

Charge-density waves and superlattices in the metallic layered transition metal dichalcogenides

J.A. Wilson , F.J. Di Salvo & S. Mahajan

To cite this article: J.A. Wilson , F.J. Di Salvo & S. Mahajan (1975) Charge-density waves and superlattices in the metallic layered transition metal dichalcogenides, *Advances in Physics*, 24:2, 117-201, DOI: [10.1080/00018737500101391](https://doi.org/10.1080/00018737500101391)

To link to this article: <http://dx.doi.org/10.1080/00018737500101391>



Published online: 28 Jul 2006.



Submit your article to this journal [↗](#)



Article views: 1599



View related articles [↗](#)



Citing articles: 1084 View citing articles [↗](#)

Charge-density waves and superlattices in the metallic layered transition metal dichalcogenides†

By J. A. WILSON, F. J. DI SALVO and S. MAHAJAN

Bell Laboratories,
Murray Hill, New Jersey 07974

[Received 1 October 1974]

ABSTRACT

The d^1 layer metals TaS_2 , $TaSe_3$, $NbSe_2$, in all their various polytypic modifications, acquire, below some appropriate temperature, phase conditions that their electromagnetic properties have previously revealed as 'anomalous'. Our present electron-microscope studies indicate that this anomalous behaviour usually includes the adoption, at some stage, of a superlattice. The size of superlattice adopted often is forecast in the pattern of satellite spotting and strong diffuse scattering found above the transition.

Our conclusions are that charge-density waves and their concomitant periodic structural distortions occur in all these $4d^1/5d^1$ dichalcogenides. We have related the observed periodicities of these CDW states to the theoretical form of the parent Fermi surfaces. Particularly for the 1T octahedrally coordinated polytypes the Fermi surface is very simple and markedly two-dimensional in character, with large near-parallel walls. Such a situation is known theoretically to favour the formation of charge and spin-density waves. When they first appear, the CDW's in the 1T (and 4Hb) polytypes are incommensurate with the lattice. This condition produces a fair amount of gapping in the density of states at the Fermi level. For the simplest case of 1T- $TaSe_2$, the room temperature superlattice is realized when this existing CDW rotates into an orientation for which it then becomes commensurate. At this first-order transition the Fermi surface energy gapping increases beyond that generated by the incommensurate CDW, as is clearly evident in the electromagnetic properties.

For the trigonal prismatic coordinated polytypes, CDW formation is withheld to low temperatures, probably because of the more complex band structures. This CDW state (in the cases measured) would seem at once commensurate, even though the transition is, from a wide variety of experiments, apparently second order.

A wide range of doped and intercalated materials have been used to substantiate the presence of CDW's in these compounds, and to clarify the effect that their occurrence has on the physical properties.

The observations further demonstrate the distinctiveness of the transition metal dichalcogenide layer compounds, and of the group VA metals in particular.

CONTENTS	PAGE
§ 1. INTRODUCTION TO THE MATERIALS.	119
§ 2. THE OBSERVATIONS OF ELECTRON AND X-RAY DIFFRACTION. SUPERLATTICE FORMATION AND DIFFUSE SCATTERING.	126
2.1. General aspects.	126
2.2. Detailed observations.	136
(a) 1T- $TaSe_2$.	136
(b) 4Hb- TaS_2 .	139
(c) 1T- TaS_2 .	140
(d) 2H polytypes.	143
(e) 6R- TaS_2 .	144

† A brief version of the main aspect of this work has appeared in *Physical Review Letters*, 32, 882 (1974).

	PAGE
(f) Mixed crystals.	144
(g) Intercalated crystals.	149
(h) Tilt experiments.	151
§ 3. CONCERNING THE BAND STRUCTURES OF THE 'IDEAL' 1T AND 2H MATERIALS.	153
§ 4. FERMI SURFACE DETERMINED PERIODICITIES AND SUPERLATTICES.	159
4.1. Pure materials ; charge and spin-density wave states.	159
4.2. Points concerning the behaviour of a CDW.	163
4.3. Alloys ; Fermi surface driven long and short-range order.	165
§ 5. DETAILED INTERPRETATION OF THE EXPERIMENTAL OBSERVATIONS IN POLYTYPES CONTAINING OCTAHEDRAL SANDWICHES.	167
5.1. Analysis of the diffraction results for the incommensurate state.	167
5.2. The commensurate CDW state.	174
(a) General aspects for the 1T polymorphs.	174
(b) The transition in the mixed coordination polytypes.	176
(c) Powder X-ray diffraction.	178
(d) More points concerning the commensurate state properties.	179
(e) The complexities of the 1T-TaS ₂ case.	182
(f) NbTe ₃ and TaTe ₂ .	182
§ 6. CONFIRMATION OF THE CDW INTERPRETATION. THE USE OF DOPED AND INTERCALATED CRYSTALS.	183
6.1. A prologue—the effect of doping on the $\sqrt{(13)}a_0$ commensurate transition.	184
6.2. The results from doping to non-superlattice conditions.	185
6.3. Further evidence in optical, electrical and magnetic data.	186
6.4. Concerning organo-intercalation.	187
§ 7. THE CASE OF THE TRIGONAL PRISMATIC POLYTYPES.	188
7.1. Background concerning the low temperature state.	188
7.2. The low temperature state related to the band-structure results.	190
7.3. The magnetic, electrical and optical properties. The suppression of T_0 .	192
7.4. Other questions concerning the stability of the $3a_0$ CDW.	194
§ 8. SUMMARY.	196
ACKNOWLEDGMENTS.	197
APPENDIX.	198
REFERENCES.	198

It is anticipated that the results presented in this paper will be of interest as much to those whose field is metal physics, as to those primarily concerned with layer materials. The paper contains much new experimental data, the basis for its interpretation being provided in our electron-microscope results. Following upon the initial microscopy on 1T-TaS₂ some two years ago, we have investigated about 25 related systems. Indeed, the plates in this paper are selected from a total of almost 1000. These results have been complemented by a variety of measurements, particularly susceptibility and resistivity. This effort was impelled by the intriguing and often spectacular nature of the superlattices and the diffuse-scattering patterns revealed with the electron microscope. Particularly fascinating and informative were the reversible first-order transitions from one régime to the other. The interpretation we give of the observed incommensurate periodicities and subsequent superlattices is in

terms of charge density waves. This interpretation enables us to understand the full range of previously anomalous electromagnetic data that over a period of five years had been steadily accumulating on these materials. We have reviewed the existing literature accordingly.

As examples of Fermi surface determined electronic instabilities, the present results are particularly simple, and, moreover, are illustrative of many more technical questions. The observed periodicities are easily picked out on the theoretical Fermi surface; we have striking commensurate/incommensurate transitions; the electronic content of the system is readily manipulated; we can see clearly the role of cation disorder. The results come at an opportune moment, when much interest exists concerning soft modes, Kohn anomalies, and correlation based states. Earlier, particular interest in the d¹-layer dichalcogenide metals had been aroused through the presence of superconductivity there, and especially how this responded to organo-intercalation. Just as interest in intercalation began to wane, we are now presented with the topical problem, as for the A15's and C15's, of interplay between a structural instability, (here induced by the CDW), and the material's superconducting transition.

With the move into the metallic transition metal compounds, it is clear now that the Fermi surface determined electronic instability is no longer the preserve of chromium and its near neighbours.

The material contained in this paper is organized in the following manner :

Section 1 gathers as background most of the experimental data which have appeared for the compounds in the past five years, relevant to the topic we shall develop.

Section 2 is confined strictly to a description of our diffraction results. These form the basis from which the present synthesis has sprung.

Section 3 is concerned with the band structures and Fermi surfaces of the materials.

Section 4 deals in general with periodicities and superlattices as driven by Fermi surfaces, and topics related to a charge-density wave as ground state.

Section 5 provides a detailed interpretation, in the light of §§ 3 and 4, of all the experimental results presented in §§ 1 and 2 (primarily for the polytypes containing octahedral sandwiches).

Section 6 gives further experimental data, especially from doped and intercalated crystals, that serves as confirmation of the interpretation offered in § 5.

Section 7 similarly treats the trigonal prismatic polytypes.

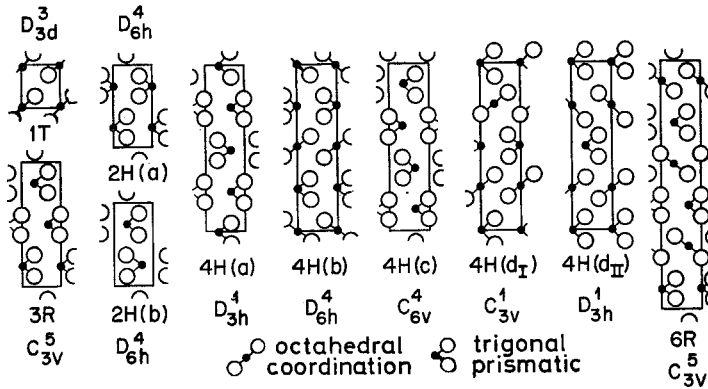
Finally, § 8 summarizes the interpretation provided by the CDW model of the various types of experimental observation reported to date, and also indicates directions for future developments.

§ 1. INTRODUCTION TO THE MATERIALS

The structure of the group VB dichalcogenides consists of sandwiches that are three atom-sheets thick. The bonding within each sandwich is covalent, while that between them is weak van der Waals type. The top and bottom sheets of the sandwich are of hexagonally packed chalcogen atoms, while the middle sheet is of metal atoms. These X-M-X sandwiches can show either

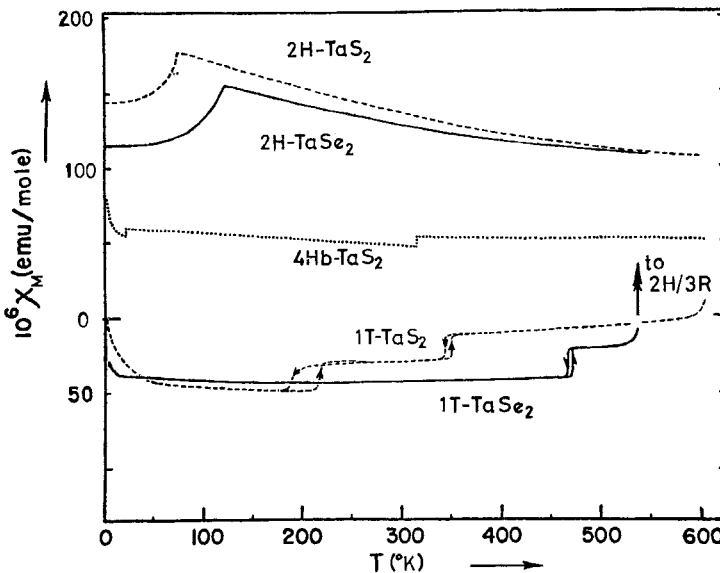
octahedral (AbC), or trigonal prismatic (AbA) coordination of the metal atoms. The sandwiches stack in a variety of ways, giving either pure octahedral (1T), pure trigonal prismatic (2H, 3R, 4Hc), or mixed coordination (4Hb, 6R) polytypes (see fig. 1). The octahedral form is the stable high temperature form of TaS_2 ($/\text{Se}_2$). It is basically of the CdI_2 type, the structure adopted by the group IV semiconductors like d^0HfS_2 . To be retained at room temperature in the 1T form, TaS_2 ($/\text{Se}_2$) must be quenched from above 1100°K in a chalcogen

Fig. 1



1120 sections of the various polytypes of the layer structure transition metal dichalcogenides.

Fig. 2



Molar susceptibilities versus T of a variety of tantalum dichalcogenides. No diamagnetic corrections have been made: these would be somewhat in excess of -50×10^{-6} e.m.u./mole. [Composite of repeated data.]

atmosphere. For the pure materials the 1T products remain metastable if not reheated beyond 550°K. The intermediate mixed coordination 4Hb and 6R polytypes are secured by quenching from about 950°K. The trigonal prismatic 2H form seems to be the room temperature stable polymorph. This latter structure is very closely related to that of the group VI semiconductors like d^2MoS_2 . All these materials have been discussed in detail in earlier papers with regard to preparation, crystallographic, magnetic, electrical and optical properties, (e.g. Wilson and Yoffe 1969, Huisman and Jellinek 1969, Lee *et al.* 1970, Thompson *et al.* 1971, Thompson, Gamble and Koehler 1972, Thompson, Pisharody and Koehler 1972, Di Salvo *et al.* 1973, 1974, Yoffe 1973) and are the subject of a new review now in preparation (Wilson, for *Rev. mod. Phys.*). However, a brief review of the anomalous properties for the compounds TaS_2 , $TaSe_2$ and $NbSe_2$ is called for here.

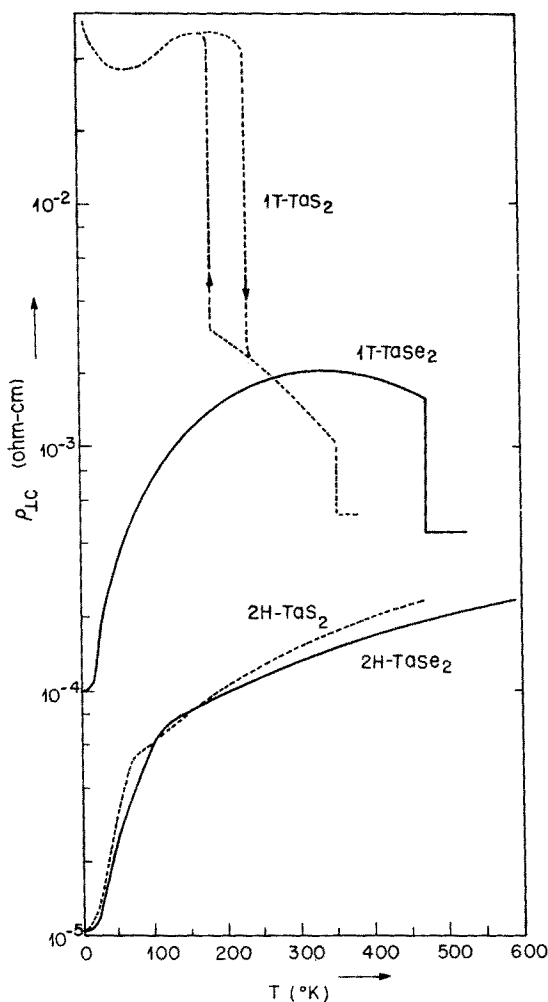
Figure 2 shows the magnetic susceptibility (χ_M) of 2H- TaS_2 , 4Hb- TaS_2 and 1T- TaS_2 from 4·2°K to 600°K. According to band-structure calculations (based upon the undistorted crystal structures of fig. 1), all of these polymorphs of TaS_2 should be d-band metals with a moderate-to-high density of states at the Fermi level. The susceptibility of 2H- TaS_2 is in accord with this, but those of 4Hb and 1T- TaS_2 are anomalously low. Further, in 1T- TaS_2 we encounter first-order transitions at 352°K and 200°K; in 4Hb- TaS_2 first-order transitions at 315°K and 20°K; and in 2H- TaS_2 a second-order one at 80°K. We shall label the higher transition temperatures in 4Hb and 1T- TaS_2 ' T_d '†. We label the transition in 2H- TaS_2 ' T_o ', since this latter turns out to be of a somewhat different character.

Early X-ray diffraction studies did not reveal any structure changes at these various 'intra-polytypic' transformation temperatures, beyond small changes in the hexagonal c and a axis parameters. The marked difference in character of the 1T and 2H polytypes, and of their intra-polytypic transitions is very clearly demonstrated in fig. 3. Figure 3 shows the basal plane resistivity ($\rho_{\perp c}$) of 1T- and 2H- TaS_2 (see fig. 8 for 4Hb), along with similar plots for the selenides. For the 2H polytypes the intra-polytypic transitions do not too greatly perturb the metallic condition, but for the 1T and 4Hb polytypes the effects are quite dramatic.

A striking feature to have been observed earlier with 1T- TaS_2 was that the Seebeck coefficient changes sign from negative to positive on warming through its 352°K transition (Thompson *et al.* 1971). Despite a break, the Hall coefficient remains negative. Although the number of carriers above T_d was indicated to be very high, ρ is also high at $5 \times 10^{-4} \Omega \text{ cm}$ (see fig. 3). This resistivity is three times more than that of the 2H polytype at the same temperature. Above T_d the carriers in the octahedral polytypes evidently suffer heavy scattering. Indeed, in the near infra-red reflectivity spectrum of 1T- TaS_2 rather little change is observed upon passing above T_d , (see fig. 4). The classical Drude behaviour, quite well exhibited by the 2H polytype in the near I.R. (Bachmann *et al.* 1971), is for 1T- TaS_2 completely disrupted above, as well as below T_d . Only after replacing more than 70% of the Ta with Ti does the 1T free-carrier reflectivity begin to appear 'normal' (Benda 1974).

† Our labelling, ' T_d ', related to distortion; ' T_o ', to onset.

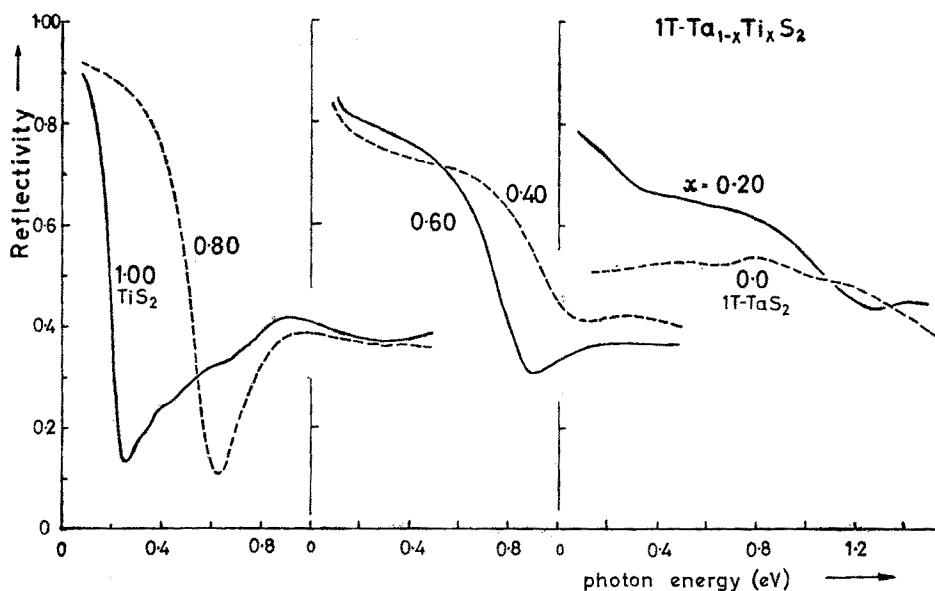
Fig. 3



$\rho(\perp c)$ versus T for the 1T and 2H tantalum dichalcogenides, (see fig. 8 for 4Hb-TaS₂). [Composite of repeated data.]

[As will be demonstrated, these latter optical measurements, made on mixed cation crystals 1T-(Ta/Ti)S₂ at helium temperatures, in fact correspond, for all Ti \geq 15%, to $T > T_d$. Thompson, Pisharody and Koehler (1972) had already reported that (at 300°K) the Seebeck coefficient was positive for (1T)-Ta_{0.9}Ti_{0.1}S₂, as for pure 1T-TaS₂ above T_d .] Thompson, Pisharody and Koehler (1972) observed further that for the 50% alloy Ta_{0.5}Ti_{0.5}S₂ the electrical resistivity is virtually temperature independent (at $\sim 8 \times 10^{-4} \Omega \text{ cm}$) right down to 4°K. For all concentrations of Ti less than this, ρ in fact *increases* on cooling, and in pure 1T-TaS₂ the apparent activation energy between the 200°K and 352°K transitions is 0.02 eV ($\equiv 160 \text{ cm}^{-1}$ or 230°K). At the lower (200°K) transition in 1T-TaS₂ (the equivalent of which does not occur in the selenide), the resistivity increases by a further order of magnitude, and at

Fig. 4



Infra-red reflectivity (at $\sim 4^\circ\text{K}$) from 0.1 to 1.5 eV through the d^0/d^1 series $1\text{T-Ta}_{1-x}\text{Ti}_x\text{S}_2$ (data from Benda 1974). The anomalous behaviour develops strongly for $x < 0.5$. The marked change between 0.2 and pure TaS_2 occurs when the latter is below T_d , as here.

4°K , ρ remains $\sim 5 \times 10^{-2} \Omega \text{ cm}$ (see fig. 3). By contrast, for 2H-TaS_2 , ρ is $\sim 5 \times 10^{-6} \Omega \text{ cm}$, just prior to superconductivity appearing at 0.8°K .

In table 1 the results of thermal and pressure measurements at the various *intra*-polytypic transitions are collected for a number of compounds. The volume changes are calculated from the Clausius–Clapeyron equation, using the dT_d/dP and ΔS data. The negative sign of each ΔV derives from the Clausius–Clapeyron equation, given the fact that these transitions are all endothermic. ΔV is largest for 1T-TaSe_2 at -0.4% . For the 4Hb materials there is virtually no change in Δa_0 , the volume contraction being carried by Δc_0 . Present indications are that refined structural determinations will prove difficult. In fig. 5 we summarize the known ranges of polytypic stability and metastability, and the various inter- and *intra*-polytypic transition temperatures for the typical case of TaSe_2 . In the present paper we concentrate on the *intra*-polytypic transitions. These, as indicated in table 1 and fig. 6, entail heats of transition of as high as 300 cal/mole, but this still is several times smaller than that of an *inter*-polytypic transition (typically $1\frac{1}{2}$ –2 kcal/mole).

One of the present authors suggested some years ago (Wilson and Yoffe 1969, § 8.2), when the anomalous properties of 1T-TaS_2 were first being noted, that the solution lay with an understanding of the complex electron diffraction patterns then obtained from 1T-TaS_2 at 300°K . The interpretation proffered at that time was that shear structure formation occurred, as in $\text{V}_n\text{O}_{2n-1}$, WO_{3-x} , etc., this hindering normal carrier mobility below T_d . However, it was later recognized that the anomalous behaviour shown by the 1T materials

Table 1.

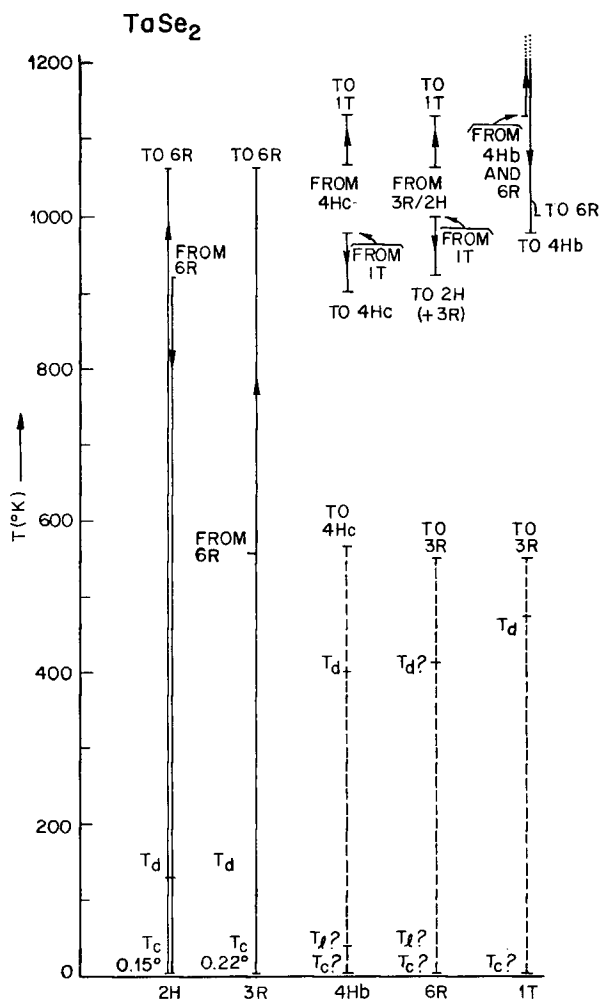
	ΔH	T_d	ΔS	dT_d/dP	Calc. $\Delta V/V$	Observed $\Delta c/c$
2H-TaSe ₂ (a)	+1.0 (integ.)	120†	+0.008	—	—	—
1T-TaSe ₂ (b)	+338	473	+0.73	-4.7	-0.38	—
4Hb-TaSe ₂ (c)	+130	410	+0.32	—	—	-0.4
4Hb-TaS ₂ (d)	+110	315	+0.35	-5.5	-0.22	—
1T-TaS ₂ (e) (1)	+123	350	+0.35	-3.0 (b), (f)	-0.10	—
(a) (2)	+54	~190	+0.28	—	—	-0.34
	(cal/mole)	(°K)	(cal/mole-°K)	(°K/kB)	(%)	(%)

References

- (a) Bagley *et al.* (1975).
 (b) Di Salvo *et al.* (1974).
 (c) Huisman and Jelinek (1969).
 (d) Di Salvo *et al.* (1973).
 (e) Thompson *et al.* (1971).
 (f) Chu *et al.* (1971).

† T_0 .

Fig. 5

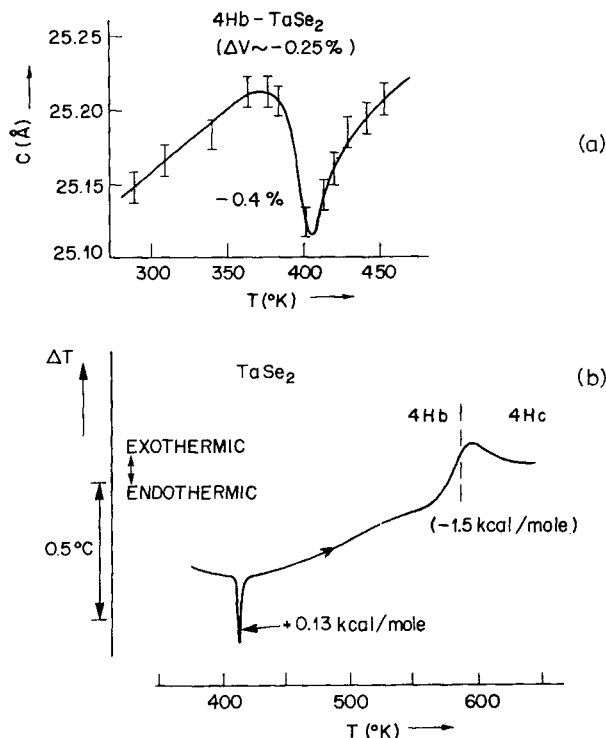


Inter- and intra-polytypic changes for the case of TaSe_2 . The inter-polytypic transition temperatures are drawn from Huisman (1969). The 1T, 4Hb and 6R polytypes are brought into the low temperature range (shown dashed) by quenching.

particularly in resistivity (see fig. 3) persists above T_d . Furthermore, the crystals all proved to be of quite good stoichiometry†. The remainder of this paper provides what we hope to substantiate as the proper solution to the above problems. The form of explanation rationalizes also the anomalies in the low temperature behaviour of the 2H polytypes, though detailed comments on the latter are reserved mainly for § 7.

† Present analysis shows them good to better than 0.5%.

Fig. 6



Data for $4Hb-TaSe_2$ from Huisman (1969), relating to its intra-polytypic transition at 410°K and its inter-polytypic transition to $4Hc$; (a) crystallographic change, (b) DTA trace.

§ 2. THE OBSERVATIONS OF ELECTRON AND X-RAY DIFFRACTION SUPERLATTICE FORMATION AND DIFFUSE SCATTERING

2.1. General aspects

Because layer crystals cleave easily they are ideally suited for electron microscopy, and accordingly their general characteristics are well documented (Amelinckx 1964). The recent papers of Allpress (1972) and Bursill (1972) on oxide shear-structures, and of Van Landuyt *et al.* (1970) on $NbTe_2$, demonstrate the power of the technique directly to reveal superlattices and other complicated structural features.

For $NbTe_2$ the crystals were observed to be broken up into twin domains, presumably as a result of strain generated in the underlying CdI_2 structure by the presence of marked metal-metal bonding. The domains are of such a small size that, unless the electron beam is carefully constrained to interact with a single domain, the observed diffraction pattern is highly confused. The investigation of Van Landuyt *et al.* has served to confirm the X-ray determined structure of $NbTe_2$ and $TaTe_2$ (Brown 1966); a structure which we shall use later in § 5.2. In $NbTe_2$, metal-metal bonding causes marked shifts from the 'ideal' atomic positions that reach almost 0.5 Å. Circumstances are similar

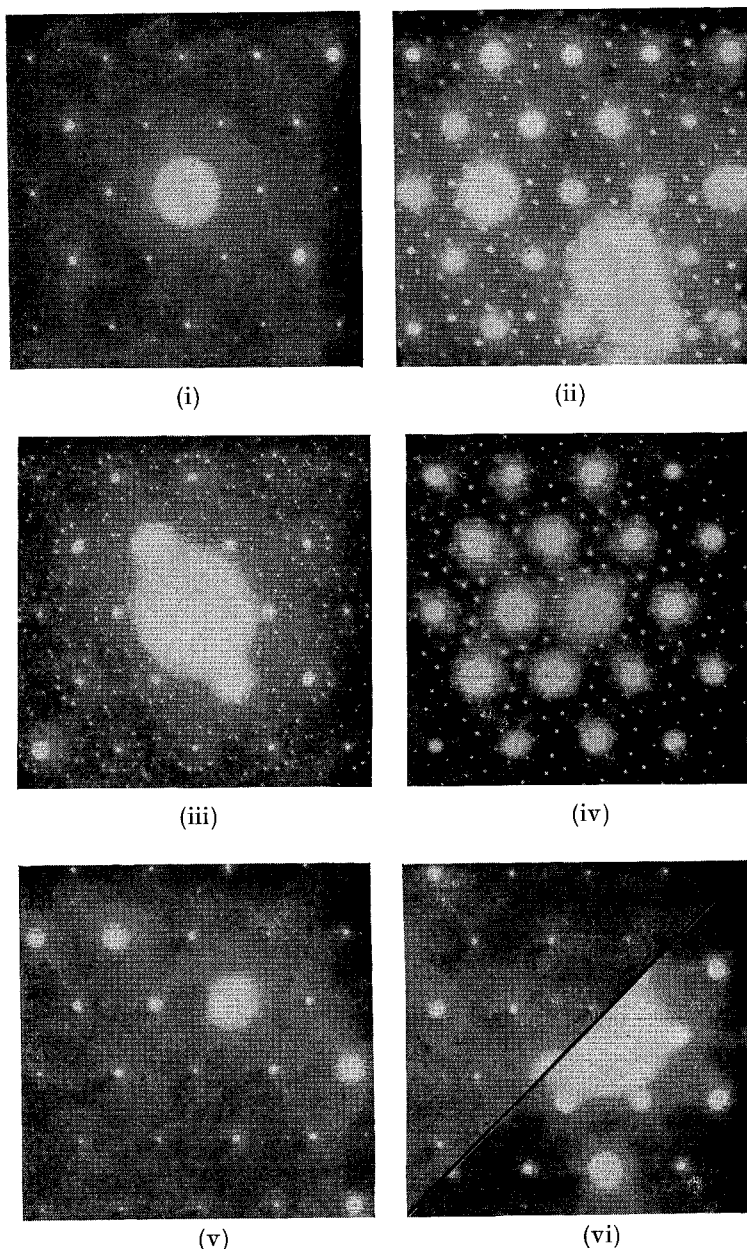
in $d^2\text{WTe}_2$ and $d^3\text{ReSe}_2$. For $\text{ReS}_2(/Se_2)$ the band structure must be very substantially modified by the distortion, as in the ideal structure they would be metals, but in fact are 1 eV gap semiconductors (see Wilson and Yoffe 1969). Standard X-ray powder patterns from the above distorted structures are covered in 'extra' lines of fairly high intensity, corresponding to the increase in cell size and to the reduction in cell symmetry following the appreciable atomic displacements. Such marked distortions are not testified to by the X-ray patterns obtained from the materials introduced in § 1.

Our electron diffraction patterns are obtained from crystals cleaved to less than 2000 Å in thickness, with the electron beam usually normal (or nearly so) to the layers. Consequently we see the reciprocal lattice reflections ($hk \cdot 0$) in the hexagonal (or pseudo-hexagonal) cell. The beam voltage was varied from 80 up to a standard 200 kV; no fundamental changes in the diffraction patterns were observed. The effects of double diffraction and spot elongation due to the thin samples are discussed later.

Figure 7 shows electron-diffraction patterns as obtained at room temperature for several $\text{TaS}_2(/Se_2)$ polytypes. [The scale of magnification for all diffraction patterns shown in this article is approximately the same, so comparisons may be made from one plate to the next.] The pattern for stoichiometric 2H-TaSe₂ at room temperature is 'normal', i.e. it is hexagonal with the spot separation proportional to the reciprocal of an a_0 axis taken equal to the Ta-Ta separation within a sandwich. Since these a_0 axes in all the Ta and Nb layered polytypes are approximately the same (3.315 Å for 2H-TaS₂ to 3.477 Å for 1T-TaSe₂), the ($hk \cdot 0$) diffraction patterns from the various polytypes should all appear very similar, according, that is, to those simple X-ray determined structures portrayed in fig. 1. That this is not the case is obvious from fig. 7. Various superlattices are present even at 300°K. Figure 7 (v), moreover, shows a $3a_0$ superlattice to be established in pure 2H-TaSe₂ below 120°K, a temperature at which its physical properties were noted earlier to become anomalous (see § 1; also § 7). Judging from these ($hk \cdot 0$) projections alone the superlattices would appear to be hexagonal. One should note however that strongly distorted ReSe₂ and NbTe₂, which are in fact triclinic and monoclinic respectively, appear hexagonal in cleavage plane electron-diffraction patterns.

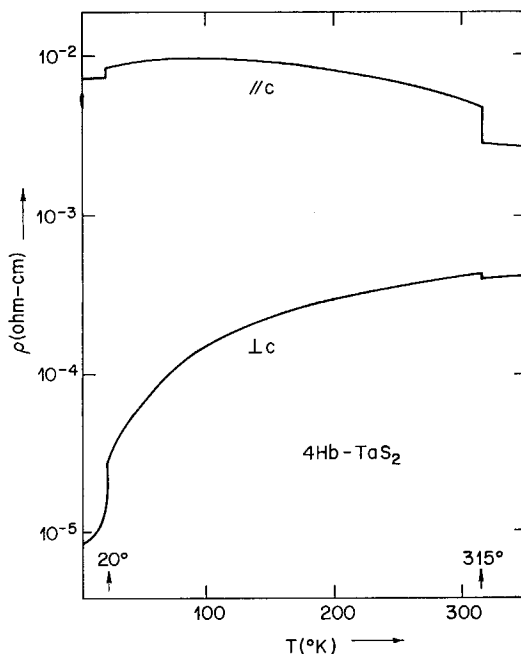
In the 4Hb pattern the diffraction spots corresponding to the parent lattice are always clearly evident. For 4Hb-TaS₂ we suspect that the superlattice transition at 315°K (see figs. 8 and 2; after Di Salvo *et al.* 1973) affects only the octahedral sandwiches, leaving the interposed trigonal prismatic sandwiches undistorted. The trigonal prismatic sandwiches would appear to distort at 20°K. (Unfortunately we have no liquid helium facility on the microscope to observe this low temperature transition directly.) The room temperature pseudo-hexagonal superlattice for 4Hb-TaS₂ corresponds to $a = 13a_0$. That of 1T-TaSe₂ corresponds to $a = \sqrt{13}a_0$ rotated by $\tan^{-1} \sqrt{\frac{3}{7}}$ (i.e. 13° 54') relative to a_0 . For 1T-TaS₂ the 300°K diffraction pattern is extremely complex, and as yet we do not have a proper explanation for its appearance, although it is clearly closely related to that from 1T-TaSe₂. Taking the pseudo-hexagonal view it would yield a value of $a \sim 81\frac{1}{2}a_0$, implying some 6650 molecular units per cell. However, in view of what follows, we shall avoid such an interpretation. We find, for example, that these numbers are a function of the temperature.

Fig. 7



Electron diffraction plates showing superlattice formation. (i) 2H-TaSe₂ (300°K). A crystal showing standard a_0 parameter. (ii) 1T-TaSe₂ (300°K). Pattern, for well-oriented sample, from $\sqrt{13}a_0$ superlattice, (β -type domain). (iii) 4Hb-TaS₂ (300°K). Pattern indexable on $13a_0$ superlattice. Equivalent to superposition of α and β -domain patterns (see fig. 15 (i)). (iv) 1T-TaS₂ (300°K). Basically $\sqrt{13}a_0$ superlattice pattern (here of α -domain type), but with complex 'decoration' (see figs. 17 and 18). (v) 2H-TaSe₂ (90°K). Sharp spots from $3a_0$ superlattice. (vi) (a) 2H-TaSe₂ (135°K). Corresponding diffuse scattering seen up to 50° above T_0 (120°K). (b) 2H-Ta_{1.08}Se₂ (300°K). Same scattering, but more intense.

Fig. 8



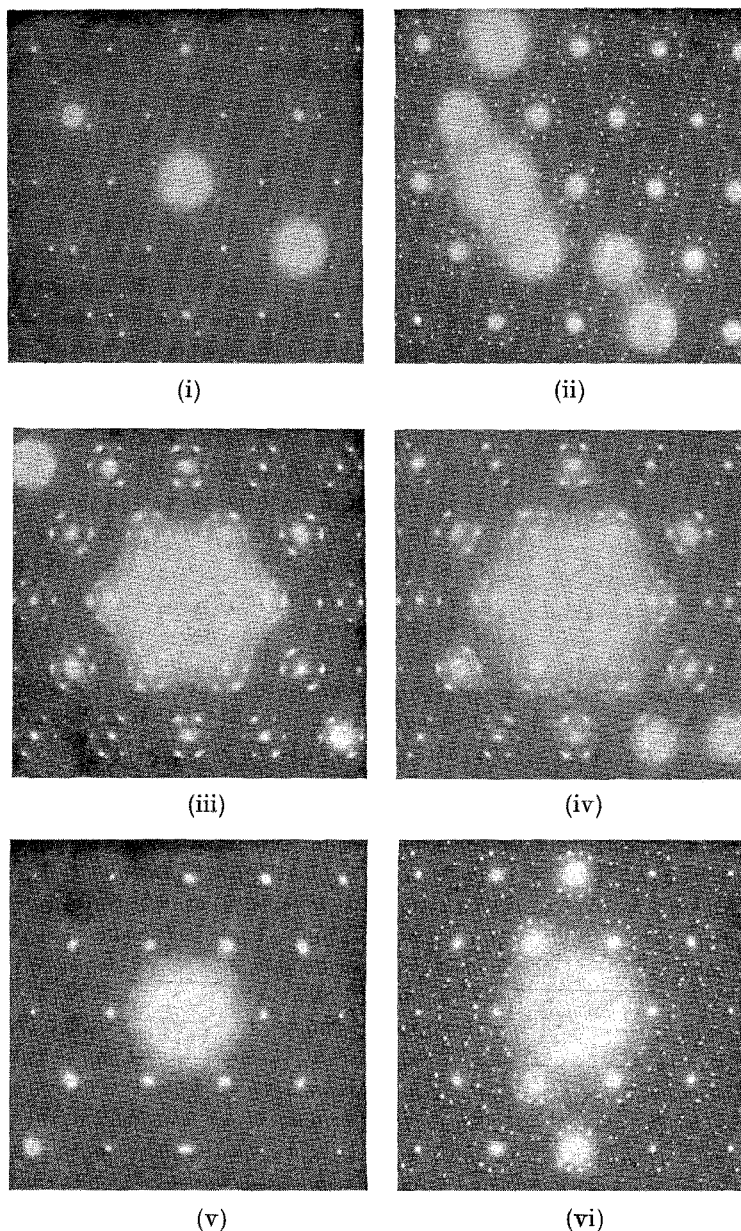
Resistivity in 4Hb-TaS₂, \perp and $\parallel c$, through both intra-polytypic transitions (compare fig. 3 for 1T and 2H-TaS₂) [from Di Salvo *et al.*, 1973].

Knowing that superlattices are present in these compounds, evidence of their presence and form was sought more carefully in X-ray diffraction. Since not previously observed, the superlattice lines were expected to be very weak, and long exposures in a camera that eliminated background radiation were clearly necessary. A great many superlattice lines were finally recorded using a Guinier powder diffraction camera with a bent crystal monochromator. For 1T-TaSe₂ an exposure of 110 hrs (at 300°K), using CuK α radiation with the tube at 17 kV (to eliminate radiation wavelengths at half the K α wavelength), and 40 mA, showed 85 superlattice reflections for 2θ up to 90° (Di Salvo *et al.* 1974). Similar results are reported for other polymorphs in § 5.2 (c). The X-ray work was performed to confirm the conclusions drawn from the electron-diffraction experiments, especially the tilting experiments (see § 2.2 (h)).

The reason that the superlattices are so easily seen by electron diffraction is that for electrons, unlike X-rays, the scattering is in the dynamical limit (i.e. multiple scattering is important). Many authors have discussed dynamical scattering, but a simple picture comparing X-ray and electron diffraction is given by Allpress (1972). The disadvantage with electron diffraction is, then, that determination of atomic positions from the intensities of the diffracted electron beams is extremely difficult, if not impossible.

For X-ray (or neutron) scattering the intensity of the superlattice lines reflects the degree of displacement modulation of the parent structure (Guinier 1963, Chap. 7; Overhauser 1971). In the 1T-type materials this is revealed to be rather small (~ 0.1 Å), in agreement with the small adjustments found

Fig. 9



Electron-diffraction plates obtained by heating above T_d . (i) 1T-TaSe₂ (500°K). Diffuse rings, and various orders of structure modulation satellite spotting in the (incommensurate) phase above T_d (473°K); (see fig. 13). (ii) 4Hb-TaS₂ (300°K). $13a_0$ superlattice prior to heating, from specimen giving plates (ii) to (vi). (iii) 4Hb-TaS₂ (320°K). Intermediate condition in conversion to high temperature phase ($T_d=315°K$). Low temperature α -domain spotting still evident; contrast fig. 12 (v) from 6R-TaS₂. The small linear accommodation made in attaining the superlattice is apparent here. (iv) 4Hb-TaS₂ (350°K). No second-order spotting is ever apparent for 4Hb and 6R. (v) 4Hb-TaS₂ (460°K). First-order spots much weakened and diffuse. (vi) 4Hb-TaS₂ (300°K). $13a_0$ superlattice condition as re-established from (v). Note, however, weak spots at $a_0^*/2$ not present originally.

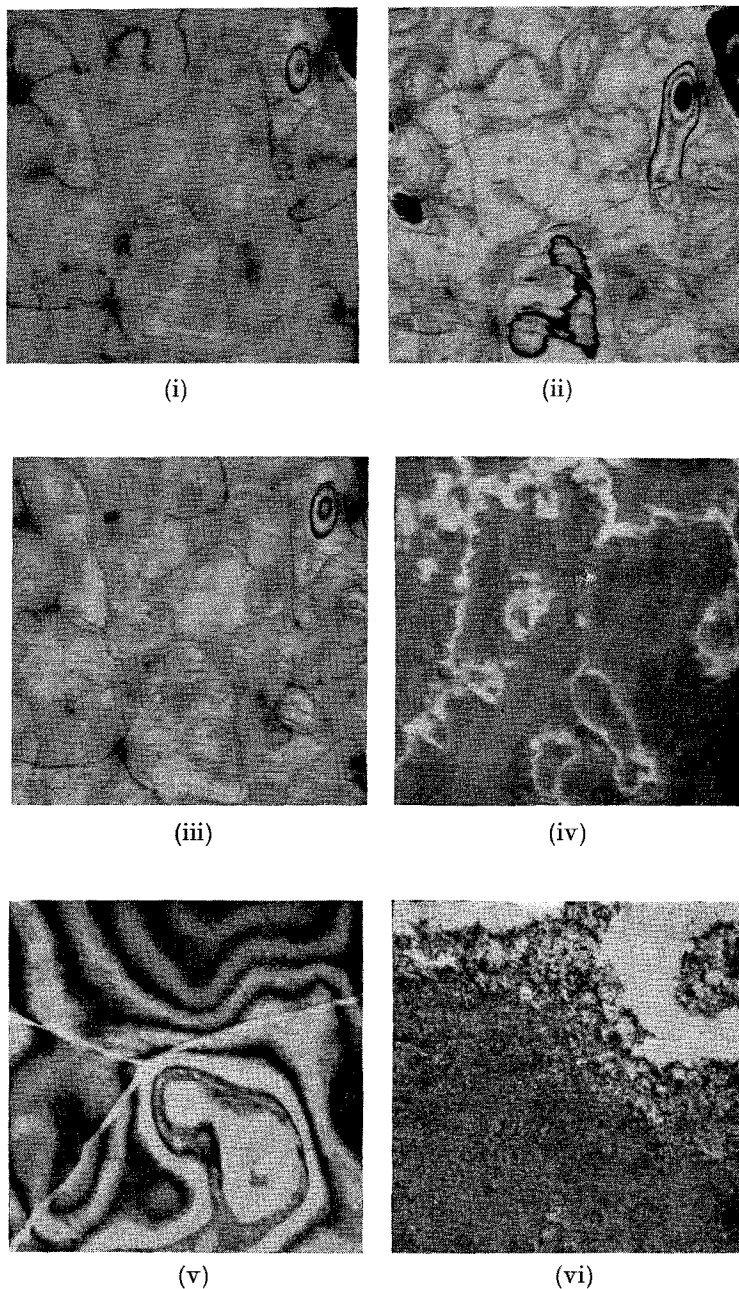
both in lattice parameter and enthalpy when the superlattice is adopted (see § 1). Actually, for 2H-NbSe₂, superlattice lines of extremely low intensity had been indicated earlier with X-rays at low temperatures, following upon a very slight discontinuity in c/a (Marezio *et al.* 1972). The superlattice that they tentatively suggested (at 10°K) had $a = 2a_0$, in contrast to the $a = 3a_0$, which we clearly observe by electron diffraction (for 2H-TaSe₂). However, the authors expressed doubt about the exact cell, since only a few superlattice lines were observed and these with signal to noise of approximately one. Displacements considerably less even than in the 1T and 4Hb polytypes are implied by this result.

Above their respective first-order transitions (T_d), the electron-diffraction patterns from the 1T and 4Hb-type materials become very similar. They are both characterized by strong diffuse scattering in a chain-like pattern of interlocking circles, which persists more than 100° into the new phase, indeed right to the temperature ($\geq 550^\circ\text{K}$) at which these metastable phases convert irreversibly to the trigonal prismatic polytypes. Figure 9 includes a sequence of plates for 4Hb-TaS₂ taken up through this diffuse-scattering high-temperature régime, along with the room-temperature pattern as regained upon cooling back below T_d . Proof of reconstitution of the superlattice at room temperature is significant for two reasons: (a) it shows that the effects are properties of the particular polymorph itself, and NOT due to some irreversible inter-polytypic transformation; (b) it shows that they do not follow from loss of chalcogen in the high vacuum of the microscope during heating. The geometry of the satellite spotting and diffuse scattering observed above T_d is later shown to be directly connected with the form of the Fermi surface in k -space (at least for those polymorphs where band-structure calculations have been reported). This relation will be discussed in principle in § 4, and material by material in § 5 and § 7.

Direct observations of the superlattice transitions themselves, in the electron microscope, again clearly separate the 1T/4Hb materials from the 2H, etc. For the former group the first-order transition shows very little hysteresis, as noted also in the scanning calorimeter and susceptibility measurements. The dislocations remain more or less fixed through the transition, but the many swirling bend contours, which characterize these particular layer materials, flicker wildly. Figure 10 (i) to (iii) shows such contours in a 4Hb specimen firstly above, then below, and finally re-heated to above T_d . As will be noted, there is a rather detailed reconstitution of the initial strain conditions even at this micro-level. Table 1 records that the volume strains at these transitions lie between 0.1 and 0.4%. Our electron microscope data (see table 2) for 1T-TaS₂ in fact indicate a discontinuous reduction at T_d in the basic lattice parameter, a_0 , of about 1½%. Contrasting with the 1T-4Hb materials, the trigonal prism-type materials show in their diffraction patterns steady build-up towards and into their commensurate $3a_0$ superlattice condition in second-order fashion, as other measurements would also indicate (see fig. 2).

We have also directly observed the *irreversible* interpolytypic conversion of the 1T polytype, which occurs around 550°K. In comparison to the *intra*-polytype transitions it is very sluggish. Samples can readily be secured in which one may see in transmission, using an optical microscope, a local merging of the yellows and browns of the 2H phase, the greens of the 4Hb, and

Fig. 10



Electron micrographs from 1T-TaS₂. (i) 360°K, (ii) 345°K, (iii) 360°K: This sequence indicates the changes in strain pattern of the band contours through the 352°K transition, and demonstrates the high degree of reversibility (13 000 ×). (iv), (v), (vi) Dark-field plates in superlattice state; (iv) from superlattice spot cluster of type *b*, (v) from an α_0^* spot, (vi) from superlattice spot cluster of type *a*, for same area as plate (v). The origin of the remarkable grainy contrast is not understood.

Table 2.

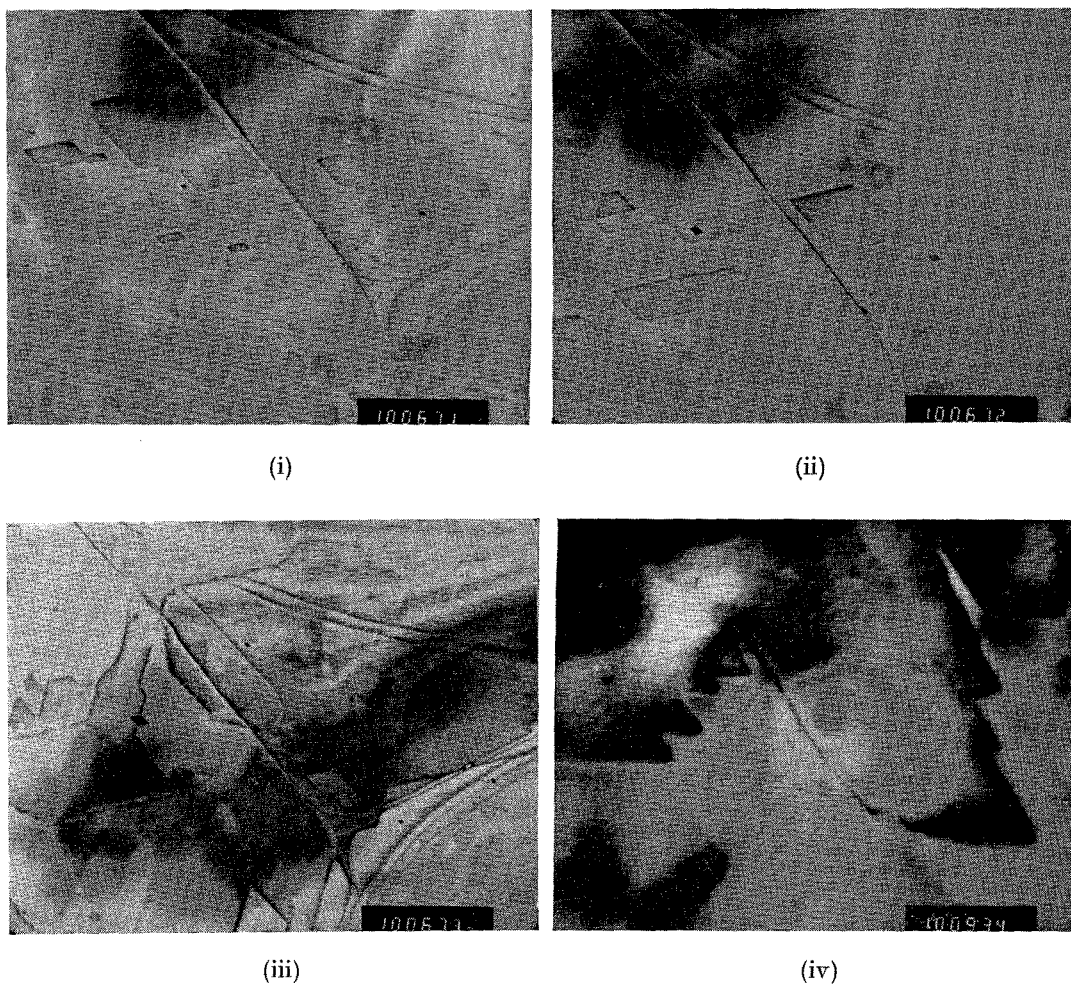
	$\frac{\Delta a_0}{a_0}$ % ($\pm 0.5\%$)	$\frac{q_0'}{a_0} \equiv \frac{a_0}{\lambda' \text{ (triple) (CDW)}}$ (± 0.005)	$\lambda' \text{ (triple) } a_0$ (± 0.05)	% incommensurateness relative to $\sqrt{13}a_0$ in $\lambda' \text{ (triple) (CDW), } T > T_d$ ($\pm 1.5\%$)
1T-TaS ₂	-1.5	0.288	3.47	-3.8
4Hb-TaS ₂	0.0	0.263	3.80	+5.2
1T-TaSe ₂	---	0.285	3.51	-2.6
4Hb-TaSe ₂	(+0.1%, X-ray)†			
Ideal		$1/\sqrt{13} = 0.2773$ ($5/18 = 0.2778$)	$\sqrt{13} = 3.606$ ($\approx 18/5$)	0.0

(The primes on q_0 and λ_{CDW} denote the basal plane projection values.)
 (We have not, with the measuring techniques used, managed to detect any change in λ with temperature; for chromium λ decreases from $0.963a_0$ at 77°K to $0.952a_0$ at 310°K.)

† See table 1.

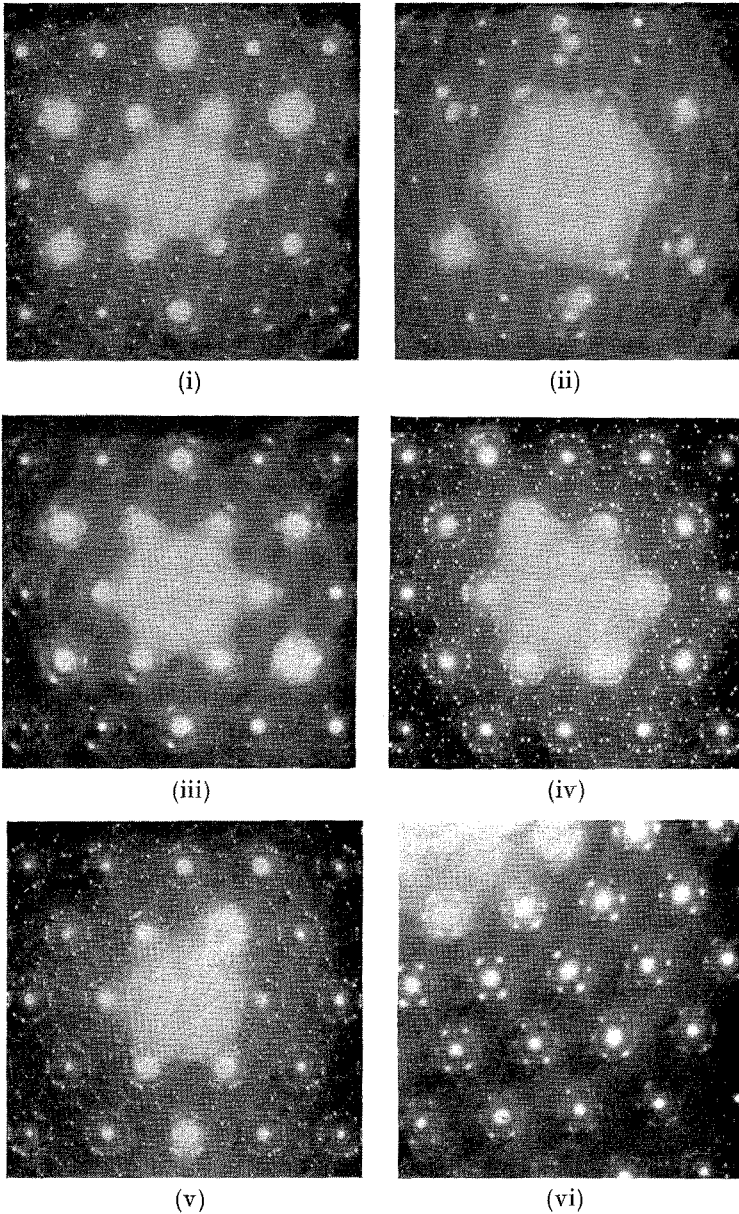
the steel-blues of the 1T. In the electron microscope one can see that this transition (as distinct from the intra-polytypic transitions) proceeds relatively slowly via nucleation and growth probably within each sandwich, the sandwiches converting more or less independently down through the bulk of the sample (see fig. 11). Detailed observations concerning the inter-polytypic transitions will be reported separately. However, we should note here that in aged 1T-TaSe₂ both intra and inter-polytypic transitions may be observed concurrently. Such crystals presumably are more heavily nucleated, so that the reversion of the metastable polytype is promoted at lower temperatures than in fresh crystals.

Fig. 11



Electron micrographs from 1T-TaSe₂ showing slow reversion to 2H structure at 460°K (i.e. just below T_d). Plates (i), (ii), (iii) were taken at 2 minute intervals (mag. 20 000). The sandwiches, in the early stages shown here, probably convert individually. This same area of crystal was earlier investigated in the experiments of fig. 15. The polytypic conversion boundaries appear to be 11 $\bar{2}0$. Mag. for plate (iv) is 50 000. See also fig. 19.

Fig. 12



Electron-diffraction patterns for 1T and 6R-TaS₂. (i) 1T-TaS₂ (cooling through T_d). Details of the high and low temperature phases are seen superposed (see fig. 13). The 'decoration' of the low temperature phase is rotated and enlarged compared with at 300°K (see fig. 7 (iv)). Similar effect to be seen in fig. 24 (vi). (ii) 1T-TaS₂ (360°K). The two sets of diffuse rings are strongly evident, plus many of the structure modulation satellites of various orders. Contrast with fig. 24, and with fig. 9 (iv) for 4Hb-TaS₂. (iii) 1T-TaS₂ (530°K). Second-order spots now gone; return on cooling. (iv) 6R-TaS₂ (300°K). Besides spots of the α/β sets many other spots of $13a_0$ superlattice show faintly. Also some $2a_0$ spotting. (v) 6R-TaS₂ (warming through T_d). Linear accommodation made between phases apparent here. Compare fig. 7 (iii). (vi) 6R-TaS₂ (310°K). Carried into h.t. phase by beam heating (note bottom right). No second-order spots (as 4Hb).

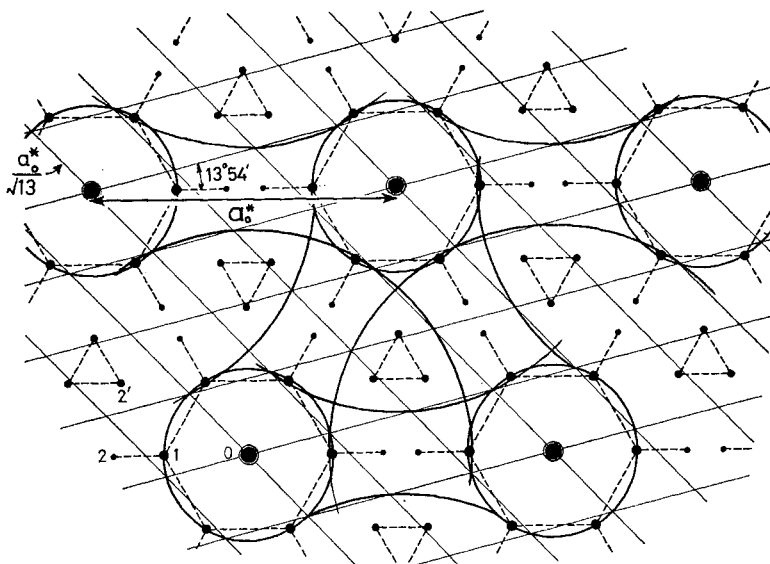
2.2. Detailed observations

In the remainder of the present section we describe the details of the experimentally observed electron-diffraction patterns, the various materials being taken one by one. We here draw attention to (a) in the Appendix, which illustrates the relationship between reciprocal and direct space for the hexagonal system; also to the combination of symmetry related plane waves (b). Note that a_o^* is equal in magnitude to $2/\sqrt{3} \cdot 2\pi/a_o$, and that \mathbf{a}_o^* is rotated by 30° from \mathbf{a}_o .

(a) $1T\text{-TaSe}_2$

Diffraction from the room-temperature superlattice was shown in fig. 7 (ii). Figure 9 (i) ($T \approx 480^\circ\text{K}$) is representative of the $T > T_d$ patterns. This TaSe_2 pattern is similar in all details to those from $1T\text{-TaS}_2$ above T_d (fig. 12 (ii)). The diffraction data obtained above and below T_d for the two phases of $1T\text{-TaSe}_2$ are clarified and correlated in fig. 13. The room temperature superlattice is there represented by the '3-by-1' $13^\circ 54'$ -rotated hexagonal net of side $a^* = a_o^*/\sqrt{13}$. The more complicated spotting and diffuse rings ('bicycle chains') of the high temperature unrotated condition have been made to show up strongly in the diagram. Experimentally the basic array of a_o^* spots becomes obvious in the *low* temperature phase, only where the sample is very

Fig. 13



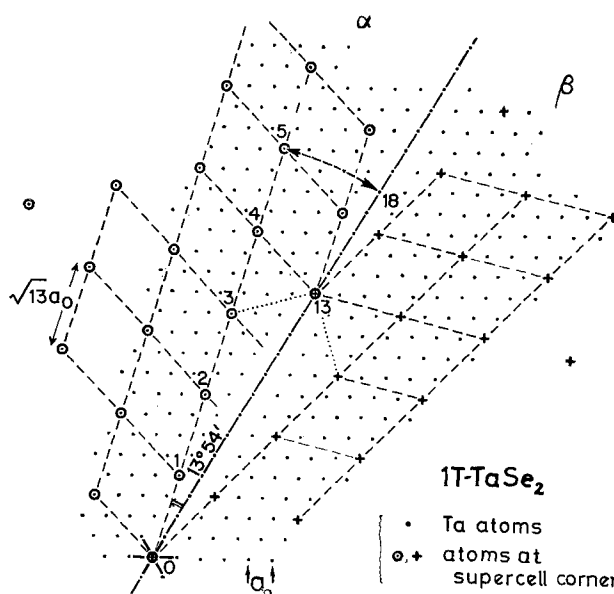
Geometric relationship between the basal plane electron-diffraction patterns obtained from $1T\text{-TaSe}_2$ above and below T_d . All straight lines serve merely to draw attention to the pattern periodicity. The spots† shown are for the h.t. phase, as are the rings. The spots in the low temperature pattern fall at the vertices of the rhombohedral net (α -oriented); $\theta = +13^\circ 54'$.

† Here neglecting the 1° twist of satellite vector relative to main spotting axis.

carefully orientated normal to the electron beam using the Kikuchi pattern. In the high temperature phase the radius of the smaller circle of diffuse scattering is just 3 to 4% (see table 2) large than a_0^* , the low temperature superlattice unit. Thus the ratio of this radius to a_0^* is $\approx 1/\sqrt{13}$ (i.e. ≈ 0.277 or $5/18$). We will concern ourselves later with just how this particular magnitude originates.

It is a remarkable fact that many fairly sharp spots are still present in the high temperature diffraction pattern. The first set of six spots appearing around each a_0^* point we label type 1. These first-order satellites experimentally appear in the basal plane sections here at very close to $5/18a_0^*$ †. The spots of the weaker set seen at $5/18a_0^*(\hat{\mathbf{a}}_{01} + \hat{\mathbf{a}}_{02})$ as a triangular cluster, we label type 2. The somewhat weaker spots at $\sim 10/18a_0^*$ (which may not be detectable in the printed version), we label type 2'. The reason for this form of labelling will be explained later. Exactly where the spots occur in three-dimensional reciprocal space is shown in § 2.2 (*h*). In § 5.1 the origin of these satellite spots above T_d is shown to be an incommensurate charge-density wave‡. Spots of types 2 and 2' are found to disappear relatively quickly upon substitution of Ti for Ta (see § 6), and they likewise disappear first during the heating experiments (see fig. 12 (iii)). From a careful examination of the high-temperature diffraction patterns it appears that each complete set of satellite spots (1, 2 and 2') is fractionally rotated ($\sim 1^\circ$) around its central Bragg peak, the sense of this rotation being towards the low temperature superlattice favoured for that particular crystal section. The effect can be clearly seen in fig. 24 (i).

Fig. 14

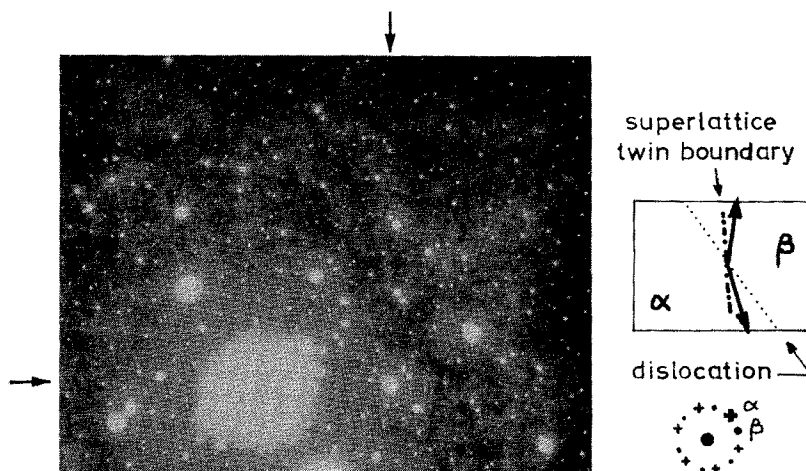


α and β -rotated superlattice domains as defined in the hexagonal array of cations of a single sandwich. The twin domain boundary is here an atom row.

† We later use the generalized label \mathbf{q}_{oi}' for such a vector.

‡ Or rather the induced periodic structural distortion in the atomic array.

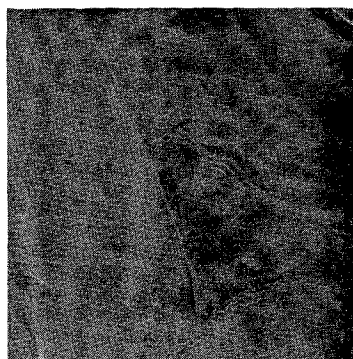
Fig. 15



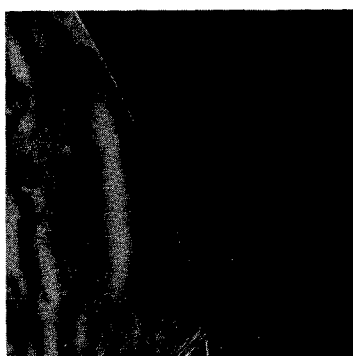
(i)



(ii)



(iii)



(iv)



(v)

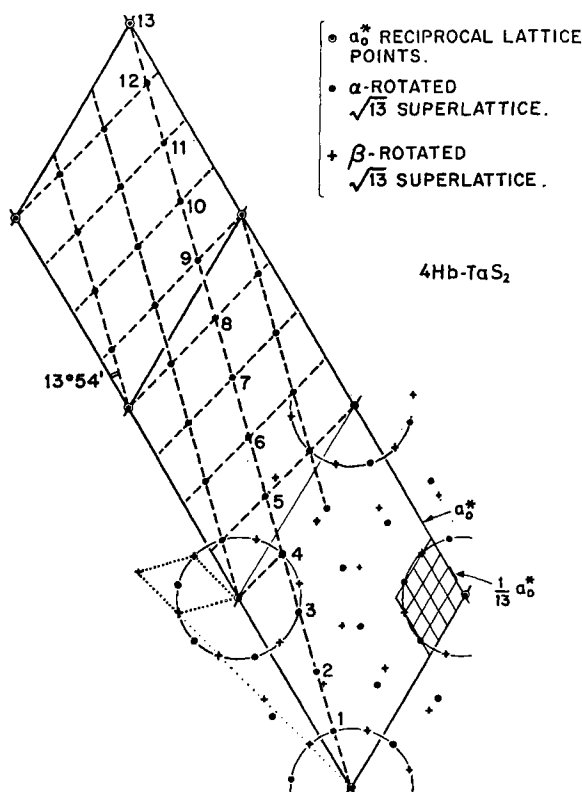
Superlattice domains in $1T\text{-TaSe}_2$ (300°K). (i) Diffraction, with aperture centred on dislocation forming α/β superlattice domain boundary. Insert relates to spots used in dark field work. (ii) Bright field ($20\,000\times$) of area around this dislocation. (The same area was later used in the work of fig. 11). (iii) Dark field of same region, using spot from main a_0^* lattice indicated above. (iv) Dark field using α -type superlattice spot, illuminating left-hand domain. (v) Dark field using β -type superlattice spot, illuminating right-hand domain. (Our thanks are due to A. G. Cullis for the results of this session, and those shown in fig. 11).

The superlattice developed below T_d may arise with the '3-by-1' operation to either side of the primary strings of a_0^* spots, thereby leading to twin domains α , β . Figure 14 shows the formation in direct space of a superlattice twin domain boundary. Such boundaries have been observed, but they are rather infrequent (≥ 0.2 mm apart in a good crystal). Figure 15 shows diffraction from the vicinity of such a boundary, which was associated in this particular case with a bundle of dislocations. What is immediately obvious from fig. 15 is that the rather complex diffraction pattern obtained from 4Hb-TaS₂, shown earlier in fig. 9 (ii), has the form of a superposition of α and β -rotated 1T-TaSe₂ patterns (see (b) below). Upon cycling 1T samples repeatedly through the superlattice transition, it seems the choice of orientation (α or β) becomes progressively less random.

(b) 4Hb-TaS₂

The geometry of the room-temperature diffraction pattern (fig. 9 (ii)) is clarified in fig. 16. As noted just above, this pattern is formed by the addition of the α and β -rotated $\sqrt{13}a_0$ patterns. This produces a $13a_0$ axis parallel

Fig. 16



The 4Hb superlattice diffraction pattern seen as the addition of α and β -rotated 1T-(TaSe₂) patterns. Parts are shown of the following hexagonal reciprocal lattice networks; (a) the parent a_0^* one, (b) both $a_0^*/\sqrt{13}$ rotated ones, (c) the unrotated $a_0^*/13$ one.

to the parent CdI_2 direction. It seems not unlikely, since the octahedral sandwiches in the 4Hb polytype (6R is similar) are regularly spaced by trigonal prismatic sandwiches, that the superlattice distortion might alternate in sense with each successive octahedral sandwich. Indeed the 'balanced' pattern of fig. 9 (ii) is obtained from the thinnest of samples, and is independent of the crystal quality. (4Hb is sometimes heavily dislocated.)

Relevant to this matter, it was observed in our heating experiments on 1T-TaSe₂ (and -S₂) that if the samples were cooled from temperatures at which random conversion of individual sandwiches through to trigonal prismatic coordination had begun, transfer into a 4Hb-like diffraction pattern could be obtained. It appears that a converted sandwich disrupts the communication between its flanking octahedral regions (or at least alters the sense of that communication), so that whole blocks of α rotation occur above blocks of β rotation. Such patterns are often rather badly moiréd (by internal slip), and frequently they show rather faint spotting at all points of the reciprocal lattice corresponding to $13a_0$. (Compare fig. 19 (i) for light Ti doping.)

A further revealing complication is portrayed in fig. 9 (iii). This picture was taken a little above T_d . It shows that while much of the sample is in the high temperature régime, there lies superimposed on that pattern just one of the low temperature $\sqrt{13}a_0$ patterns†. We can only suggest that the sample contains just octahedral sandwiches at some level, and for the latter one is still below T_d . It should however be remembered here that the low temperature diffraction pattern for pure 1T-TaS₂ is not *normally* so simple (see fig. 7 (iv); attention is also brought to figs. 12 (i) and 12 (v)).

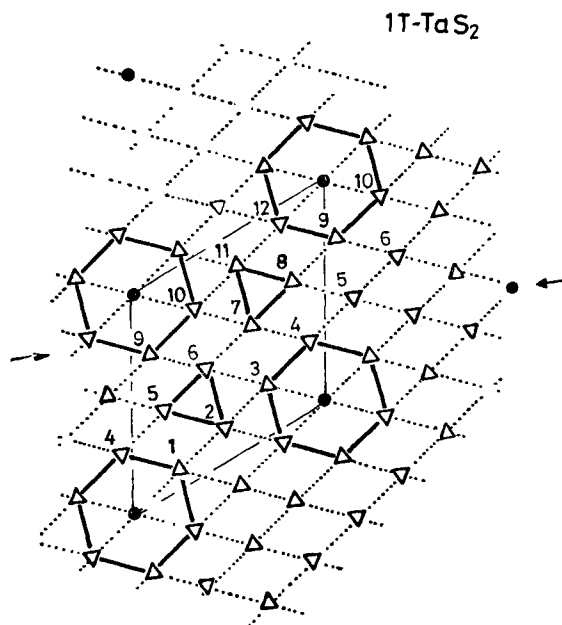
Immediately apparent from fig. 9 (iii) is that the circle of type-1 spots is in the 4Hb case somewhat smaller in radius than the ideal $a_0^*/\sqrt{13}$; by -5% in fact (see table 2), to be contrasted with +3% for 1T-TaSe₂ (or -S₂). None of the 4Hb samples when taken into the high temperature phase (fig. 9 (iv)) show those extra fairly sharp spots of types 2 and 2', noted above for both pure 1T-TaSe₂ and 1T-TaS₂. Moreover, the intensity of both the diffuse scattering and of the type-1 satellite spots is less than for the 1T materials. This implies smaller atomic displacements in the 4Hb material.

(c) 1T-TaS₂

As regards the high temperature phase there is no difference between 1T-TaS₂ and 1T-TaSe₂, apart from the fact that the selenide is more prone to undergo inter-polytypic conversion. The room-temperature diffraction from 1T-TaS₂ is much more complex however (see fig. 7 (iv)). The details of this pattern are expounded in figs. 17 and 18. Each spot of the selenide pattern is replaced by a cluster of four spots in the form of a centred equilateral triangle. However, the centring spot does not fall exactly at the $\sqrt{13}$ site. The triangles are of two types: namely, neighbour to a CdI_2 lattice point (type *a*), or not so (type *b*). The centring spot for the former is more nearly 'ideal' than for the latter (see fig. 18). The sides of all the triangles have a common inclination relative to the main a_0^* spots. At 300°K this is approximately '3 by 2'

† The double transition seen by DTA (Di Salvo *et al.*, 1973) in 4Hb-TaS₂ could derive from this or a related situation.

Fig. 17



Representation of repeat details in 1T-TaS₂ (300°K) superlattice diffraction pattern. Expanded view of a_0^* unit is given in fig. 18. The heavy hexagons incorporate type a superlattice sites, the triangles type b .

(i.e. $23^\circ 25'$); the *arms* of the triangles then roughly bisect the \mathbf{a}_0^* and 1T-TaSe₂ \mathbf{a}^* directions. As the temperature is raised towards the 350°K transition, the triangular clusters smoothly grow in size and twist to a significantly different orientation with respect to the a_0^* spotting (see fig. 24 (vi)). In this process there appears to be some loss of hexagonality in the array of fine spots 'decorating' the triangle-centring spots.

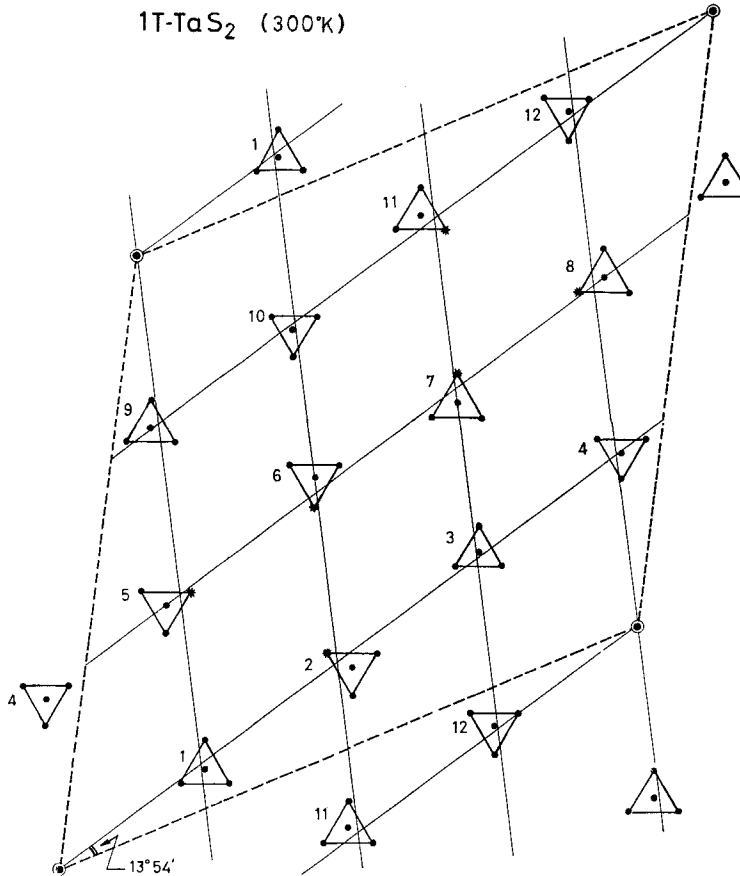
Specimens of 1T-TaS₂ for all thicknesses and all preparative variants show the same details, and these details regenerate upon cycling through T_d . The definition of the pattern is however very sensitive to specimen tilt. Only when carefully centred with the aid of the Kikuchi bands do the basic CdI₂ spots flare out as in fig. 7 (iv). Moreover, when so positioned, a corner spot in the type b triangles also flares strongly, emphasizing the larger triangular grouping evident in fig. 7 (iv), and giving the impression of very non-collinear strings of spots. When the specimen is tilted slightly ($\sim 5^\circ$), the clear systematics of the pattern rapidly disappear, the pattern fuzzing out in ribs. Moreover, where sharp spots remain, some of the small triangles are added to by further spots, so that

$$\begin{array}{c} \cdot \\ \vdots \\ \cdot \end{array} \text{ becomes } \begin{array}{c} \cdot \\ \vdots \\ \cdot \\ \cdot \end{array} \text{ or } \begin{array}{c} \cdot \\ \vdots \\ \cdot \\ \cdot \\ \cdot \end{array} \text{ or } \begin{array}{c} \cdot \\ \vdots \\ \cdot \\ \cdot \\ \cdot \\ \cdot \end{array}$$

Figure 24 (v) corresponds to a specimen tilt of about 15° .

The various spots in the 1T-TaS₂ superlattice patterns are too close together to permit satisfactory dark-field work even with a 10μ aperture.

Fig. 18



Details of diffraction pattern from 1T-TaS₂ in quasi-superlattice state at 300°K. The spots within the clusters around the type-*b* sites, that are marked by a star flare strongly when the pattern is Kikuchi-centred upon the *c*-axis pole. Neither type of cluster places its centre spot exactly at the $a_0^*/\sqrt{13}$ points. These details are a function of temperature (see text).

The dark-field patterns (see fig. 10 (vi), (iv)) obtained when trying to image in the $\sqrt{13}a_0$ superlattice 'spots' show a remarkable grainy contrast, not apparent for the selenide where those spots are not composite.

So far only one run has been made through the low temperature (200°K) transition of 1T-TaS₂. The diffraction pattern is found to lose these complexities, the detailed origin of which is not yet clear.

The complex pattern from 1T-TaS₂ has many of the characteristics of double diffraction (where spots with zero structure factor can appear), but it is not likely that out of all the layer materials such an occurrence would be confined to 1T-TaS₂. Further discussion of the fine detail in the room-temperature 1T-TaS₂ pattern pattern is given in § 5.2 (e).

(d) Trigonal prismatic polytypes

In fig. 7 (v) we showed that the low temperature phase of 2H-TaSe₂ involves the formation of a $3a_0$ superlattice, and, while it is not yet proved, it is quite probable that this is common to all the polymorphs 2H, 3R, 4Hc of TaSe₂, TaS₂, and NbSe₂. Certainly the anomalies in χ , ρ , S , R_H , etc., outlined in § 1 (and re-examined in § 7), are all very similar for this group.

The $3a_0$ superlattice spotting in 2H-TaSe₂ is of very low intensity, and shows clearly only when the neighbouring a_0^* spots are strongly excited, this indicating that the superlattice lies in the $l=0$ plane. The apparent absence of a superlattice spot at the centre of the triangle defined by the a_0^* spots further indicates that the modulation defining the superlattice is very slight. The intensity of these points should in part be due to overtones (i.e. combinations) of the basic $(\frac{1}{3}, 0, 0)$ and $(0, \frac{1}{3}, 0)$ satellite spots (see § 7). The latter spots gain perceptibly in intensity for some 40° below the first appearance of sharp spotting ($T_0 = 120^\circ\text{K}$ for 2H-TaSe₂). For 60°K above this temperature diffuse scattering is observed about the $(\frac{1}{3}, 0, 0)$ points (see fig. 7 (vi) (a)). Both these observations indicate second-order behaviour. Worthy of note is the extent of the critical scattering, (viz. to $\frac{1}{2}T_0$). Indeed, this diffuse scattering can be observed at room temperature, following either incorporation of tantalum excess in the van der Waals gap region (as in Ta_{1.08}Se₂, fig. 7 (vi) (b)), or substitution of tungsten for tantalum within the sandwiches (as in Ta_{0.92}W_{0.08}Se₂). Electrical and magnetic measurements are underway to follow any associated shifts in T_0 , and to see whether these effects are a function of 'e/a'.

Intercalation of 2H polymorphs with Lewis base organics, such as pyridine, acts to suppress the above anomaly (Thompson, Gamble and Koehler 1972, Di Salvo 1972, Revelli 1973 (Ph.D. Thesis), Murphy *et al.* 1974), as observed in χ , ρ and R_H . Electron diffraction however often reveals a host of ordered and partially ordered states, but these seem to relate to the intercalate in its varying stages of deintercalation (see fig. 22 (iv)). When in the fully ordered condition, using pyridine, it is nevertheless clearly significant, with regard to the chalcogenide matrix, that the basal plane cell dimensions are a rectangular $2\sqrt{3}a_0$ by $13a_0$ (Parry *et al.* 1974), while for cyclopropylamine the same hexagonal $\sqrt{13}a_0$ cell occurs that we have met for 1T-TaS₂ (or possible $\times 2$, Beal and Liang 1973, fig. 10). Thus, as will become apparent particularly through the results of § 2.2 (g), there is considerable interaction between the structural instability of the host and the geometric ordering pattern favoured by (at least some) organic intercalates.

For inorganic 2H intercalates, however, such as iron (fig. 22 (v)) or sodium (Carter and Williams 1972), the observed superlattices usually seem due to a simple, geometric ordering of the intercalate, although tin does show a complex, unresolved pattern (fig. 22 (vi)). The two patterns reported by Carter and Williams for ammonia intercalated 2H-NbSe₂ are very interesting. Although the extra spotting in their partially intercalated samples ($x \simeq 0.40$ and 0.60) appears to bear an arbitrary relation to the matrix spotting, patterns of this type were reported to come also from material that had never been intercalated. The latter material showed heavy concentration of growth defects. This serves to warn against always interpreting the observed superlattice as coming from ordering of the intercalate. The $2a_0$ superlattice reported by Beal and Liang

(1973) for 2H-TaSe₂ + aniline is probably a case in point. This superlattice we often observe in chalcogen-poor material that, again, has never been intercalated. In fact aniline is known to extract chalcogen as it de-intercalates spontaneously at 300°K (A. H. Thompson *et al.*, to be published); ammonia does likewise, substantially reducing the 2H low temperature anomaly. In fig. 19 (vi) we show a sample of 'pure' 2H-TaSe₂ locally passing over from the simple structure to a 2a₀ superlattice (300°K). Figure 19 (v) shows the 2a₀ superlattice to be thermally controlled, perhaps in a similar way to the 3a₀ superlattice described earlier. The relation between the two superlattices will be discussed in § 7, in terms of probable changes in the Fermi surface geometry. The effects of intercalation are returned to in § 2.2 (g) and §§ 6 and 7.

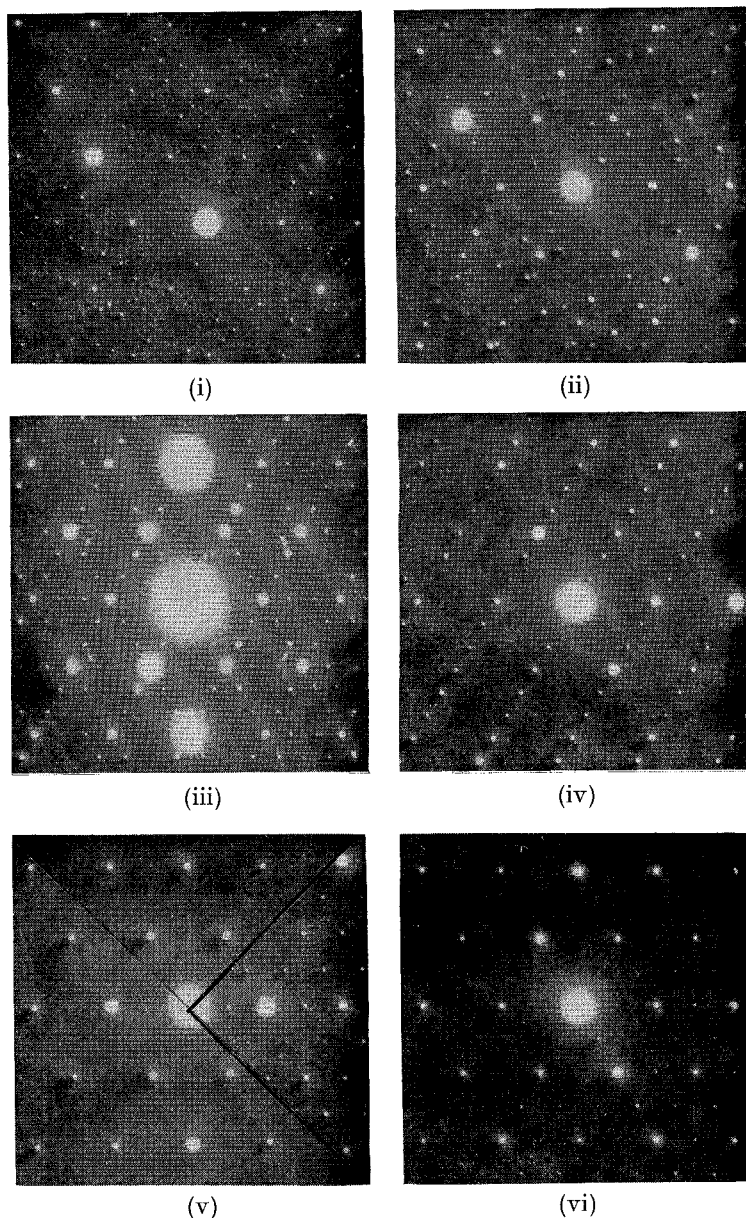
(e) 6R-TaS₂

Powder samples were kindly provided by R. B. Somoano and A. Rembaum of the Jet Propulsion Laboratory, Pasadena, California. These contained some small crystallites of up to 1 mm diameter which were adequate for electron diffraction studies. X-ray diffraction and magnetic susceptibility measurements indicated that the (powdered) material was contaminated by approximately 10 to 15% of other polymorphs, primarily 2H and 1T. The susceptibility of the material showed a 10°K broad transition centred at 315°K, apparently deriving from the 6R content, this being the same temperature as for the transition in 4Hb-TaS₂, the other mixed coordination polytype (see fig. 1). No further anomaly was detected in χ near 20°K, however, unlike 4Hb-TaS₂ (fig. 8). As one can see from plates (iv) to (vi) of fig. 12, the electron-diffraction patterns obtained are indeed similar to those obtained from 4Hb-TaS₂. Extra spots appear in these patterns at ($\frac{1}{2}$, 0, 0) and ($\frac{1}{3}$, 0, 0), which are not seen for good 4Hb material. This may be due to stoichiometry problems, or possibly defects in the stacking arrangements, such as having several trigonal prismatic sandwiches together. Because the transition is not as sharp as for 4Hb, pictures like fig. 12 (v), of a high temperature/low temperature pattern superposition, can be readily obtained. It is immediately apparent from this figure that the first-order high temperature satellites lie closer to the main spotting than the $a_0^*/\sqrt{13}$ of the superlattice, by a ratio somewhat in excess of $\cos^{-1} 13^\circ 54'$ (or 0.97)—in fact by 5.2%, as for 4Hb.

(f) Mixed crystals

Work on mixed systems has opened up a variety of interesting aspects; but so as not to overload the present paper most of this will be reported separately. A comparatively simple and most illuminating substitution has been that of Ti for Ta. In this article we will focus on 1T-Ta_{1-x}Ti_xS₂ and 1T-Ta_{1-x}Nb_xS₂. The electronic and optical properties of the series 1T-Ta_{1-x}Ti_xS₂ have already been reported (Thompson, Pisharody and Koehler 1972, Benda 1974). Ti substitution allows the average 'e/a' number for the conduction electron system to be decreased continuously from 1 to 0, without at the same time markedly distorting the crystal lattice. The molar volumes of 1T-TaS₂ ($T < T_d$) and TiS₂ differ by only $\frac{1}{2}$ % (57.80 and 57.12 Å³ respectively), though the compounds do have the significantly different c/a ratios

Fig. 19



Stages in the destruction of the 1T phase by thermally promoted interpolytypic conversion (see fig. 11): 1T-TaSe₂. (i) (300°K, following short period at 500°K). A great many spots falling on $a_0^*/13$ net are apparent. This is characteristic of faulted crystals. (ii) (300°K, following 1 hr at 450°K.) One of the hexagonal axes has become tripled, relative to standard $\sqrt{13}a_0$. (iii) (500°K, following 1 hr at 450°K.). Besides standard structure modulation spots of h.t. phase, spots corresponding to $2a_0$ and $3a_0$ also apparent. Plate (ii) was regained from this condition. (iv) (Held at 550°K.) Virtually converted to trigonal prismatic coordination. Shows triple spotting of one a_0 axis. (v) (Held at 550°K.) Final plates of sequence: (a) diffuse $2a_0$ scattering at 550°K, (b) sharp $2a_0$ superlattice spotting, when cooled to 300°K. (vi) (300°K.) Same $2a_0$ superlattice appearing towards edge of an as-grown 2H sample.

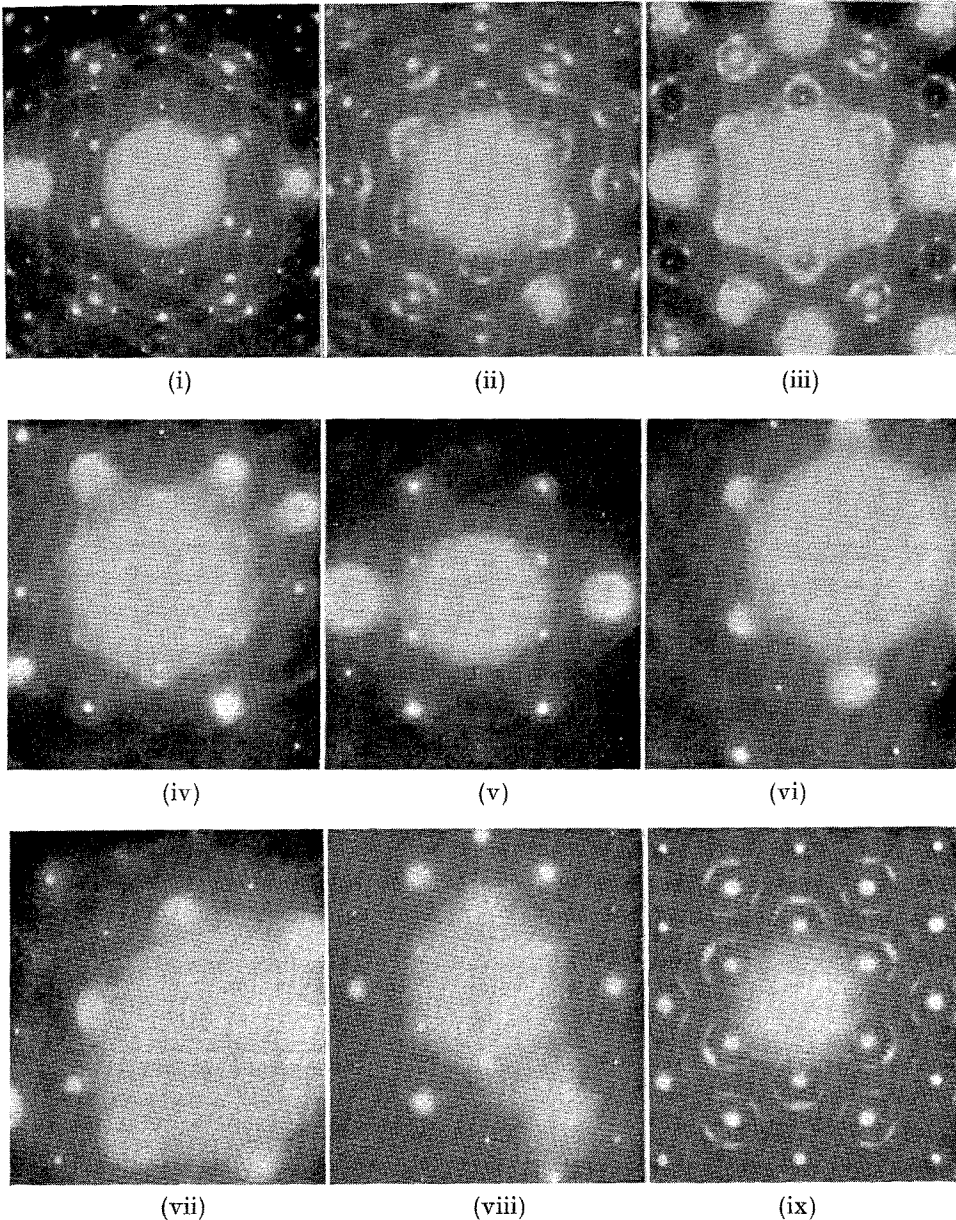
of 1.75 and 1.67, the a_0 values being 3.365 and 3.405 Å respectively. The crystallographic accommodation demanded by substitution of isoelectronic Nb for Ta is even less, so that in this case, study can be made solely of the effects of the $4d^1/5d^1$ disorder in cation site potential.

In both alloy systems T_d is depressed with increasing x , at a rate somewhat faster than linear, but which approximates in each case to $10^\circ\text{K}/\text{atomic } \%$. (The details of the electronic and magnetic properties at low x will be reported separately.) The transition quickly broadens as x increases, becoming essentially undefined for $x \gtrsim 0.15$. The energetically slighter transition occurring at 200°K in pure 1T-TaS_2 is completely suppressed by as little as $\frac{1}{2}\%$ Ti substitution. Moreover, the resistivity in all the 1T alloy systems remains anomalous at large x , and indeed up to about $x = 0.5$, ρ continues to increase for decreasing temperature (see Thompson, Pisharody and Koehler 1972).

A selection of electron-diffraction patterns for these systems is collected in figs. 20 and 21. The results of fig. 20 will be analysed at length in § 6. For Nb doping of 1T-TaS_2 , although T_d is depressed (it falling to room temperature for 8% Nb), the magnitude of the low and high temperature structure modulations throughout remains virtually unchanged at (effectively) $\sqrt{(13)}a_0$. The sharp satellite spots of the high temperature phase are rapidly smeared out (by $x \sim 15\%$ Nb), leaving the two interlocking sets of rings of diffuse scattering, stronger even than before. By only 8% Nb doping the potential disorder appears so severe that no trace is found of any second-order (types 2 and 2') spotting (fig. 21 (ix)). Surprisingly this contrasts with the case for comparable doping by Ti (see fig. 21 (vi)), despite the fact that the depression of T_d is virtually the same as for the Nb case. However, contraction of the structure-modulation spotting back towards the main a_0^* spotting is the most striking feature through the Ti alloys; a feature not found in the Nb-doping case. The first-order (type 1) satellites, although becoming somewhat diffused, are still evident even with 50% Ti doping, whilst the associated rings of diffuse scattering, though weakening in intensity, persist right through to TiS_2 itself. The rings do not appear to be due to short-range crystallographic order, since annealing a sample with 85% Ti for several days yielded little change in their definition. As was apparent in fig. 13 for pure 1T-TaSe_2 , the radii of the large and small circles are found to adjust throughout the series so that their sum remains close to a_0^* .

For the 'high' temperature phase there is little difference in behaviour between the sulphide and the selenide alloys, $1\text{T}-(\text{Ta}/\text{Ti})\text{X}_2$. For the low temperature phase, however, there are several differences of detail in the diffraction patterns. Differences are also picked up in the ρ and χ versus T behaviour below 300°K . It is clear they are associated with the fine structure observable in the room-temperature pattern for pure 1T-TaS_2 , and largely retained following suppression of the low temperature transition at 200°K (e.g. fig. 21 (iii)). This topic is returned to in §§ 5 and 6. At the present stage we might point out the difference between the Ti-doped selenide fig. 21 (ii) and the sulphide fig. 21 (iv). The latter contains some of the complexities to be found in fig. 21 (vii) for $1\text{T}-(\text{Ta}/\text{Nb})\text{S}_2$. One notes in such sulphide plates both a loss of hexagonality for trigonality in the pattern of 'superlattice' spotting, and the complex manner in which the details of the 1T pattern are accommodated.

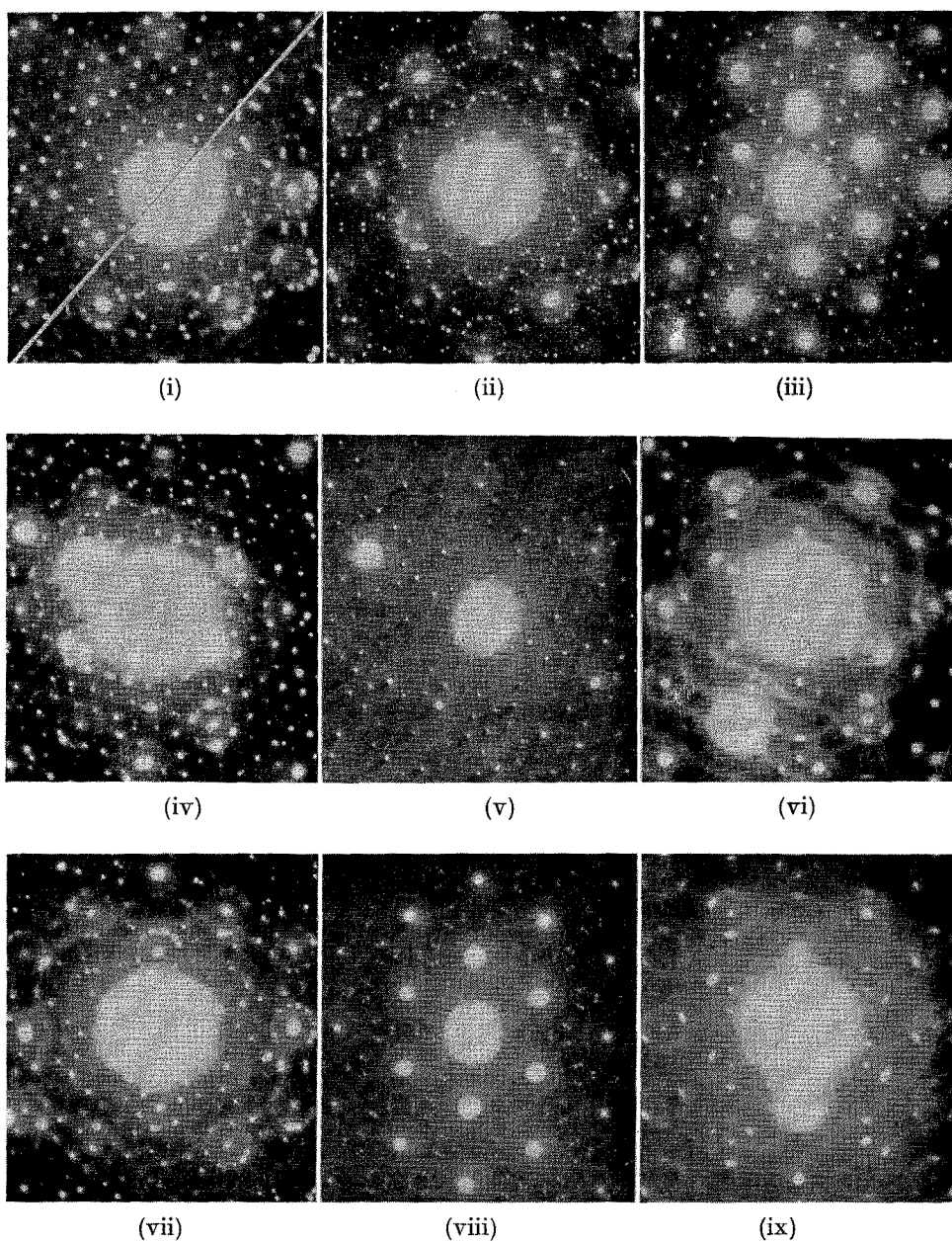
Fig. 20



Changes in the e/a -dependent features of the 1T diffraction pattern (outside the $\sqrt{13}a_0$ superlattice region). (i) 1T-TaS₂, 370°K; (ii) 1T-Ta_{0.6}Nb_{0.4}S₂, [at 300°K, as are remaining plates]; (iii) 1T-Ta_{0.7}Ti_{0.3}S₂; (iv) 1T-Ta_{0.5}Ti_{0.5}S₂; (v) 1T-Ta_{0.3}Ti_{0.7}S₂; (vi) 1T-Ta_{0.15}Ti_{0.85}S₂; (vii) 1T-V_{0.1}Ti_{0.9}S₂; (viii) TiS₂; (ix) 4Hb-TaS₂·EDA_{1/4}. The crystals for plates (iii) and (v) were kindly provided by J. Benda, those for plate (ix) by S. Meyer, and for plate (viii) by A. H. Thompson. The latter TiS₂ crystals are of good stoichiometry, but still show interspot streaking. The EDA intercalated plate (ix) shows $3a_0$ spotting in the rings, i.e. $q_0'/a_0^* = 0.33$ (see fig. 22 (i) and fig. 23 (a)). In addition to the virtually unchanged ring size in (ii) relative to (i), note that the second-order spotting is gone (true for $\gtrsim 8\%$ Nb).

For 4Hb-like patterns such as fig. 21 (ii) to have been recorded, it is presumed that the dimensions of the α/β superlattice domains are reduced by the doping to such an extent, that, with the 10 micron aperture used, this additive pattern is yielded. It is probable that local variations in Ti concentration significantly change the local value of T_d , so that there is not a single co-operative adoption of α or β orientation for the superlattice throughout the crystal. X-ray fluorescence analysis indeed has revealed that the Ti content

Fig. 21



varies somewhat from crystal to crystal within a single growth batch. The many extra spots of the $a_0^*/13$ array present in fig. 22 (ii) and the very marked blobs, not spots, on fig. 21 (i) (b) are also indicative of somewhat faulted material. Finally we note in fig. 21 (viii) a remarkable suppression of the inner (type *a*) spots occurs, and the type *b* spots falling in parallel hexagonally arrayed pairs, as with real 4Hb material. This signifies that the doping has produced a change in the *c*-axis spot coordinates.

The behaviour of vanadium-doped TiS_2/Se_2 , and of d^{1V}Se_2 with respect to its low temperature transition at 110°K , can be interpreted within the present framework. We will treat separately some of these very interesting vanadium-containing compounds. Not presently understood are the properties of TiSe_2 and TiS_2 (A. H. Thompson, B. G. Silbernagel, to be published), and in particular the source of the very high conductivity in TiS_2 , which by all theoretical counts should be a semiconductor. The interspot streaking evident in fig. 20 (viii) suggests that some type of structural defect provides the carriers in this d^0 material. The specimen used was of good Ti : S stoichiometry. It was, however, noted to be peculiarly devoid of dislocations. Since it is very easy to cleave, it would not seem to have metal atoms in the van der Waals gap region, unlike many vanadium-doped products.

(g) Intercalated materials

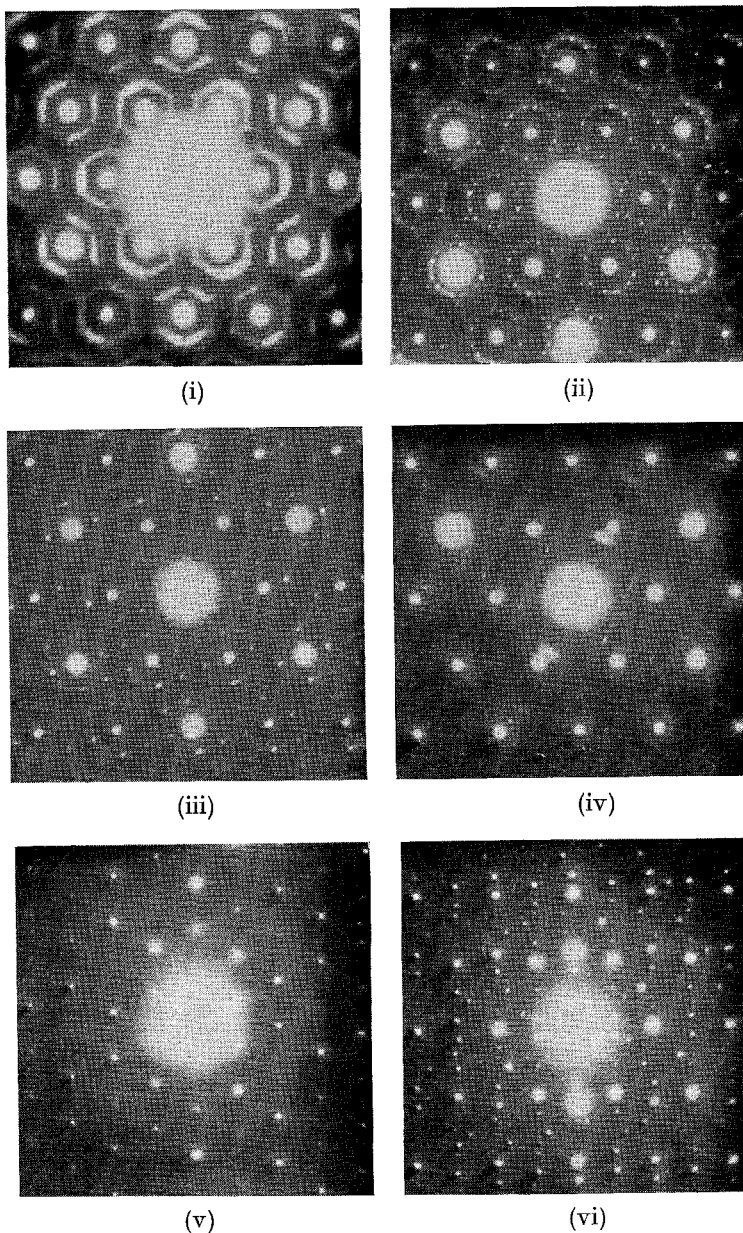
While many organic materials form stable intercalation products with the trigonal prismatically coordinated polymorphs of TaS_2 (see, for example, Gamble *et al.* 1971), only very few can be intercalated into 1T or 4Hb- TaS_2 . Ethylene diamine ($\text{NH}_2\text{CH}_2\text{CH}_2\text{NH}_2$) is one such (Meyer 1974). Crystals of 1T- $\text{TaS}_2 \cdot \text{EDA}_{1/4}^\dagger$, 4Hb- $\text{TaS}_2 \cdot \text{EDA}_{1/4}$ and 2H- $\text{TaS}_2 \cdot \text{EDA}_{1/4}$ were provided by Meyer. Since each polytype shows the same interlayer expansion, and has

Fig. 21

Diffraction pattern complexities developed in cation substitutional doping ($<10\%$; nominal 'as-grown' values). (i) 1T-(Ta/Ti) Se_2 , (a) 4% Ti-1T-type pattern, (b) 8% Ti-4Hb-like pattern; contrast these well-defined blobs with sharp spots of plate (ii). (ii) 1T-(Ta/Ti) Se_2 , 4% Ti. This 4Hb-like pattern has many extra spots falling on a $1/13a_0^*$ array—a feature characteristic of defect material (see fig. 19 (i)). (iii) 1T-(Ta/Ti) S_2 , 2% Ti. The definition of the small triangular spot clusters is much reduced relative to pure 1T- TaS_2 . (iv) 1T-(Ta/Ti) S_2 , 4% Ti. This 4Hb-like pattern shows in parts the complexities seen in plate (vii) for Nb-doping. (v) 1T-(Ta/Ti) S_2 , 6% Ti. Complex multispotting of sulphide degenerating towards ' $\sqrt{13}a_0$ ' superlattice of selenide. (vi) 1T-(Ta/Ti) S_2 , 6% Ti. Same sample taken above T_d (305°K). Shows diffuse 1st and 2nd order spotting. From latter $q_0'/a_0^* = 0.276$, to be compared with 0.288 for pure 1T- TaS_2 . (vii) 1T-(Ta/Nb) S_2 , 2% Nb. Transfer from 1T to 4Hb-like pattern. However, latter array is trigonal, not hexagonal, with much disruption. (viii) 1T-(Ta/Nb) S_2 , 8% Nb. Remarkable suppression of inner ring spotting, with second ring of spots sharp and now forming parallel pairs, as for actual 4Hb pattern. (ix) 1T-(Ta/Nb) S_2 , 8% Nb. h.t. condition in different area of same crystal. ($T_d \approx 300^\circ\text{K}$.) $q_0'/a_0^* = 0.276$, much as for 15% and 40% Nb. Additional blobs in large circle also given by 15% Ti doping.

† The 1T- TaS_2 is actually converted from a '1T' (CdI_2) type stacking to a '3R' (CdCl_2) stacking.

Fig. 22



Some patterns from intercalated materials (300°K); concentrations nominal. (i) $4\text{Hb-TaS}_2 \cdot \text{EDA}_{1/4}$. Diffuse ring $q_o'/a_o^* \equiv 0.354$; contrast fig. 20 (ix), where more EDA had been driven out by beam heating. (ii) $4\text{Hb-TaS}_2 \cdot \text{EDA}_{1/4}$. In certain areas this ordered pattern was found; the origin of the 'tabs' on the diffuse rings of plate (i) is apparent. (iii) $4\text{Hb-TaS}_2 \cdot \text{EDA}_{1/4}$. Plate (ii) is a symmetric triple addition of this single orientation pattern, which is analysed in fig. 23. (iv) $2\text{H-TaS}_2 \cdot \text{pyr}_{1/2}$. This intercalation process, unlike the above, leads to very complex order patterns, that change during deintercalation. (v) $\text{Fe}_{1/3}\text{TaS}_2$ (trig. pr.). The superstructure, due to intercalate ordering, is here distorted from the standard hexagonal $\sqrt{3}a_o$ pattern. The honeycomb streaking probably reflects the poor stoichiometry. (vi) $\text{Sn}_{1/3}\text{TaS}_2$ (trig. pr.). Much more complex ordering.

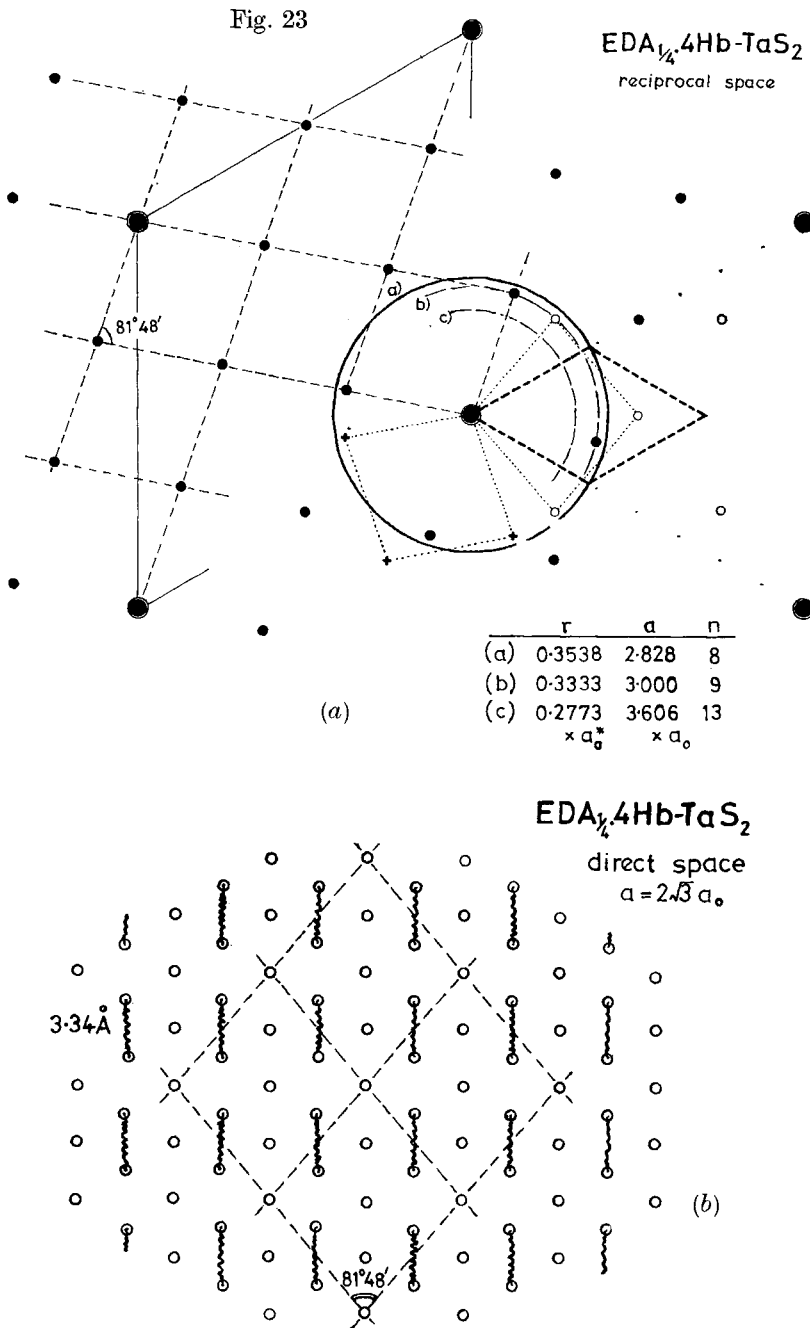
the same stoichiometry, we conclude that the EDA arrangement is similar in each. Actually it is found that one can reduce the local EDA content in the crystals merely by beam heating in the electron microscope.

When an organic donor intercalates TaS_2 , the electron concentration in the TaS_2 sandwich is known to increase. It is not known, however, if the degree of donation to trigonal and octahedral sandwiches differs. Qualitatively, however, we did anticipate that the intercalation would cause q_0/a_0^* to increase, the reverse effect to that secured by group IV substitutional doping. While $2\text{H-TaS}_2 \cdot \text{EDA}_{1/4}$ continues to show the normal (2H) diffraction pattern (with just a small amount of a_0^* -axis streaking; $\sim 300^\circ\text{K}$), we indeed do find for the 1T and 4Hb materials diffuse 'ring' patterns, as shown in figs. 20 (ix) and 22 (i). The former, from a partially deintercalated sample, corresponds even so to a substantially augmented q_0'/a_0^* ratio of 0.33. Actually spotting derived from a $3a_0$ hexagonal superlattice is discernible within these rings. The second plate comes from virgin material, and has a q_0'/a_0^* ratio of close to 0.35 ($\approx 1/\sqrt{8}$). In certain areas of such a specimen the diffuse rings give place to the spotting pattern of fig. 22 (ii), from which it is apparent why the diffuse rings of the previous plate (22 (i)) carry 'tabs'. Still further areas reveal that this complex hexagonal pattern of spotting (fig. 22 (ii)) results from a symmetric addition of three non-hexagonal patterns of the type shown in fig. 22 (iii). As is portrayed in fig. 23 (a), this non-hexagonal superlattice is defined, within the hexagonal matrix, by the operations ('2-by-1') $\div 8$ in conjunction with ('1-by-1') $\div 4$, yielding eight lattice points per a_0^* cell. The corresponding direct space cell is shown in fig. 23 (b), this containing eight tantalum atoms and two EDA molecules (per sandwich). The EDA molecule is of just the appropriate length to employ both its electron-donating amine groups in the manner that the illustrated form of molecular ordering would imply. It is clear that the q_0'/a_0^* ratio simultaneously attained in the TaS_2 sandwiches favours this same size of cell, a point returned to in § 6.4. The discontinuity reported in ρ versus T just above room temperature by Meyer (1974) for the $\text{EDA}_{1/4}$ complex of 1T- TaS_2 is presumably due to the disappearance of this superlattice state.

Even after subtraction of the organic contribution, the above material is still somewhat *more* diamagnetic than pure 1T- TaS_2 . For the case of EDA intercalated 4Hb- TaS_2 it appears that the octahedral sandwiches continue to possess only a very low paramagnetic component, whilst its trigonal prismatic sandwiches seem to remain quite paramagnetic (though not so markedly as in pure 2H- TaS_2) (Di Salvo 1974, unpublished). [Note through the series of 2H-intercalates-collidine $_{1/6}$, -picoline $_{1/3}$, -pyridine $_{1/2}$, -EDA $_{1/4}$, and -aniline $_{3/4}$, the paramagnetism is progressively reduced, while T_0 is smeared out and forced to somewhat higher temperatures (see Di Salvo 1972, fig. 10).] We return to discuss just what effects organo-intercalation might be having on the band structure of the host in § 6.

(h) Tilt experiments

In order fully to interpret the diffraction patterns more information is needed. First we need to clarify the effects on the observed diffraction pattern of using thin crystals. Secondly, we would like to obtain definite information concerning other reflection planes than just ($hk0$).



Analysis of fig. 22 (i), (ii), (iii) from $4\text{Hb-TaS}_2 \cdot \text{EDA}_{1/4}$. (a) The non-hexagonal reciprocal cell shown to the left corresponds to a superlattice of 8 Ta sites per cell (per sandwich). The hexagonal cell to the right associated with ring 'a'—see fig. 22 (i)—has the same area. The three symmetry related superlattice cells shown in this region are marked, ●, ○ and +. (b) Likely ordering of the 'bidentate' EDA molecule to yield the above supercell at the stoichiometry $\text{EDA}_{1/4}$. It is not known whether all molecules in a given vdW gap attach themselves to the same sandwich.

Diffraction from thin samples is represented by elongated regions in reciprocal space, in contrast to spots for thicker crystals. Elongation will for the present materials occur along the k_z axis. The diffracted intensity decreases from the centre of the elongated spot approximately as (Guinier, 1963, Chap. 5)

$$I(k_z/c_o^*) \approx \frac{I_o}{(k_z/c_o^*)^2 N^2}, \quad \left(\frac{k_z}{c_o^*} > \frac{1}{N} \right),$$

where k_z/c_o^* = distance from spot centre (in units of c_o^*), N = number of c_o units in sample thickness. Thus if $N \sim 100$ (i.e. a 600 Å thick crystal), $I(\frac{1}{3}) \sim 10^{-3} I_o$. Since double diffraction is prevalent in electron scattering, I_o can be an appreciable fraction of the initial beam intensity, and a 'spot' centred on the ($hk0$) plane could possibly show right through into the (hkl) plane, and vice versa.

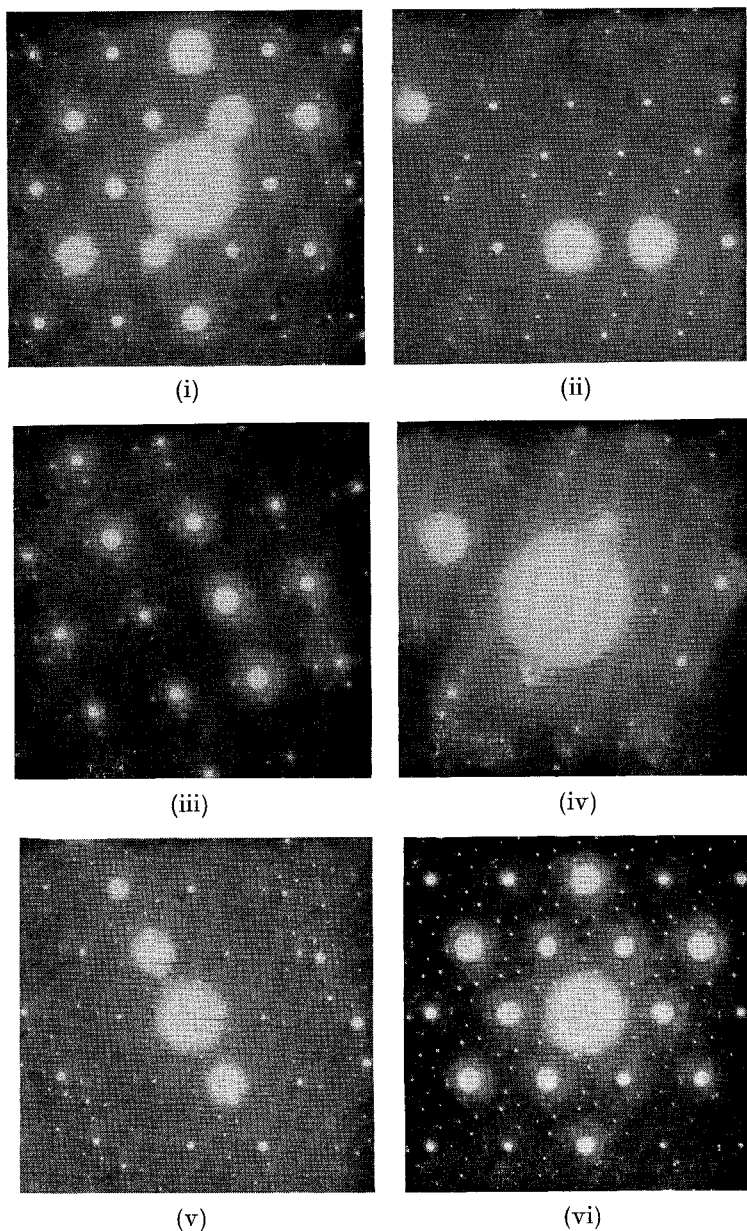
When the spots are not too severely elongated, we can study in more detail the effects of structure modulation, and the possibility of non-hexagonal distortions, by tilting the sample normal with respect to the electron beam. We then obtain diffraction patterns corresponding to intersections of the 'horizontal' viewing plane with the scattering map for the tilted reciprocal lattice. For our typical sample thickness we find that the a_o^* spots are not so elongated as to reach right through from the $l=1$ to $l=0$ plane. However, one does find that many of the extra spots appearing in the $hk0$ plates are not in fact centred upon the $l=0$ plane, but upon planes translated along k_z by some fraction of c_o^* .

A most revealing configuration of satellite spotting is found for the 1T compounds when $T > T_d$. [We have in fact made our tilt experiments on Ti-doped material for which T_d is depressed below room temperature, because large tilts were not attainable in our heating stage. The results we show below are for 1T-Ta_{0.91}Ti_{0.09}S₂, for which $T_d \approx 240^\circ\text{K}$ (see § 6). Since the $\theta=0^\circ$ patterns ($hk0$ plane) are, in character, identical to those obtained from pure 1T-TaS₂ for $T > T_d$, the results shown here most likely do apply to TaS₂ itself.] Figure 24 (i), where $\theta=0^\circ$, demonstrates that only the type 2' spots of the triangular cluster lie in the $l=0$ plane (in addition of course to the main a_o^* spotting). To locate the remaining spots, a crystal of about 2500 Å in thickness was used, and 11 $\bar{2}0$ selected as tilt axis (see fig. 25). The patterns of figs. 24 (iii) and (iv), obtained when the tilt angles were $+50^\circ$ and -30° respectively, indicate that the type 1 spots are in triangular sets of three on planes at $\pm c_o^*/3$ (connected by the operation $\bar{3}$). This accounts for the trigonal distribution of intensity often seen, as in fig. 24 (ii), among the hexagonal grouping of type 1 spots. (This feature is not observed for the 4Hb polymorph.) The type 2 spots follow the same form of distribution as type 1. In § 5.1 we construct a structural model that will generate such diffraction conditions.

§ 3. CONCERNING THE BAND STRUCTURES OF THE 'IDEAL' 1T AND 2H MATERIALS

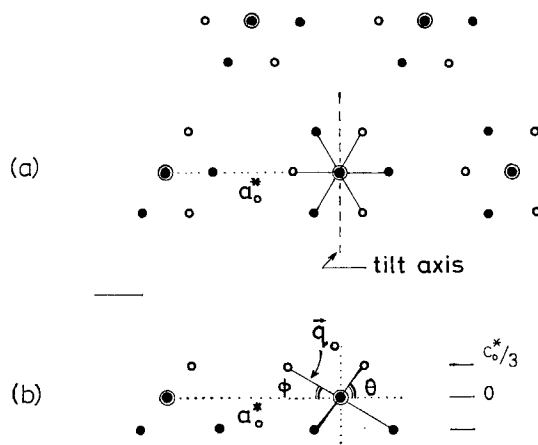
The high density of states at the Fermi level of the 2H metals, as inferred from the electronic heat capacity and magnetic susceptibility, encourages one to seek an interpretation of all the above observations in the band structures and Fermi surfaces of these materials.

Fig. 24



Some effects of tilt and temperature on the 1T patterns. (i) 1T-TaS₂ (370°K). Where close to 0° tilt (samples flexible), the second-order triangular clusters (type 2') of $l=0$ plane show strongly (along with the diffuse circles). (ii) 1T-TaSe₂ (480°K). For this orientation 1st and 2nd order satellites lying outside $l=0$ plane here preferentially excited. (iii) 1T-Ta_{0.91}Ti_{0.09}S₂ (300°K). Viewing plane tilted +50° to intersect four of the first-order satellites on the $\pm c_0^*/3$ planes; ($T > T_d$; axis indicated). (iv) 1T-Ta_{0.91}Ti_{0.09}S₂ (300°K). With tilt of -30° to intersect other two first-order satellites in the $\pm c_0^*/3$ planes (see fig. 25). (v) 1T-TaS₂ (300°K). Degeneration of superlattice pattern upon slight tilting. The main spots are seen to be 'decorated' now. (vi) 1T-TaS₂ (360°K). Both high and low temperature patterns show here. The spot decorating triangles are larger and twisted in orientation relative to room temperature.

Fig. 25



Geometry of first (and zero) order diffraction spotting for 1T incommensurate phase, showing the tilt angles used in obtaining fig. 24 (iii) and (iv).

(a) $hk0$ projection, (b) $h0l$ projection. (See also fig. 30.)

$$\theta \doteq \tan^{-1} \left(2 \cdot \frac{c_o^*}{a_o^*} \cdot \frac{3.5}{3.0} \right) = 49^\circ 24'$$

$$\Phi \doteq \tan^{-1} \left(\frac{c_o^*}{a_o^*} \cdot \frac{3.5}{3.0} \right) = 30^\circ 15'$$

Full *ab initio* band structures along symmetry lines have recently been derived using the APW technique for representative members of the layered transition metal dichalcogenides, assuming undistorted structures (Mattheiss 1973, 1974). These supersede the earlier two-dimensional semi-empirical tight-binding results (Bromley *et al.* 1972, Murray *et al.* 1972, Murray and Yoffe 1972). Of these latter papers, the last has given a reasonably true picture for titanium disulphide, comparing favourably with the recent K.K.R. result of Myron and Freeman (1973). However, for the heavier group IV materials (MBY 1972) an incorrect splitting within the t_{2g} -based d-band had appeared. In the case of the group VI trigonal prismatic materials, the BMY paper foundered in part on the incorrect assessment that the inter-d-band semiconducting band-gap in 2H-MoS₂, etc. be less than 1 eV (Wilson and Yoffe 1969). Now there is sufficient experimental evidence to affirm the new APW results, in asserting that these group VI band-gaps are in fact $\gtrsim 1$ eV. This data will be analysed in detail in the forthcoming review (Wilson 1975). It is sufficient here to say that the initial part of the group VI optical spectra is well matched by the d \rightarrow d-band absorption possibilities of the new 2H calculation, determined in keeping with the selection rules of the full non-symmorphic space group D_{6h}^4 . The earlier 2H calculation did not adequately deal with the crucial inter-d-band hybridization effects (Mattheiss 1973 b), and furthermore, because of its two-dimensional format, it automatically could not reveal those d-band splittings which follow from the fact that here there are two sandwiches per unit cell. The lowest d-band (predominantly d_z^2 at Γ) is particularly

Fig. 26

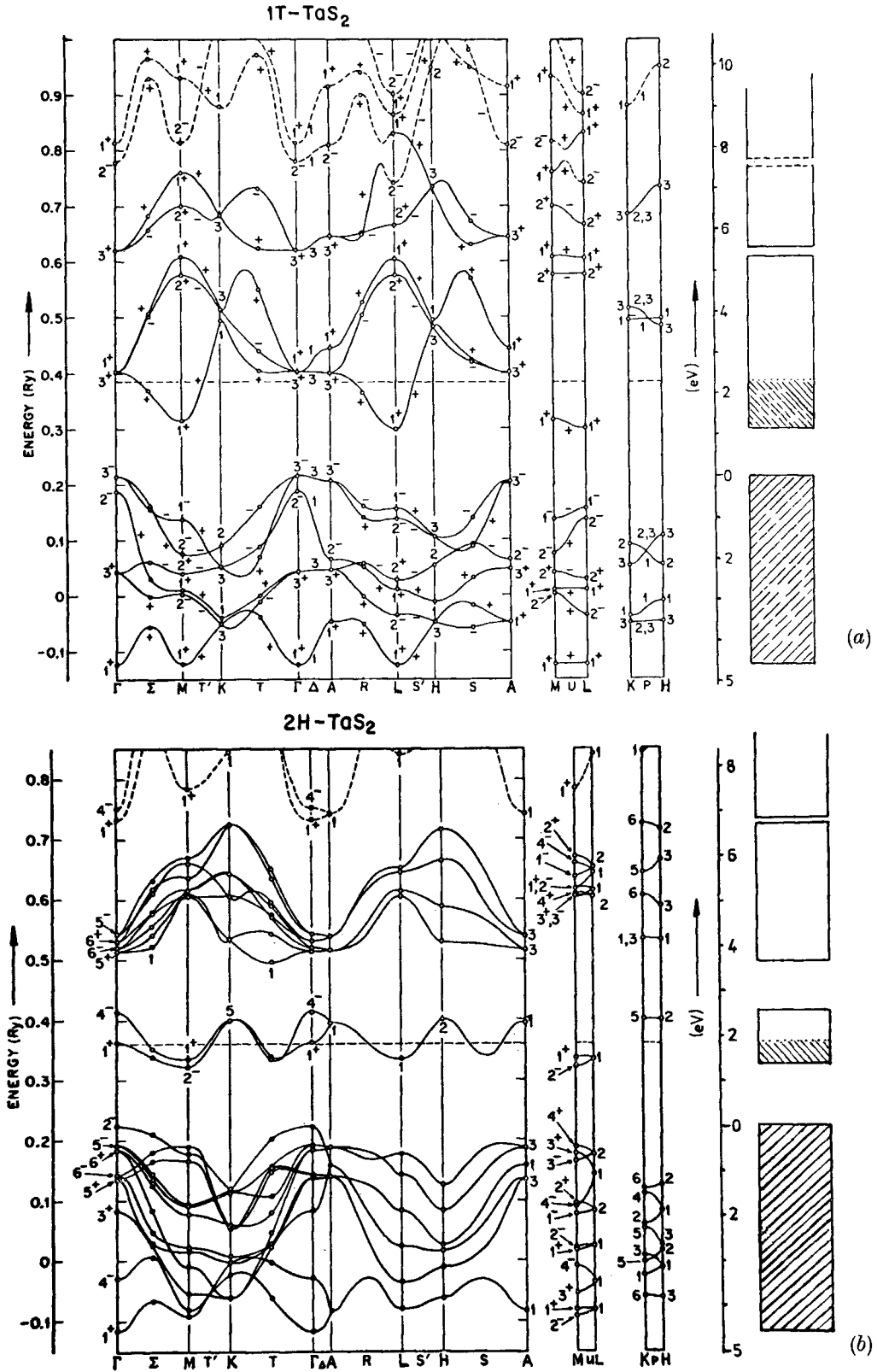
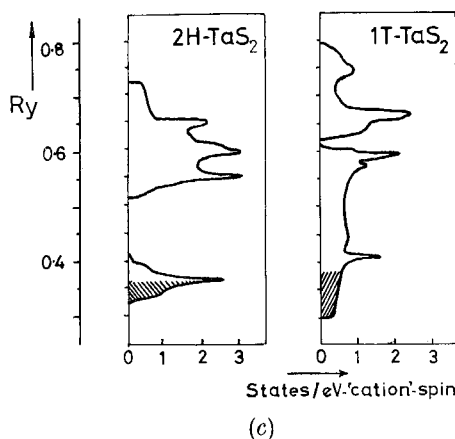


Fig. 26 *contd.*

d-band density of states



(a) Band structure (APW) for 2H-TaS₂, (b) Band structure (APW) for 1T-TaS₂,
 (c) Comparison of d-band density of states (tight-binding) for the 2H and 1T
 polymorphs of TaS₂. [From Mattheiss (1974).]

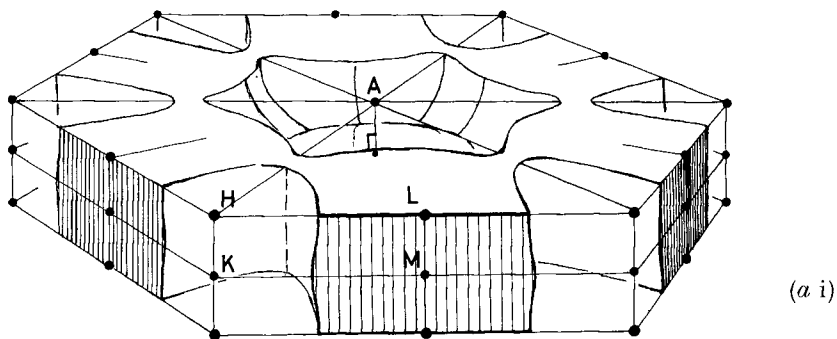
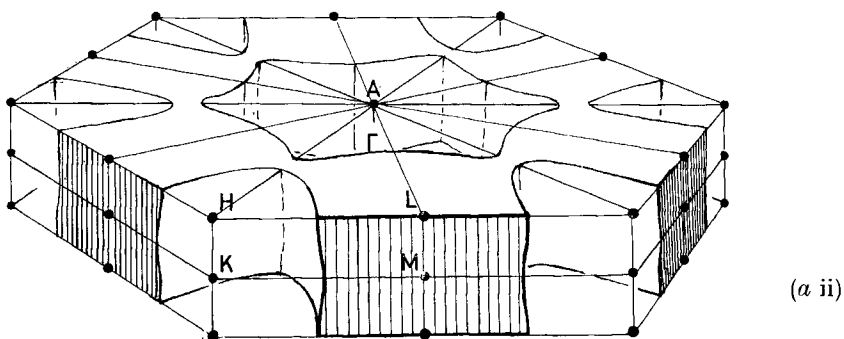
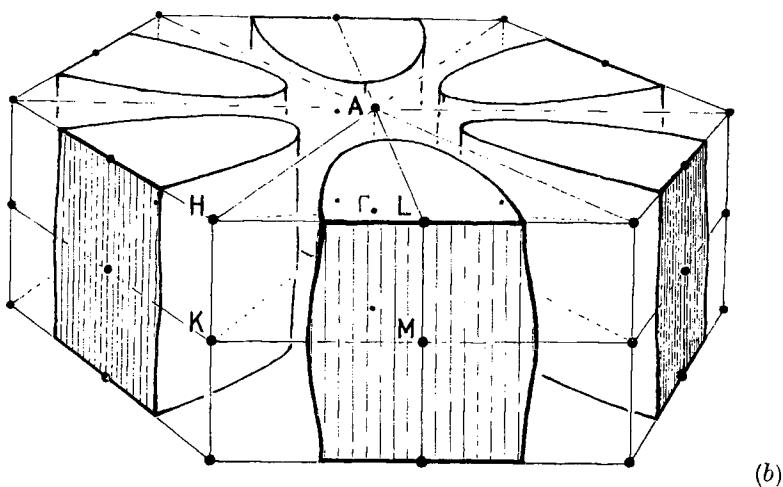
narrow ($\sim 1\frac{1}{4}$ eV), and the inter-sandwich band splittings (which occur away from the basal planes $k_z = \pm \pi/c$) in fact reach a comparable magnitude. Accordingly there is a marked effect on the form of the 2H Fermi surface and, along with it, on those properties of present interest for the d¹ 2H polymorphs.

Figure 26 (a), (b) gives Mattheiss' band structures for 2H- and 1T-TaS₂. In each the Fermi energy falls very close to 2 eV above the top of the p-band. Experimentally a p-d-band separation lower by $\frac{1}{2}$ eV would be preferred (Wilson 1975), but this is not of importance here. Far more important is the high sensitivity of the Fermi surface to small adjustments in band shape, particularly within the 'd_{z²}' band of the 2H polytypes, since it is so narrow. Although slight modifications are called for from various experimental results, for the moment we show the geometry of the Fermi surfaces as estimated from the calculations (fig. 27 (a), (b)).

Partly because there is only one molecule per unit cell for the 1T polytype, the Fermi surface is there particularly striking in its simplicity. All the electrons lie within one zone grouped around the six ML axes†. Adding to the simplicity is the very slight energy dependence in the k_z direction for the states about the ML axes, (a feature true for either polytype), this leading to a Fermi surface that is almost two-dimensional. For the 2H polytype this 2D character is not quite so marked, particularly close in to Γ , but experimentally one still finds an anisotropy of 30 in the bulk resistivity ($\rho_{\parallel c/p \perp c}$) (Edwards and Frindt 1971, Frindt *et al.* 1972). One should contrast the above c -axis d-bands with the very much wider bands found for NiS, the NiAs structure of which

† Angular photoemission results demonstrate that these regions are not all strictly equivalent away from the symmetry planes (Traum *et al.*, 1974), in accord with D_{3d}^5 symmetry.

Fig. 27

2H-TaS₂ lower band2H-TaS₂ upper band1T-TaS₂

(a) Fermi surface of 2H-TaS₂ (see also fig. 37), (b) Fermi surface of 1T-TaS₂, constructed from band-structure calculations of Mattheiss (1974), and hence not including splitting due to spin-orbit coupling. (The 2H surface represents an average of the APW and tight-binding results.)

amounts to a layered structure in which the previously empty inter-sandwich sites are now occupied by metal atoms (Mattheiss 1974). Helping to bring simplicity to the Fermi surfaces of the group V dichalcogenides is the fact that we are dealing with d^1 systems, where the Fermi level is first entering the d-band complex. Moreover, unlike the case with the transition metal elements or their alloys, the d-bands of the present sulphides are not overlapped by the metal s-band; neither are they directly overlapped by the ligand p-bands.

The total width of the d-bands is not inappreciable (~ 5 eV), this coming in large measure from covalent interband mixing. However, the bands are still sufficiently narrow in these chalcogenides that correlation effects, so important in oxide metals like V_2O_3 or CrO_2 , will still play a significant role. (For an assessment of the extent of correlation in the present materials relative to other transition metal compounds, see Wilson 1972, 1973.) Accordingly one expects and finds strong electron-phonon coupling along with superconductivity in many of the 4d/5d layered dichalcogenides, and magnetic behaviour in certain related 3d systems.

As will shortly be made evident, it is the union of these three features, (a) the general simplicity of Fermi surface, (b) the latter's strongly 2D characteristics, and (c) a strong electron-phonon coupling, that yields the effects of present interest.

§ 4. FERMI SURFACE DETERMINED PERIODICITIES AND SUPERLATTICES

A number of experimental and theoretical works have dealt with the relation of superlattice formation to the Fermi surface in metallic systems. Most of these concern order-disorder phenomena in certain alloys. There, a periodic potential deriving from the Fermi surface can cause a periodic sorting of the atoms away from the disordered condition. Far fewer papers as yet deal with the periodic displacements of *like* atoms, due to this same Fermi-surface-derived potential. Recent work (Comes *et al.* 1973, Werner 1974) on the Krogman salt $K_2Pt(CN)_4Br_{0.30} \cdot 3H_2O$, a quasi-one-dimensional metal, shows it to provide an excellent example of such periodic distortions. Other metallic systems that may incorporate similar effects include some rutiles like NbO_2 (Shapiro *et al.* 1974). We have found that the layered transition metal dichalcogenides are particularly amenable systems in which to study these periodic distortions, as the electron concentration can readily be changed by doping (see § 2.2 (f) and (g)). Moreover, various polytypes of the same compound, having quite different band structures, can easily be prepared. Several other reasons will become apparent shortly.

At the end of this section we give some background work on alloys, in so far as the results complement those now obtained with periodic structural distortions. We begin by discussing the conditions necessary for Fermi-surface-driven periodic structural distortions, and the applicability to the group V layered dichalcogenides.

4.1. *Pure materials; charge and spin-density wave states*

Electronic instabilities, which result in spin-density waves (SDW), or in the periodic structural displacements (PSD) coupled to charge-density waves (CDW), or in (long period) superlattice formation from atom sorting in alloys,

each arise from the same basic driving force; namely, a divergence in the generalized static electronic susceptibility $\chi(\mathbf{q})$. SDW and CDW possibilities of this sort in metals were both first considered seriously by Overhauser. In 1960 he examined the occurrence in Hartree–Fock theory of an instability with respect to the formation of an SDW and suggested that specific heat anomalies in certain dilute magnetic alloys might arise from a distribution of local fields caused by the stabilization of an SDW. (In most such systems effects of this type are now ascribed to a simple type of RKKY interaction, but SDW effects probably occur in some special systems such as Y–Gd.) Overhauser (1968) later considered the role of correlation, and suggested that its inclusion enhanced the possibility of CDW occurrence in simple metals: although CDW produced anomalies in the optical properties of alkali metals are not now generally believed to exist. The developments of the SDW concept are discussed by Herring (1966).

$\chi(\mathbf{q})$ is derived from the ‘bare’ magnetic or electronic susceptibility of the conduction band, $\chi^0(\mathbf{q})$. The latter is proportional to a sum over the Brillouin zone of the form

$$\sum_{\mathbf{k}} \frac{n_{\mathbf{k}}(1 - n_{\mathbf{k}+\mathbf{q}})}{E_{\mathbf{k}} - E_{\mathbf{k}+\mathbf{q}}}$$

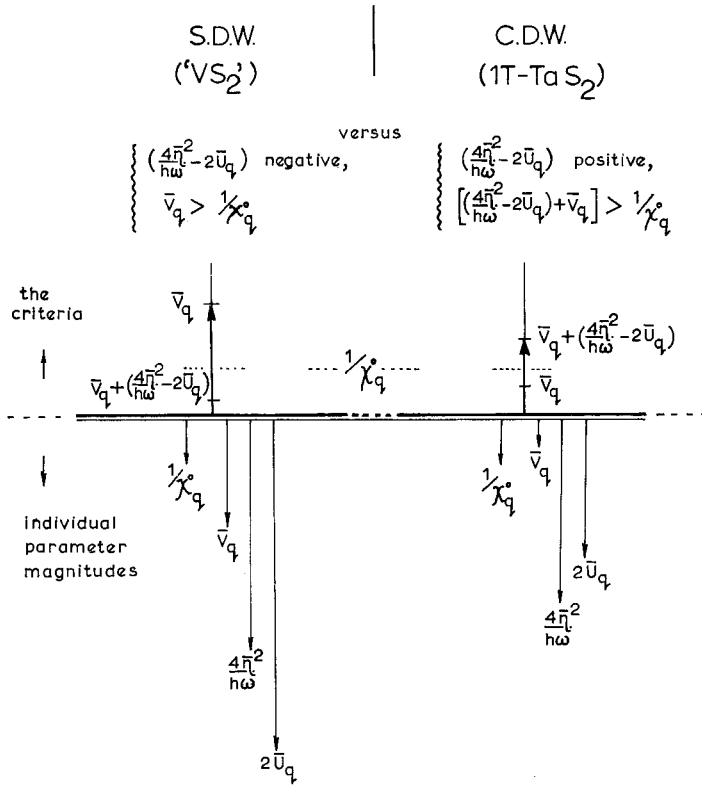
where $n_{\mathbf{k}}$ is the occupation number of the state \mathbf{k} as given by Fermi–Dirac statistics, and $E_{\mathbf{k}}$ is its energy. $\chi^0(\mathbf{q})$ depends critically on the geometry of the Fermi surface, since the latter determines the regions in k -space contributing to the above sum. Because of the form of the denominator, certain contributions to the sum $\chi^0(\mathbf{q})$ can attain a large value when \mathbf{q} is close to spanning the Fermi surface from side to side.

For free electrons at $T = 0$, the spherical Fermi surface leads to a $\chi^0(\mathbf{q})$ that decreases monotonically with increasing $|\mathbf{q}|$. If the Fermi surface possessed cylindrical sections, these would make a contribution to $\chi^0(\mathbf{q})$ that is independent of $|\mathbf{q}|$ up to $2k_{\text{F}}$, but which then falls as $|\mathbf{q}|$ increases further. If the Fermi surface contains flat parallel sections (or equivalently E versus k is one-dimensional), a contribution is made to $\chi^0(\mathbf{q})$ that diverges logarithmically at $|\mathbf{q}| = 2k_{\text{F}}$ (for these examples see Roth *et al.* 1966). The trend in χ suggested above has been affirmed for a complete but simply modelled Fermi surface by Fehlner and Loly (1974). They show $\chi^0(q)$ to steadily develop a peak very near $|\mathbf{q}| = 2k_{\text{F}}$, as the modelling radius of curvature for their Fermi surface is increased.

In an actual material the generalized susceptibility is obtained from the bare susceptibility by including electron–electron (direct Coulomb, exchange and correlation) and electron–phonon interactions. In calculations this is usually attempted via a renormalization of the RPA form $\chi(\mathbf{q}) = \chi^0(\mathbf{q})/[1 - X(\mathbf{q})\chi^0(\mathbf{q})]$. $X(\mathbf{q})$ is rather weakly dependent upon the detailed Fermi surface shape, but, as will be apparent later, it can be influenced by the symmetry of the Fermi surface. A divergence in $\chi(\mathbf{q})$ will occur if and as $X(\mathbf{q})$ tends to $1/\chi^0(q)$. Since $\chi^0(\mathbf{q})$ is always greater than zero, $X(\mathbf{q})$ must be positive if any divergence is to be at all possible.

Chan and Heine (1973) give the explicit form of $X(\mathbf{q})$ for several different circumstances. They show that when $X(\mathbf{q})$ is dominated by the screened exchange matrix element $V(\mathbf{q})$, a SDW instability may occur, as in the case of

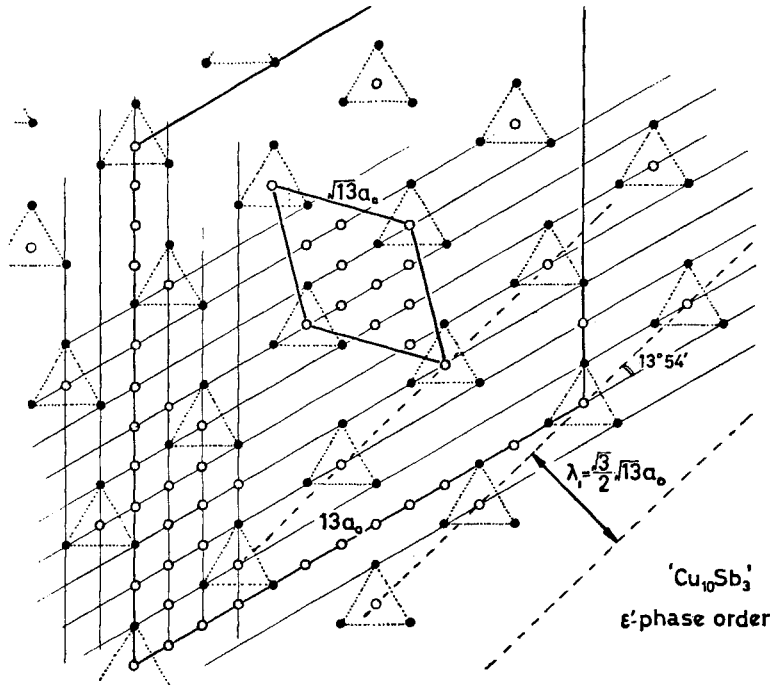
Fig. 28



A schematic of the SDW/CDW choice, displaying the criteria as developed by Chan and Heine (1973), and the likely modifications in the various parameters in going from a 5d to a 3d material. \bar{V}_q and \bar{U}_q are the averaged screened exchange and bare Coulomb matrix elements respectively (for the conduction electrons), and $\bar{\eta}$ is a measure of the electron-phonon coupling. $\omega(q_0)$ is the unmodified phonon frequency at the singularity wave-vector.

Cr metal. When the electron-phonon interactions become important and overwhelm the electrostatic term U_q , the alternative conditions for a CDW to arise are deduced (see fig. 28). This work suggests that an instability will result only when $\chi^0(q)$ is itself large. Overhauser, on the other hand, in his 1968 paper maintains that electron correlation, when allowing properly for the system response, could allow $X(q)$ of itself to produce particularly a CDW as ground state. His discussion was largely given in connection with potassium metal, where $\chi^0(\mathbf{q})$ is essentially of course free-electron-like. However, many theorists express the feeling that if $X(\mathbf{q})$ were indeed large enough to produce a CDW in a virtually free-electron gas, more severe instabilities such as complete localization of the conduction electrons would in fact form a lower energy state in a large number of materials. Despite such questions, we use the above form of $\chi(\mathbf{q})$ as the basis of discussion, while acknowledging questions as to its capacity to foretell every CDW instability. We note there is no general reluctance to accept the possibility of a CDW, whenever $\chi^0(\mathbf{q})$ is large enough, as seems to be the case for the quasi-one-dimensional metallic compounds

Fig. 29



A basal-plane atom-sheet of the ordered h.c.p. alloy 'Cu₁₀Sb₃' (the ε'-phase), showing the rotated $\sqrt{13}a_0$ supercell. The distribution of the antimony (filled circles) comes close to matching three symmetrically directed sinusoidal waves, with $\lambda_1 = \sqrt{3}/2 \cdot \sqrt{13}a_0$. Down an atom row the repeat is $13a_0$. (Based on the work of Yamaguchi and Hirabayashi 1972.)

K₂Pt(CN)₄ · 0.3Br · 3H₂O, etc. (Rietschel 1973, Rice and Strässler 1973), and perhaps even for the TTF-TCNQ-like organic salts. While $\chi^0(\mathbf{q})$ for the layered compounds under study is not even roughly calculated as yet, the Fermi surfaces indicated by the present band-structure calculations, with their strongly two-dimensional character, do lead one to expect large peaks in $\chi^0(\mathbf{q})$. Thus, while this particular paper will not resolve some of the basic theoretical differences concerning CDW formation, it serves to show that CDW's exist in other than one-dimensional compounds.

Actual calculation of a q -dependent susceptibility has been made for very few metals. A recent calculation (Cooke *et al.* 1974) of $\chi(q, \omega)$ for niobium $\langle 100 \rangle$ evaluates the size of anomaly in χ , from which the much investigated Kohn phonon anomalies (see Sharp 1969) are produced. The effect of temperature on χ and χ^0 is most pronounced in one dimension (or for flat sections of Fermi surface), where the peak at $2k_F$ becomes proportional to $\ln(E_F/kT)$, (Ehrenfreund *et al.* 1972). A circumstance similar to that of one dimension arises for multi-sheeted Fermi surfaces, when for instance a hole sheet can be closely nested into an electron sheet by vector \mathbf{q}_0 , as for antiferromagnetic Cr. (For recent discussion, and band structure of the paramagnetic phase, see Rath and Calloway 1973). A calculation by Rice and Halperin (1970) of the effect of temperature on the non-divergent 5d analogue, tungsten, indicates that there

the peak present in $\chi^0(q)$ at $T=0^\circ\text{K}$ (peak height $\approx 2\chi^0(0)$), is decreased and broadened about 25% by 400°K .

Given the temperature dependence of the peaks in $\chi^0(\mathbf{q})$, and also that of the electron-phonon coupling, a divergence in $\chi(\mathbf{q})$ may be attained as the temperature is reduced from a suitably high value. From this model one may expect a second-order phase transition at such a divergence, that can leave a CDW ground-state with $q=q_0$ for $T < T_{o(\text{onset})}$. Below T_o the coupled periodic structural distortion (PSD) of wavelength $2\pi/q_0$ (in general incommensurate with the atomic lattice) grows in amplitude in an approximately BCS-like way (see Rice *et al.* 1969, for case of the chromium SDW). Above T_o , due to the appreciable electron-phonon coupling, softening of certain lattice modes is expected as with other second-order lattice instabilities. In 2H-TaSe₂ such softening is apparent, from the diffuse scattering seen in electron diffraction, over a span of some 50°K prior to the (seemingly) second-order transformation at 120°K . The diffuse scattering in this case appears around those same reciprocal lattice points as are shown ultimately for the CDW itself (see § 2.2 (*d*) and § 7). Such scattering may come both from the large vibrational displacements of a giant Kohn anomaly induced in the phonon dispersion curves, and the fluctuating development of SRO for the impending CDW state. Analogous critical scattering, pertinent to the postulated SDW state in $\gamma\text{-Mn}$, has been detected there above T_N (Moringa 1974).

4.2. Points concerning the behaviour of a CDW

Following upon the creation of a CDW(/SDW) state at T_o , whatever diffuse scattering then remains present could express a rather limited phase coherence length, together with some non-conformity in the selection of orientation of the CDW. Inevitably a limited phase coherence length could be caused even at $T=0$ by, for example, impurities and dislocations. Furthermore, as was expounded by Overhauser (1971), there probably exist low-lying excitations of the CDW corresponding to local changes of the CDW direction and wavelength, these arising from phase modulation effects of the phonons on the CDW/PSD. Such excitations Overhauser labelled 'phasons' in analogy with magnons. The coupled phason modes occur for wave-vectors fairly close to q_0 . Out of the $3N$ vibrational modes, they may contribute (as derived by Overhauser) very disproportionately to the Debye-Waller factor for the PSD, though not to that for the parent structure. We shall return to this topic when discussing the characteristic diffuse scattering observed in 1T/4Hb-TaS₂/Se₂ in the extensive temperature range between T_d and T_o . [Note that this latter temperature is here normally inaccessible because of inter-polytypic conversion, but may be reached through Ti doping (see § 6).]

As will be expanded upon in §§ 5 and 6, all the various experimental results do indicate, in the case of the 1T and 4Hb polytypes, that there exist incommensurate charge-density waves, the amplitude of which grows down through the polytypic stability range below 550°K as far as T_d . For these polytypes the first-order transition at T_d represents the point of conversion ('lock-in') to a commensurate geometry. The superlattice so defined then permits a reduced zone description for both the electron and phonon dispersion curves. In the contrasting case of the 2H polytypes, the CDW appears at onset very

closely associated with a $3a_0$ commensurateness (see § 7). Because of the rather strong electrostatic forces involved in CDW generation, it might be supposed that the drive to become commensurate should be stronger for a CDW than for an SDW. Somewhat surprisingly most impurities in chromium quickly drive the system towards commensurate behaviour (for details and theory see Edwards and Fritz 1973, Kotani 1974), whereas all impurities seem for our CDW's to have the effect of depressing the lock-in temperature (see § 6). Especially for a CDW involving tight-binding d-electrons, we suspect that the move to adopt some appropriate lattice commensurate geometry will occur whenever a reasonable chance appears. Since an incommensurate wave will inevitably in some places situate its charge maxima between metal atoms, the move to become commensurate will secure that the displaced charge be centred back on the metal atom ions. Certainly this is how what occurs with the present 1T and 4Hb materials at T_d is most readily interpreted (see § 5.2).

When a CDW becomes commensurate at such a first-order transition, it may change magnitude, wavelength and/or direction. The enthalpy of this transition, ΔH_d , is a measure of the net commensurability energy. If ΔH_d were to be rather large compared with the integrated excess heat capacity of the incommensurate CDW ($\Delta H_i = \int \Delta C_p \cdot dT$, relative to the simple ground state), the structural adjustment is probably not just a response to the Fermi surface geometry. In such a case, particularly when an *incommensurate* CDW is not maintained above the lattice distortion temperature, the transition can more fruitfully be discussed in other terms. We suggest then that the term CDW be reserved to two circumstances: (1) to the incommensurate state where wavelength and direction are determined solely by a divergence in $\chi(\mathbf{q})$ at \mathbf{q}_0 , a spanning vector of the Fermi surface, (2) subsequent to the adoption of a commensurate state at some first-order transition temperature (in general from an incommensurate state), for which transition $\Delta H_d \lesssim \Delta H_i$. The exact boundary in this second case is somewhat arbitrary, but we intend to separate a CDW from cases where $\Delta H_d \gg \Delta H_i$, particularly when $\Delta H_i \rightarrow 0$, because in these latter cases the Fermi surface is of little or no importance. Such is, for instance, probably the case for the MnP-type distortion of the NiAs structure, (0.3 Å displacements at 300°K), found in d²TiSe and d³VS. The same is true for the distorted rutile family VO₂, NbO₂, etc.

In the d¹ metallic layer compounds we have encountered a case where the Fermi surface is particularly simple, and shows large approximately plane-parallel regions. Because of the simplicity of the Fermi surface, the associated oscillatory potential impressed on direct space (the transform of $\chi^0(\mathbf{q})$, Roth *et al.* 1966) is free from many strongly conflicting components. Furthermore, because of the large parallel elements it is strong and long-range. For plane-parallel sections of the Fermi surface, Roth and co-workers have shown that the derived real space component of potential falls off only as $1/r$, in contrast to $1/r^3$ for spherical Fermi surface segments. Further, the strength of the component is proportional to the areas of the Fermi surface lying parallel. Note the oscillatory potential is impressed upon real space parallel to the k -vector that spans the Fermi surface segments of interest.

One further important point for these d¹ layer metals, noted in general materials systematics (Wilson 1972, 1973), is that exchange and correlation effects do remain at a quite significant level ($U \approx \frac{1}{2}\Delta$); indeed, there is some

magnetic behaviour in related 3d systems (e.g. see Conroy and Pisaharody 1972). The trigonal prismatic polytypes are superconductors, for which, above T_c , ρ increases approximately as $a \times T^2$, an indicator of the strong electron–electron scattering, to which highly correlated metallic transition metal compounds are susceptible (Volkenstein *et al.* 1973, Doniach 1974). For 2H–NbSe₂ the fairly narrow band-width and the quite high electron–electron and electron–phonon interactions lead to $a_\rho \simeq 5 \times 10^{-9} \Omega \text{ cm } (^{\circ}\text{K})^{-2}$, $\gamma_{cv} \simeq 20 \text{ mJ/mole } ^{\circ}\text{K}^2$, and $V_{\text{ph}}^{\text{BCS}} \sim 0.4 \text{ eV}$ (van Maaren 1972), values that are fairly typical of transition metal superconducting compounds toward the narrow band limit. The materials fall then within the rather narrow range of interaction strengths that seem suited, in the presence of a sympathetic band structure, to support instabilities towards charge and spin-density wave ground states. The choice criteria, developed by Chan and Heine (1973), for the adoption of a CDW versus a SDW, are shown figuratively in fig. 28. We portray there some plausible relative changes in magnitude of the various parameters, such as are required for the promotion of a CDW for 5d¹TaS₂, but a SDW for related vanadium containing 3d materials. In fig. 28, of the various parameters, \bar{V}_q and \bar{U}_q are the average (local) exchange and Coulomb matrix elements, and η is a measure of the electron–phonon coupling.

The equilibrium amplitudes that might be reached in such oscillatory adjustments to the ground state have not been treated, but from experiment would seem to range widely, e.g. for SDW's proved or postulated, see CrB₂ (Liu *et al.* 1973), γ -MnFe (Endoh *et al.* 1973), Cr (Rice *et al.* 1969), and α -U (Smith and Fisher 1973). As regards a CDW, it remains to be proved that a rutile like NbO₂, with its 0.25 Å displacements (see Shapiro *et al.* 1974, or Nb₃Sn (0.015 Å, Shirane and Axe 1971) are genuine members of the class (as some suggest). The only clearly signatored case of a CDW, apart from the materials we are currently discussing, is for the previously mentioned linear-chain partially oxidized platinum cyanide family, e.g. K₂Pt(CN)₄Br_{0.30} · nH₂O. The properties of the latter, however, do present some interpretative problems because of the non-stoichiometric disorder (Butler and Guggenheim 1974). Recent diffuse-scattering experiments (Comes *et al.* 1973 a, b) suggest a displacement modulation within the Pt chains of approximately 0.05 Å. The modulation here is indeed seen to derive from coupling to the Fermi surface, since making the change from the K/Br_{0.30} to the Rb/Cl_{0.23} compound changes the observed wavelength in the appropriate manner. For both these materials, moreover, the modulations are lattice incommensurate, at least at room temperature. Our present results show that the system 1T–(Ta/Ti)S₂ is particularly flexible on this latter point, as is set out in detail in § 6. It is hoped that current neutron diffraction work on the layer metals (Moncton and Axe 1974) will, in addition to yielding crystallographic data on the distortions, be able to follow in detail the soft-mode behaviour (in Γ M) occasioned by the CDW, as has been done for the Pt-chain compounds (Renker *et al.* 1973, Werner 1975). It should provide also more experimental data against which to test the self-consistent electron–phonon interaction theory recently developed by Barišić *et al.* (1972, 1973), primarily with the A15 superconductors in mind.

4.3. Alloys ; Fermi surface driven long and short-range order

Certain alloy systems can show ordered superlattices of strikingly long repeat period, e.g. $10a_0$ for CuAu(II) (Tachiki and Teramoto 1966). Such work (see

Sato and Toth 1968) often has linked the driving force of this atomic organization to the generation, via the appropriate superlattice, of new Brillouin zone boundaries more or less coincident with the old Fermi surface of the disordered ('parent') structure, over considerable areas in k -space. This must secure a reduction in the total electronic energy. In extreme cases the superlattice can bring a significant reduction in the number of free carriers.

A recent study of this type (Yamaguchi and Hirabayashi 1972) has dealt with the order in certain h.c.p. Cu-Sb alloys containing close to 20% Sb. These workers relate their electron diffraction results to two idealized superlattice formulae $\text{Cu}_{78}\text{Sb}_{20}$ (ϵ -phase, 20.4% Sb) and $\text{Cu}_{10}\text{Sb}_3$ (ϵ' -phase, 23.1% Sb). Actually in the former phase ($98 = 7 \times 7 \times 2$ atoms) certain sites in the superlattice (12 in number) are randomly occupied by either Cu or Sb, and then, for specimens slightly antimony-poor, the periodicity taken up in the ϵ -phase is observed to be variable and fractionally greater than $7a_0$. This incommensurate periodicity falls towards 7 as the electron-to-atom ratio is increased (via increase in the antimony content). No such latitude was observed for the ϵ' -phase. The structure determined for this latter phase is shown in fig. 29. In this superlattice the antimony atoms are seen to cluster around the corners of a $\sqrt{13}a_0$ cell having '3-by-1' ($13^\circ 54'$) rotation in the basic h.c.p. array. We have already encountered a cell of this external form for 1T-TaSe₂.

The segregation of atoms in these alloys to produce matter waves as apparent as those in fig. 29 is also a feature found in certain non-stoichiometric materials that maintain very high vacancy concentrations, e.g. in the carbide vacancy materials like V_nC_{n-1} (Billingham *et al.* 1972, Shacklette and Williams 1973), and also in various superlattice materials based on 'TiO' for which both sublattices can be highly defective (Castles *et al.* 1971). When all such materials are maintained through quenching in the 'parent' disordered condition, and subsequently are examined in diffraction, particularly electron diffraction, they are found to show very marked narrow bands of diffuse scattering. The magnitude of the vectors of strongest diffuse scattering correlate closely with the size of the superlattice finally attained in the ordered phase. These same vectors of strong diffuse scattering themselves would seem to be determined by the Fermi surface geometry of the parent condition (i.e. when fully disordered).

The cut-off effect of any particular Fermi surface on some wave-vector-dependent property, such as the generalized susceptibility $\chi(\mathbf{q})$ above, or here the 'pair-ordering function' figures prominently when Fourier-transformed back in the real-space potential. The range of the ensuing periodic real-space potential component has been confirmed in Cu_3Au and related alloys to be active to beyond third nearest neighbours (Moss 1969, Cowley and Wilkins 1970). The geometry of the potential so impressed upon a particular alloy will in general be incommensurate with the parent lattice, and any ultimate adoption of some commensurate LRO (as that given above for the Cu-Sb ϵ' -phase), usually represents a delicate choice, balancing electronic and lattice energies. Whatever order geometry might be assumed within the alloy is simultaneously dependent on the Fermi surface, as dictated by the Fermi level (or initially ' e/a '), and, of course, on the numerical ratio between the atom types there present.

Such diffuse scattering as is observed could in alloys in principle arise from

three possible mechanisms : (a) static short-range order (SRO), i.e. the vacancies or alloy atoms do not show complete randomness, (b) soft phonon modes producing strong thermal scattering, (c) local dynamic fluctuations into a LRO condition whose lifetime may be as long as 10^{-6} sec. The last possibility is prompted by observation of just such an effect for the omega phase of Zr/Nb, via neutron and Mössbauer studies (Moss *et al.* 1973, Batterman *et al.* 1973). Of course, several of these effects may be present in any specific case. All of them, potentially, can arise from the same basic electronic instability.

For alloys and defect materials it has in a few cases been possible to convert the observed diffuse-scattering map, which can be very complex, back into the real-space SRO distribution function (e.g. V_6C_5 , Sauvage and Parthé 1972). The other task posed of tracing the observed diffuse scattering vectors back to the Fermi surface topology has proved more difficult. Agreement seems to have been attained for Cu_3Au (Moss 1969, Hashimoto and Ogawa 1970), and some tentative suggestions have been made for 'TiO' (Castles *et al.* 1971). However, in most cases the Fermi surface is simply not determined as yet to the accuracy required.

§ 5. DETAILED INTERPRETATION OF THE EXPERIMENTAL OBSERVATIONS IN POLYTYPES CONTAINING OCTAHEDRAL SANDWICHES

In this section the diffraction results presented in § 2 are derived from a simple model of scattering for a PSD, and the observations are connected in detail to the basic physics as presented in § 3 and § 4.

5.1. Analysis of the diffraction results for the incommensurate state

Since the 1T polymorphs have three-fold rotational symmetry about the c axis, it may be anticipated that three equivalent charge-density waves with propagation directions at 120° to one another will co-exist (though such is not always the case ; cf. the SDW in Cr, where a single cubic axis (per domain) is selected). Also, since the inter-sandwich bonding is weak, and as there is a large anisotropy in resistivity (> 10), it might further have been suspected that the charge-density waves are not coupled in phase from sandwich to sandwich. Below we shall demonstrate that there are indeed three CDW's per layer, and that, in fact, the combined phase does systematically shift from one sandwich to the next.

If a CDW in the conduction band causes a sinusoidally varying component in the electron density, one expects the ionic cores and the nuclei to readjust their position in a sinusoidal response to the electric field of the wave (Overhauser 1968, 1971). The atomic displacements from equilibrium are presumed to be proportional to the local gradient in the CDW, $\Delta \mathbf{x} \propto \nabla(\Delta \rho)$. The displacement wave will take the form $\Delta \mathbf{x} = \mathbf{A} \sin(\mathbf{q}_0 \cdot \mathbf{r} + \Phi)$, where \mathbf{q}_0 is the propagation wave vector, \mathbf{A} is the wave amplitude, and is parallel to \mathbf{q}_0 , \mathbf{r} labels the unperturbed atomic positions, and Φ is an arbitrary phase angle not tied to the atomic lattice.

If we neglect the smooth variation of the atomic scattering amplitude with scattering angle, the amplitude of scattering from such a modulated crystal,

$I(\mathbf{k})$ (either X-ray or electron diffraction, neglecting extinction and double diffraction effects) takes the form

$$I(\mathbf{k}) \propto \sum_{\substack{\text{atomic} \\ \text{positions}}} \exp \{i\mathbf{k} \cdot [\mathbf{r} + \mathbf{A} \sin(\mathbf{q}_0 \cdot \mathbf{r} + \Phi)]\}. \quad (1)$$

To compute this sum the following identity is used, after Overhauser (1971):

$$\exp(iY \sin \theta) = \sum_{\alpha=-\infty}^{+\infty} J_{\alpha}(Y) \cdot \exp(i\alpha\theta),$$

where $J_{\alpha}(Y)$ is a Bessel function of order α . If we then assume the crystals are large, so that broadening of the diffraction spots due to crystal size may be ignored, the following $I(\mathbf{k})$ is obtained (one atom per unit cell):

$$I(\mathbf{k}) \propto \sum_{\alpha} \exp(i\alpha\Phi) J_{\alpha}(\mathbf{k} \cdot \mathbf{A}) \cdot \delta(\mathbf{k} - h\mathbf{a}_0^* - k\mathbf{b}_0^* - l\mathbf{c}_0^* - \alpha\mathbf{q}_0), \quad (2)$$

where the Dirac delta function contains h, k, l, α —integers (positive or negative), $\mathbf{a}_0^*, \mathbf{b}_0^*, \mathbf{c}_0^*$ —the reciprocal lattice vectors of the *undistorted* cell (2π included in definition). (For the case of the layer compounds we shall use the standard symbols for a crystal with hexagonal axes, $\mathbf{a}_0 = \mathbf{a}_{10}$, $\mathbf{b}_0 = \mathbf{a}_{20}$, $\mathbf{c}_0 = \mathbf{c}_0$.)

We break the problem (worked here for the 1T polymorphs, $T > T_d$) into two parts; firstly, the scattering from a single 'layer', assuming three waves at 120° with various selected phase relationships; secondly, the mode of CDW stacking between successive 'layers'.

For a single layer we assume three waves of the type $\mathbf{A}_i \sin(\mathbf{q}_{oi}' \cdot \mathbf{r} + \Phi_i)$, $i = 1, 2, 3$, with the \mathbf{q}_{oi}' in the plane of the layer directed 120° apart. Since we are discussing a single layer $\mathbf{r} = n_1\mathbf{a}_{10} + n_2\mathbf{a}_{20}$, with n_1 and n_2 integers. Inserting three waves into eqn. (2), we find for the scattering amplitude from a single layer

$$I_L(\mathbf{k}) \propto \sum_{\alpha, \beta, \gamma} \exp[i(\alpha\Phi_1 + \beta\Phi_2 + \gamma\Phi_3)] \cdot J_{\alpha}(\mathbf{k} \cdot \mathbf{A}_1) \cdot J_{\beta}(\mathbf{k} \cdot \mathbf{A}_2) \cdot J_{\gamma}(\mathbf{k} \cdot \mathbf{A}_3) \\ \times \delta(\mathbf{k} - h\mathbf{a}_{10}^* - k\mathbf{a}_{20}^* - L\mathbf{c}_0^* - \alpha\mathbf{q}_{o1}' - \beta\mathbf{q}_{o2}' - \gamma\mathbf{q}_{o3}'), \quad (3)$$

where α, β, γ, h and k are integers, but L is a continuous variable. This scattering occurs on lines perpendicular to the layer. In addition to scattering as from the unmodulated structure, lines of scattering occur separated from the parent reciprocal lattice positions, $h\mathbf{a}_{10}^* + k\mathbf{a}_{20}^*$, by positive and negative integer multiples of q_{o1}' , q_{o2}' and q_{o3}' .

The scattering from the complete crystal is next obtained by adding the scattering from each layer, with due regard to relative phase in successive layers. We give computation of this scattering in a model which fits the data for 1T-TaS₂ and 1T-TaSe₂ when $T > T_d$. The model is as follows:

(1) The amplitudes $|\mathbf{A}_i|$ are the same in each layer, and also from layer to layer.

(2) In a given layer the three phases Φ_i take a common value Φ' at the arbitrarily placed CDW origin, there being a progressive shift of 120° made in each from one layer to the next. This latter factor may appear somewhat arbitrary, but is necessary to explain the results presented in § 2.2. As we will later illustrate, the condition reduces the Coulomb interaction energy of the

CDW's between successive sandwiches. Within this model we have, then, for the total scattering amplitude,

$$\begin{aligned}
 I(\mathbf{k}) \propto \sum_{n_3} \left[\exp [i\mathbf{k} \cdot \mathbf{c}_0(3n_3)] \cdot I_L(\mathbf{k}, \Phi^{(1)} = \Phi') \right. \\
 + \exp [i\mathbf{k} \cdot \mathbf{c}_0(3n_3 + 1)] \cdot I_L \left(\mathbf{k}, \Phi^{(2)} = \Phi' + \frac{2\pi}{3} \right) \\
 \left. + \exp [i\mathbf{k} \cdot \mathbf{c}_0(3n_3 + 2)] \cdot I_L \left(\mathbf{k}, \Phi^{(3)} = \Phi' + \frac{4\pi}{3} \right) \right]. \quad (4)
 \end{aligned}$$

Inserting the form of I_L (eqn. (3)), we can sum over n_3 to obtain the total scattering amplitude

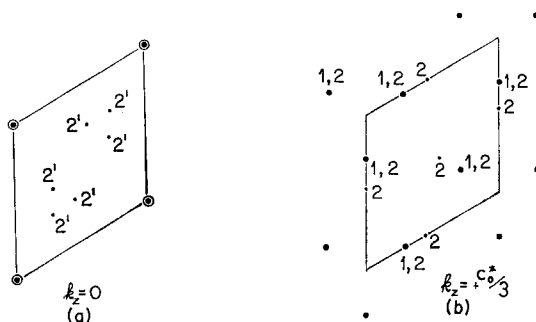
$$\begin{aligned}
 I(\mathbf{k}) \propto \sum_{\alpha, \beta, \gamma} \left(1 + \exp \left[\frac{2\pi i}{3} (\alpha + \beta + \gamma + l) \right] \right. \\
 \left. + \exp \left[\frac{4\pi i}{3} (\alpha + \beta + \gamma + l) \right] \right) \cdot J_\alpha(\mathbf{k} \cdot \mathbf{A}_1) \cdot J_\beta(\mathbf{k} \cdot \mathbf{A}_2) \cdot J_\gamma(\mathbf{k} \cdot \mathbf{A}_3) \\
 \times \delta \left(\mathbf{k} - h\mathbf{a}_{10}^* - k\mathbf{a}_{20}^* - \frac{l}{3} \mathbf{c}_0^* - \alpha\mathbf{q}_{01}' - \beta\mathbf{q}_{02}' - \gamma\mathbf{q}_{03}' \right), \quad (5)
 \end{aligned}$$

where now $\alpha, \beta, \gamma, h, k, l$ are all integers. From eqn. (5) it is immediately apparent that zero in intensity is obtained whenever $\alpha + \beta + \gamma + l \neq 3n$ (n -integer). Note that in the delta function l is divided by 3, and this is equivalent to fixing of the c -axis repeat as $3c_0$, via the above 120° shifts in Φ' .

In order to compare eqn. (5) to the observed scattered intensity, one should note that the magnitude of the \mathbf{A}_i 's is fairly small ($\sim 0.1 \text{ \AA}$ or less), so that, for the scattering range studied, $\mathbf{k} \cdot \mathbf{A}_i \lesssim 0.3$. For this range we can replace J_α by its small argument expansion $J_\alpha(Y) = (2/\alpha!)^{-1} \cdot Y^\alpha$. Also, with α integral, $J_{-\alpha}(Y) = (-1)^\alpha \cdot J_\alpha(Y)$, so that the relative intensity of a given satellite spot to a main peak is approximately $(\mathbf{k} \cdot \mathbf{A})^{2(|\alpha|+|\beta|+|\gamma|)}$. Consequently we expect to see satellite spots only of low order, the order index being $(|\alpha| + |\beta| + |\gamma|)$. The numbers previously used to label the sharp spots in fig. 13 are just the above orders for the various types of reflection spot.

From the diffraction experiments for $T > T_d$, we identify, (for 1T-TaSe₂), $|\mathbf{q}_{01}'|$ as $0.285[(2/\sqrt{3}) \cdot (2\pi/a_0)]$, the directions of the \mathbf{q}_{0i}' being along the \mathbf{a}_0^* . Using the extinction condition above, the calculated diffraction patterns for the $l=0$ and $l=1$ planes are shown in fig. 30, portraying only those spots of order ≤ 2 . In the planes $l=3n$, where the main (i.e. order zero) spots lie, the pattern has hexagonal symmetry about those spots, while in planes $l=3n \pm 1$ there is only trigonal symmetry. The pattern at $l=3n-1$ is the same as at $l=3n+1$, but rotated about \mathbf{c}_0^* by 60° . The spots again are labelled with their (lower) order numbers, and we use the prime to denote spots on the $l=0$ layer. In the $l=1$ pattern the triangular groupings of the three strongest satellite spots (sum of reflections of orders 1 and 2) are centred directly above the main spots in $l=0$. It is thus clear that the observed basal plane electron-diffraction patterns are a superposition of the $k_z=0$ and $k_z = \pm c_0^*/3$ planes, due to spot elongation and dynamical scattering, as pointed out in § 2.2 (*h*). The observations reported there for various sample tilt angles agree exactly

Fig. 30



The calculated positions of the first and second-order satellite spots for the incommensurate lattice modulation (in a $3c_0$ model), agreeing with the experimental results for the 1T polymorphs above T_d . The spots are shown as they fall in the $k_z=0$ and $+c_0^*/3$ planes. Relative to the $+c_0^*/3$ satellite spotting, that in the $-c_0^*/3$ plane is rotated by 60° about the a_0^* cell corner (see fig. 25).

with the predictions of the present analysis for which we have employed $c = 3c_0$.

A number of physical observations can now be drawn from this result. The first is that the shifting of the PSD phase from layer to layer amounts to a tilting of the divergent wave-vector out of the layer. If we choose three waves with $\mathbf{q}_{oi} = \mathbf{q}_{oi}' + c_0^*/3$, we would reproduce the results of eqn. (5), at least as far as the position of the satellite spots. Only proper measurement of intensities will reveal the direction of the actual displacements \mathbf{A}_i , but it seems not unreasonable to expect that the metal atom motions will be mostly parallel to the layers, i.e. that the \mathbf{A}_i be parallel to the \mathbf{q}_{oi}' . However, as far as coupling to the phonons is concerned, the vectors \mathbf{q}_{oi} will be the important ones. From a plate like fig. 12 (ii) we evaluate that $|\mathbf{q}_0| \approx 0.70 \text{ \AA}^{-1}$, this wave-vector being tilted out of the layer plane by $\approx 30\frac{1}{4}^\circ$ (see fig. 25). It is the projection \mathbf{q}_0' of \mathbf{q}_0 on the basal plane that later appears in fig. 34, along of course with the mean projection of the Fermi surface. From fig. 27 (b) (of the 1T Fermi surface) we note that the direct 'nesting' process may actually be improved following the above tilt to the \mathbf{q}_{oi} , since it tends to accommodate for the c -axis wiggle in the Fermi surface 'walls'.

Further insight into the form of the CDW state comes when we look at the real space-charge redistribution that it represents. First consider just a single layer, with its combination of three simple charge-density waves, $\Delta\rho = \Delta\rho_0 \sum_i \sin(\mathbf{q}_{oi}' \cdot \mathbf{r} + \Phi_i)$. The detailed contouring, and the peak-to-peak swing (A_ρ), of the resultant charge distribution will depend upon the value of Φ . The two most symmetrical cases are generated when (with $\Phi_i = \Phi'$)

$$\Phi' = 30^\circ + n \cdot 60^\circ, \quad \text{for which } A_\rho = 9/2\Delta\rho_0, \quad \left(\begin{array}{l} \text{six-fold symmetric, but} \\ \text{asymmetric w.r.t. } + \text{ and } - \end{array} \right),$$

and

$$\Phi' = 60^\circ + n \cdot 60^\circ, \quad \text{for which } A_\rho = 3\sqrt{3}\Delta\rho_0, \quad \left(\begin{array}{l} \text{only three-fold symmetric} \\ \text{though symmetric w.r.t.} \\ + \text{ and } - \end{array} \right).$$

(Note that we use the point where the Φ_i take a common value Φ' to define the phase origin in the incommensurate CDW itself.) The actual value taken up by Φ' is seen to be physically significant, in that it will affect the direct intra- (and inter-) layer Coulomb interactions. It is these latter that largely limit the stability of a CDW state. The Φ' adopted should tend to minimize the Coulomb interaction energy within, of course, the bounds set by the driving force for CDW formation (and $\Delta\rho \neq 0$) in the first place.

In fig. 31 the single-layer charge-modulation function is shown for the cases $\Phi' = 90^\circ$ and $\Phi' = 120^\circ$. The three individual waves are indicated by the vectors λ' drawn from the origin. Note that the maxima in the resulting undulatory build-up of charge make a hexagonal pattern in which they fall along lines rotated 30° away from the input \mathbf{q}_{oi}' directions. Since the \mathbf{q}_{oi}' lie parallel (almost) to \mathbf{a}_{oi}^* , the maxima are therefore to be found parallel to the direct space cell axes, a_o , and hence to the lines of atoms (see Appendix). Furthermore, the real space wavelength between these charge peaks is seen to be $\lambda_\rho' = 2/\sqrt{3} \cdot 2\pi/|\mathbf{q}_o'|$, or $2/\sqrt{3}$ times longer than the wavelength of the individual plane waves. With the value of $|\mathbf{q}_o'|$ previously deduced, we find for 1T-TaSe₂ ($T > T_d$), $\lambda_\rho' = a_o/0.285$ or $3.50a_o$.

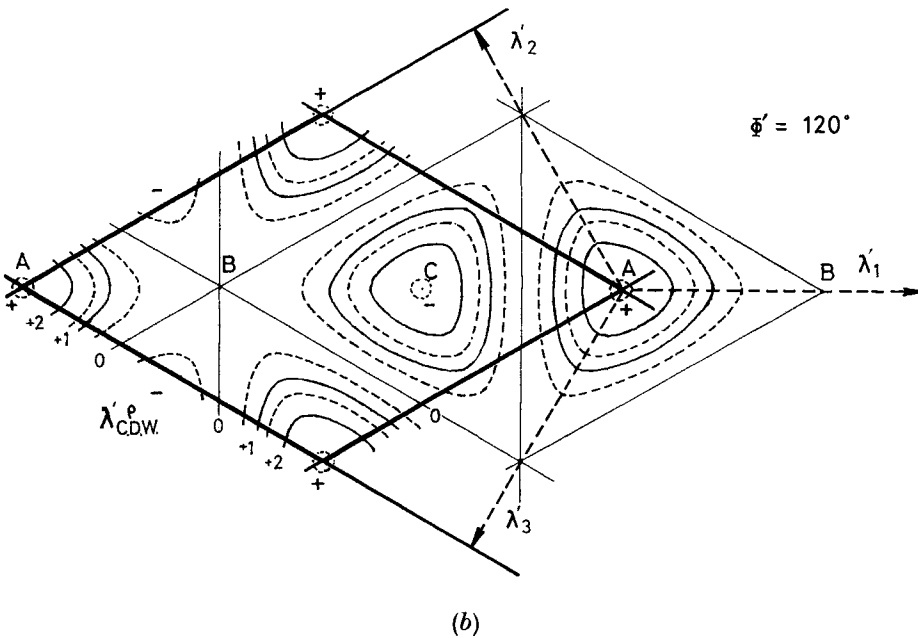
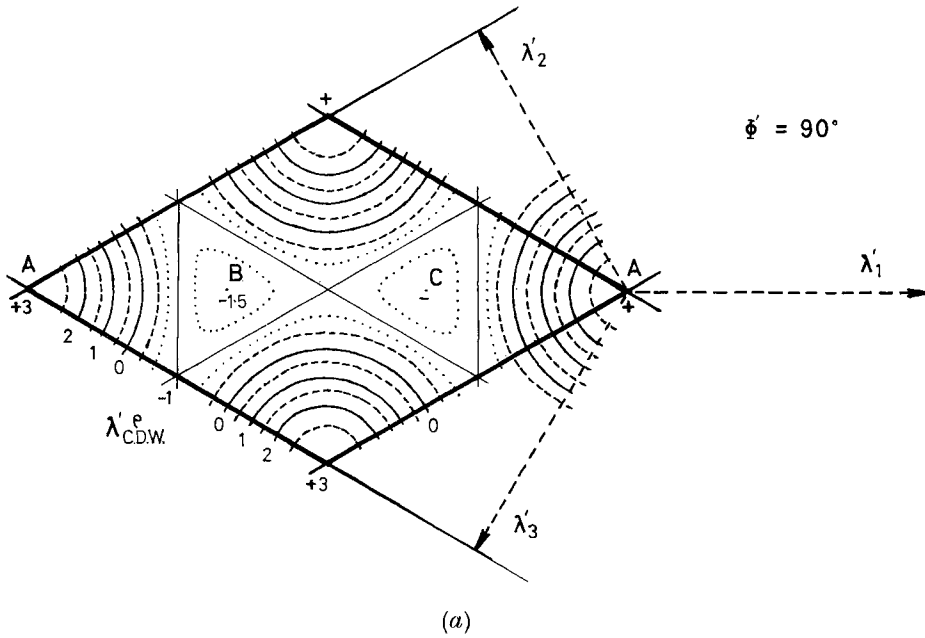
When generating the CDW in the next layer, we phase-shift each plane wave by 120° . The shape of the CDW remains identical to that in the previous layer, but it is translated in the 1120 direction so that charge maxima lie as far as possible above minima in the previous layer. Inspection of fig. 31 suggests the choice $\Phi' = 90^\circ$, with the CDW stacked ABCABC (using the usual close-packing notation) would best minimize the significant intra- and inter-layer Coulomb interaction†.

ABAB stacking of the CDW, while ruled out in the 1T case (since scattering would occur then at $l = n/2$ planes), would appear to represent the 4Hb case ($T > T_d$). The main CDW we take to occur in the alternate sandwiches, having octahedral coordination. The waves in these sandwiches then are directly superposed A-A-, as (crystallographically), are the metal atoms there (in fact for all the sandwiches, see fig. 1). The first-order satellites in the 4Hb plates never show a trigonal distribution of intensity (fig. 9), and flare at the same time as the zero-order spots (see § 5.2 (c)), thereby indicating that they lie in the same l -planes. The absence in the 4Hb (and 6R) plates of any second-order spotting could mean that the \mathbf{A}_i are smaller than in the 1T polymorph. It could also mean simply that the lateral coherence length of the modulation is relatively low (although the first-order spotting seems quite sharp). Coherence within each octahedral sandwich, it should be remembered, has in these polytypes to be maintained in the presence of flanking trigonal prismatic sandwiches.

When ABAB stacking of the charge-density wave is favoured by the symmetry of the parent crystallography, it seems likely from inspection of fig. 31 (a) and (b), that then the phase selection $\Phi' = 120^\circ$ could occur. Rather surprisingly ABAB stacking of the CDW does not appear to occur for the 2H materials (Moncton and Axe, to be published).

† Analogous phase staggering has also recently been reported between Pt chains in $\text{K}_2\text{Pt}(\text{CN})_4\text{Br}_{0.3}\cdot 3\text{H}_2\text{O}$ (Renker *et al.* 1974, Werner 1975).

Fig. 31

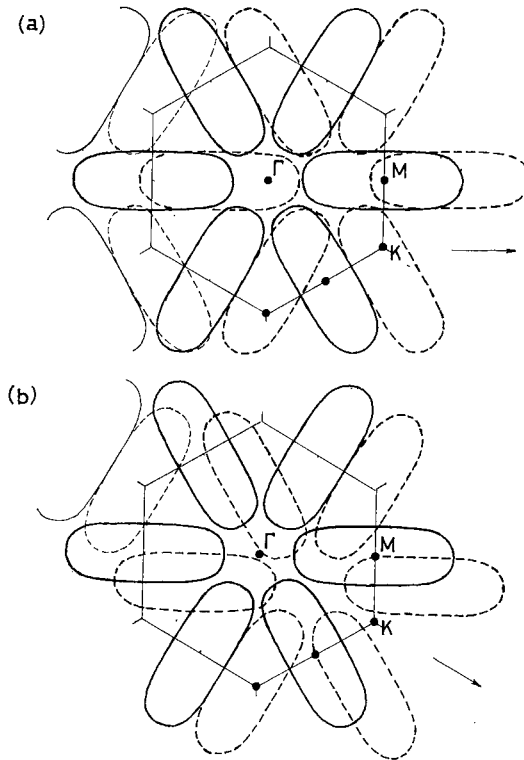


Charge modulation envelope produced by three sinusoidal waves directed at 120° to each other, for (a) $\Phi' = 90^\circ$, (b) $\Phi' = 120^\circ$ common phase angle at origin. Case (b) is symmetrical with respect to charge excess and deficit, though only trigonal; it also shows a larger overall amplitude. For more detail on geometry see Appendix diagrams. The origin in case (b) is brought to 'point' C by the choice $\Phi' = 240^\circ$.

The choice made by 1T-TaSe₂, etc. to employ the symmetry-related set of three vectors \mathbf{q}_{oi} , rather than just one of them, in order to define the CDW state, probably also devolves from the same question; namely, the best matching of the direct Coulomb interaction in the CDW to the crystallography of the undisturbed lattice. For a SDW, where the lattice response is much slighter, one does encounter single- q domains, as in Cr. With the exception possibly of NbTe₂/TaTe₂ (§ 7.5 (f)) no evidence of single- q domain behaviour has been detected for the present materials. Even for the phase below T'_d , the α and β domains mentioned earlier do not involve breaking the q set, but involve (primarily) rotation, positive or negative, of the triple set as a whole.

A final point concerning the high temperature phase plates is why the vectors \mathbf{q}_{oi} should be found to take orientations that, in basal plane projection, make angles of 30° with respect to the Brillouin zone side walls. In fact, in our previous short communication, we incorrectly depicted q_o' as being parallel to ΓK . It is apparent from the plates (for $T' > T'_d$), as from the above analysis, that ΓM is the operative direction. This point was correctly portrayed in the note of Williams *et al.* (1974). In fig. 32 we make comparison between the geometries leading to $\chi^0(q)$, firstly for the situation that holds empirically where q_o' is parallel to ΓM , and secondly for the case with q_o' parallel to ΓK (i.e. parallel to the zone walls). We do this by showing the Fermi surfaces as

Fig. 32



To demonstrate the superior overall 'nesting' of the 1T Fermi surface for the horizontal component of \mathbf{q}_{oi} parallel to ΓM , (a), rather than parallel to ΓK , (b).

displaced by the 'spanning' vectors for the directions in question. Although the second case probably gives the optimum contribution to $\chi^0(q)$ obtainable from a single segment of the Fermi surface, it is seen from fig. 32 (b) that the empiric case, with q_o' parallel to ΓM , secures quite comparable contributions per segment, but these now will arise for four out of the six Fermi surface segments, not just two. With the q_{oi}' parallel to ΓM , the charge maxima as built up in the triple CDW are, it should be recalled, rotated 30° away from the single component q -vectors, and thereby form in the atom row direction (see Appendix figure).

The size of the wave vector q_o , as deduced from the structure modulation satellites of the diffraction plates, requires that the Fermi surface be scaled as in fig. 32, given that its shape be kept as simple as possible. The Fermi surface is constrained then to intersect the zone wall approximately 0.43 of the way from ML to KH. The tight-binding interpolation scheme made by Mattheiss (from which fig. 27 (b) is constructed) yields approximately 0.59. In view of the fact that the calculation is a first principles' effort, and also that it carries a full $\alpha = 1$ correlation term, rather than some empirically more favourable value around 0.7, we regard this match as very satisfactory. In both figs. 32 and 27 we have met the condition that the Fermi surface encloses exactly one electron. With respect to the detailed shape, however, it should be recalled that the 1T space group is only trigonal not hexagonal, and away from the symmetry lines and planes of the band-structure calculation, the band structure and Fermi surface in alternate hexants of the zone need no longer be equivalent. In our figures we have assumed any such deviation to be slight†. Angular photo-emission results (Traum *et al.* 1974), on the other hand, indicate a very substantial trigonality, and we may be making some error at this point. However, the photo-emission work is complicated by questions both of steric emission and blocking for the electrons comprising the photo-emitted beam.

The main features to perceive for the high temperature 1T phase are : (1) the CDW in each sandwich is formed from a symmetrized set of three wave vectors ; (2) the wave vectors q_{oi} possess a k_z component, which relates to c -axis stacking of the CDW from one sandwich to the next ; (3) the basal component of the wave vectors takes the ΓM directions in order to maximize $\chi^0(q_o)$ from *all* segments of the Fermi surface simultaneously ; (4) the triple CDW, as built up in direct space, aligns its charge maxima within a sandwich along atom rows, with an incommensurate spacing of about $3.5a_o$. Because of cancellation between the pair of $2/\sqrt{3}$ factors, $\lambda_{CDW}^{triple} = (a_o^*/q_o')a_o$.

In the next subsection we shall see what is the relation between this geometry and that of the commensurate phase below T_a .

5.2. The commensurate CDW state

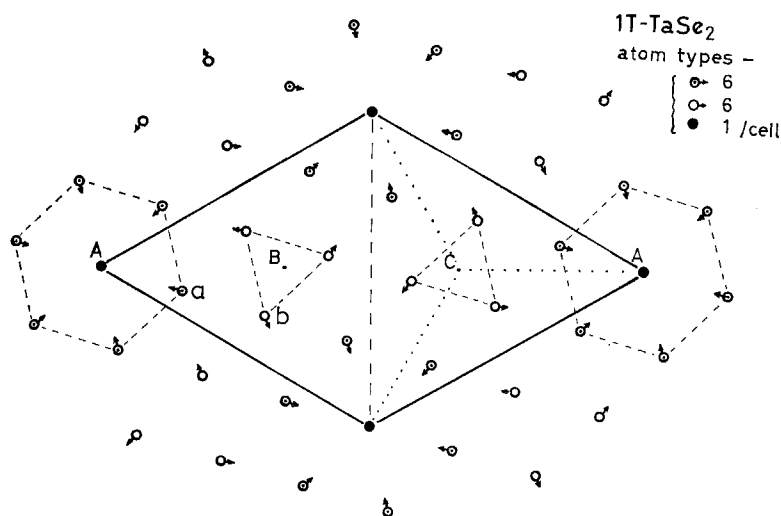
(a) General aspects for the 1T polymorphs

At T_a , it appears, taking the simplest case of 1T-TaSe₂, that the charge pattern of the triple- q CDW rotates almost rigidly about the c axis, with just 2% increase in λ , to achieve commensurateness in the basal plane with the

† The very slightly twisted orientation taken by the modulation vectors (see § 2.2 (a)) could possibly arise from this trigonality.

'3-by-1' $13^\circ 54'$ -rotated hexagonal repeat in the cation array. This is as portrayed in fig. 14. The regions of charge build-up most probably come to centre around particular cation sites (so anchoring the CDW phase origin). In total for each sandwich there are 13 cations per unit, which, in a cell maintaining hexagonal symmetry (as when following the choice $\Phi' = 90^\circ$), would fall into three types, in the ratio 1 : 6 : 6. In fig. 33 we have indicated the directions in which the cations are likely to move in the cation plane, for a $\Phi' = 90^\circ$ CDW, assuming the displacements act to minimize the charge separation brought in a sinusoidal CDW. Unfortunately Ta is not amenable to a N.M.R. investigation of the site field inequivalencies (unlike Nb in 2H-NbSe_2), and the distortions ($\sim 0.1 \text{ \AA}$) are too severe for N.Q.R. to be useful. It is hoped that neutron-scattering experiments will shortly determine the actual atomic displacements, thereby identifying Φ' .

Fig. 33



Basal plane displacements in the $\sqrt{13}a_0$ superlattice for the cations assuming their motion is simply directed to the charge maxima formed by CDW. We anchor the CDW phase origin at an atom site, and make the phase angle choice $\Phi' = 90^\circ$, as for the high temperature phase. This makes points B and C equivalent (see fig. 31). The sites $a : b : 0$ are in the ratio 6 : 6 : 1. (The arrows here, and particularly in fig. 38, greatly overstate the actual displacements.)

The lock-in transitions studied to date are each accompanied by volume expansions (see table 1) into the low temperature phase, along with the evolution of heat. Given the present amount of data, however, it is not clear if and how this crystallographic response is related to the precise accommodation the CDW has to make at T_d in each case to achieve the $\sqrt{13}a_0$ commensurate geometry. As can be seen in fig. 9 (iii), 4Hb-TaS_2 , for example, makes a 5% reduction in λ at the transition, while the a_0 axis remains unchanged. A major reason for the absence of a clear pattern to the numerical data of tables

1 and 2 is that the situation which exists in 1T-TaS₂ is more complex than for the others (see § 2.2 (c)). If one assumes that in a 4Hb polytype only the octahedral sandwiches are affected at T_d , then the entropy change per mole should be approximately half that in the corresponding 1T polymorph. While this is the case for TaSe₂ (see table 1), the change at T_d for 1T-TaS₂ is observed actually to be somewhat *less* than for 4Hb-TaS₂. We will return to discuss 1T-TaS₂ and its unique multi-stage lock-in behaviour shortly.

(b) *The transition in the mixed coordination polytypes*

Concerning the 4Hb mixed coordination polytypes, it is truly amazing that their properties indicate that the two types of sandwich behave there almost independently of each other. This we see, for example, in the magnitudes of the susceptibilities (see fig. 2), and again in the optical spectra (see Wilson and Yoffe 1969, fig. 22 (i)). Indeed, in transmission 4Hb-TaS₂ is green, compared with blue for 1T and yellow for 2H-TaS₂ ($t \sim 500 \text{ \AA}$). Because of the tight-binding nature of the d-bands in these materials, a band structure can be anticipated which will spatially alternate the character of those bands between successive octahedral and trigonal prismatic sandwiches. In the 4Hb crystal (P6₃/mmc), both types of metal atom find themselves (neglecting the CDW distortions) in the same point symmetry as they do for the respective single coordination polytypes (*viz.* octa.— $\bar{3}m$; trig. pr.— $\bar{6}m2$); the chalcogen atoms are always in 3m sites. Since the Fermi energies in the pure 1T and 2H polytypes are virtually identical, they will be readily matched in the composite 4Hb and 6R types.

The small size of the discontinuity in ρ for 4Hb-TaS₂ at 315°K, along with the positive gradient to the ρ versus T curve below T_d (see fig. 8, in contrast to fig. 3 for the 1T materials), clearly indicates that the trigonal prismatic sandwiches carry most of the current above and particularly below T_d . Since the conductivity within these sandwiches increases on cooling, while conductivity up the c axis is impeded by the low conductivity of the intervening octahedral sandwiches, the resistivity anisotropy becomes exceedingly large, particularly after the low temperature transition at 20°K. At 4°K ($\rho_{\parallel c}/\rho_{\perp c} \approx 10^3$). The material does not become superconducting down to 1°K (Meyer 1974).

Table 3.

$T_{d/o}$ (°K)

TaS ₂			TaSe ₂		
1T	4Hb	2H	1T	4Hb	2H
350			473		
	↘			↘	
		315			410
		↙			↙
		80			120
		↘			↘
		20			75

The 20°K transition we presume to be the analogue of the 80°K transition for 2H-TaS₂ (see § 7), this occurring just in the trigonal prismatic sandwiches. We note that the transition has become first order in the mixed polytype. In all instances the various 4Hb transition temperatures are lower than for the corresponding single coordination case (see table 3). It is not possible to say whether this depression is due to the increased complexity of the 4Hb band structure, to the higher degree of incommensurateness in its CDW wavelengths, or to the lack of cooperative behaviour here between neighbouring sandwiches. T_d certainly is depressed by structural disorder, as produced by substitutional doping, even when this is isoelectronic, e.g. Nb for Ta, Se for S. (Many of the effects obtained via doping are discussed in detail in § 6.) Probably the reason for no low temperature commensurate superlattice appearing in K₂Pt(CN)₄ · 0·3Br · 2·3H₂O is because the extent of the incommensurateness is too high ($\lambda \approx 6\cdot8c_0$), but here again the question of disorder is present in the bromine packing the [Pt(CN)₄] chains.

(c) *Powder X-ray diffraction*

While tilting experiments are helpful in determining the correct l index for a reflection, they are not always conclusive, especially for very thin samples where spot elongation is severe. Electron-diffraction patterns can be thought of as giving a two-dimensional projection of the low l reciprocal lattice planes onto the $l=0$ plane. Two of three indices labelling the reciprocal lattice positions are thus determined by electron diffraction, and the last can be fixed by X-ray diffraction.

A number of samples have been studied in powder X-ray diffraction using a Guinier-De Wolf camera. Since the distortions are small, we only expect to see satellites of type 1 in the X-ray diffraction patterns. In table 4 we list the diffraction patterns observed at room temperature for 1T-Ta_{0·92}Ti_{0·08}S₂, 1T-TaS₂, 1T-TaSe₂ and 4Hb-TaS₂. In general the main lines, labelled with hkl indices, were considerably overexposed on the film, due to the long length of the exposure; consequently their intensity is not given. The intensity of the super-lines for each sample is visually estimated relative to the strongest which is labelled as very strong (vs), while those just at the limit of visibility on the film are labelled as very weak (vw).

The tilting experiments on 1T-(Ta/Ti)S₂ alloys, in which $T_d < 300^\circ\text{K}$, showed that the type 1 satellites were not in the $l=0$ plane, but lie in triangular clusters in planes perpendicular to c_0^* , that intersect at approximately $\pm c_0^*/3$. It would be difficult, however, conclusively to rule out intersection at $c_0^*/4$, or $2c_0^*/5$, or other values close to $c_0^*/3$, due to spot elongation along c_0^* . Using the distance to this intersection point along c_0^* from a main a_0^* spot as a parameter (k_z), powder-diffraction patterns were calculated. Employing the value of \mathbf{q}_0' obtained from electron diffraction for 1T-Ta_{0·92}Ti_{0·08}S₂, the first two lines in the powder-diffraction pattern are calculated to be

k_z	0	$c_0^*/4$	$c_0^*/3$	$2c_0^*/5$	Experiment
Largest	10·9	9·88	9·26	8·75	9·2
d-spacings	5·16	6·35	6·84	7·31	6·8 Å

A $3c_0$ repeat is, we see, confirmed.

We now also conclude that the *superlattice* spots seen in 4Hb-TaS₂ lie in the $l=0$ plane, since the first d-spacing observed, 10.4 Å, is the 100 line for a hexagonal lattice of $\sqrt{13}a_0$, $\left(-\sqrt{13}a_0 \times \frac{\sqrt{3}}{2} = 10.4 \text{ Å}\right)$. Again this result was suspected from the fact that the superlattice spots flared in intensity in electron diffraction at the same time as the main a_0^* spots—a situation not encountered with the 1T polymorphs above T_d . From the fact that the powder-diffraction lines are sharp and are observed on the $l=0$ plane, it seems likely that this 4Hb CDW indeed has locked-in to alternate α and β -rotated states in successive octahedral layers, with the \mathbf{q}_{oi} parallel to the layers. Finally, we should note that the superlattice lines observed for 4Hb-TaS₂ are noticeably weaker than for 1T-TaS₂. Thus we expect the superlattice distortions at room temperature to be smaller in 4Hb-TaS₂ than in 1T-TaS₂.

For 1T-TaSe₂, $T < T_d$, we record in table 4 a great number of superlattice lines, of which the line at 3.88 Å is in fact intense enough to be seen weakly on standard short-exposure films. These data were originally given a tentative assignment in terms of a triclinic cell (Di Salvo *et al.* 1974). Very recently Yamada and LaPlaca, in a single crystal study (to be published), suggested a hexagonal superlattice with $a = \sqrt{13}a_0$ and $c = 12c_0$. Moncton and Axe (1975), however, determine that $c = 13c_0$. Until the distortion details of the CDW/PSD are known, it is not apparent why the superlattice should adopt this long c_0 repeat. Since the superlattice points occur so close to the $l=0$ plane, it is not surprising that they all show in the $l=0$ plane in electron diffraction.

By contrast the X-ray pattern from 1T-TaS₂ for the room temperature state is approximately though not exactly fit by the cell $a = \sqrt{13}a_0$ and $c = 3c_0$. (For example the observed d-spacings 3.79 Å and 3.68 Å differ significantly from those calculated at 3.88 Å and 3.63 Å. This deviation from the $\sqrt{13}$ superlattice was not detected by Brouwer and Jellinek (1974).) It is apparent here, and from the electron diffraction patterns, that between 352°K and 200°K the CDW is not quite commensurate. Williams, Parry and Scruby (to be published) from an extensive X-ray and electron diffraction study of 1T-TaS₂ clearly show that the q_0 do not rotate by the full 13° 54' at the 352°K transition but stop short by $\approx 3^\circ$. Only with the transition at 200°K is the lock-in finally completed, to give a superlattice that is very similar or identical to that of 1T-TaSe₂. It is not clear at the present time why the transition at 352°K stops short of full lock-in, but it is interesting to note that then c remains at $3c_0$ until the final 200°K transition. We shall return to the 1T-TaS₂ case in § 5.2 (e).

(d) *More points concerning the commensurate state properties*

In fig. 13 we have recorded the inverse '3-by-1' rotated relationship which exists between the reciprocal lattices for the parent CdI₂ structure and for the CDW-driven superlattice. There we displayed the virtual equivalence in length of a^* for the (1T-TaSe₂) superlattice, with both the first-order satellite vector and the radius of the smaller ring of diffuse scattering for the phase above T_d , the latter being very close to $(a_0^*/\sqrt{13})$ for pure 1T-TaSe₂. At lock-in, all the first and second-order spotting rotates, each spot about its own zero-order spot. All spots take the same clockwise or anticlockwise sense,

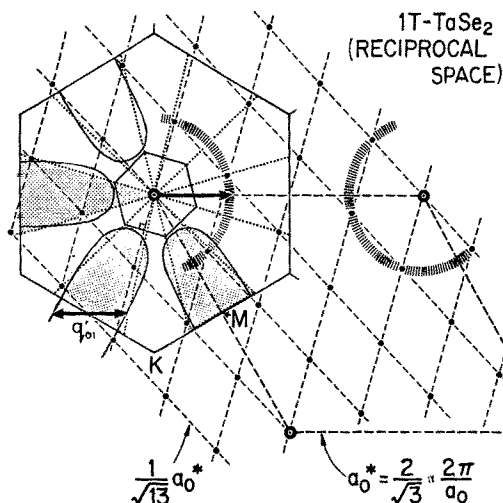
thereby accommodating themselves onto that superlattice net, respectively to denote either a β or a α -oriented domain†.

With fig. 34 we have developed the above figure (13) to include the Brillouin zones for the two phases, the high temperature Fermi surface, and a typical CDW (projected) spanning vector, \mathbf{q}_0' . The dotted wedges, as drawn, divide the parent B.Z. into 12 equal area segments. Since the wedge is of angle $2 \times 16^\circ 06'$, one of its sides passes through the (11·0) oriented reciprocal lattice point of the superlattice net. Such reciprocal lattice points are, in fact, also seen to be incorporated into the paths of the second (larger) circles of diffuse scattering, for which the radius then closely takes the value of $\sqrt{7}a^*$. (Note, here, hexagonal geometry is such that, for that value, the second ring incorporates 12 reciprocal lattice points, rather than just 6 as for the inner rings.)

We earlier ascribed the inner rings to (very probably) phason scattering, associated with the critical Fermi surface spanning wave vector, \mathbf{q}_0 . The larger circles, we now note, seem similarly related to the umklapp vector $-\mathbf{q}_0 + \mathbf{a}_0^*$, although, as we have tried to indicate in fig. 13, a careful examination of plates like fig. 12 (ii) seems to show slight overlap for the two sets of circles. Of these two spanning vectors, $-\mathbf{q}_0 + \mathbf{a}_0^*$ corresponds to $\lambda = 1.38a_0$; and it is only \mathbf{q}_0 that achieves commensurateness at T_d .

Corresponding to what is noted above, any rotated hexagonal superlattice (a_0') in an h.c.p. array (a_0) has all its cell corners at distances from the origin

Fig. 34



The figure portrays, for the simpler case of 1T-TaSe₂, the relationship between the high temperature Fermi surface, one of its critical spanning vectors (in basal projection), q_{01}' , a radius of a smaller ring of diffuse scattering, and the low temperature rotated superlattice. The Brillouin zones for both phases are included. The dotted wedges divide the parent zone into 12 equal area segments. The Fermi surface as drawn is modified slightly from that in fig. 27 (b), to match the experimental value of q_{01} .

† We ignore here, as in fig. 13, the 1° twist in the h.t. spotting that was mentioned in § 2.2 (a). Its presence is clearly apparent in figs. 9 (i), 12 (ii) and particularly fig. 24 (i).

held by 12 atoms, rather than just 6 as for an axial superlattice (see fig. 14). These rotated ($\theta \approx 30^\circ$) superlattices are of side $\sqrt{7}$, $\sqrt{13}$, $\sqrt{19}$, $\sqrt{21}$, $(\sqrt{28})$, $\sqrt{31}$, $\sqrt{39}$, $\sqrt{43}$, $\sqrt{49}a_0 \dots$. Note that the latter 5-by-3-rotated cell, for which $a_0' = 7a_0$, is then associated with an 18-atom peak in $\rho(r)$, a feature that recurs at $13a_0$, etc. It will be interesting to find if this has any influence via $\rho(k)$ in promoting a special stability for the $\sqrt{13}a_0$ superlattice, which the Fermi surfaces have come so close to matching. Certainly, as we shall see in § 6, this superlattice is fairly tenaciously clung to, even when the Fermi surface geometry is changed quite appreciably via doping, etc.

The reduced Brillouin zone of the superlattice phase is $1/13$ of the old zone in cross section, so that, if the bands were to fold neatly into the new zone, the Fermi surface would lie halfway through the seventh band. In fact it does seem, from the three-fold increase in resistivity at T_d for 1T-TaSe₂ (see fig. 3; note also the large increase in R_H found when cooling 1T-TaS₂ through T_d (Thompson *et al.* 1971)), that the total area of the Fermi surface becomes very substantially reduced at lock-in. For the high temperature phase, as we will discuss in § 6, some gapping already exists across the simple band structure in the vicinity of the Fermi surface due to the incommensurate CDW. The low value of χ found *above* T_d (see fig. 2) is related to this loss of free-carrier behaviour. Below T_d the augmented gapping of the superlattice drives χ still closer to the diamagnetic core value (approximately -55×10^{-6} e.m.u./mole for MoS₂, and -100×10^{-6} for WS₂; see Geertsma and Haas (1973)).

Wherever in the zone the gapping from the superlattice geometry is centred at or just below the original Fermi level, appreciable stability will be lent to the superlattice state from the reduction in electronic band energy of the electrons so placed. This is the descriptive form employed by Sato and Toth (see their 1968 review) to interpret the stability of many long-period superlattice orderings in alloys.

In the 1T and 4Hb layer compounds, T_d is reduced quite sharply by the application of pressure (see table 1). Pressure should promote significant changes in band shape for the layer compounds, reducing the two-dimensionality. The depression rate for 1T-TaSe₂ and 4Hb-TaS₂, is close to 5°K/kB (much in fact as for the SDW 'Neel' point in chromium (Fletcher and Osborne 1974)).

Also noteworthy is that T_d falls from the 1T and 4Hb (and indeed 2H) tantalum selenides to the corresponding sulphide, in each case by approximately the molecular weight ratio of 1.38 :

	1T	4Hb	2H
T_d ratio (TaSe ₂ : TaS ₂)	1.35	1.30	1.50

This is not unexpected, since the electronic instability is coupled strongly to the phonon system. The changes brought by substitution of different cations seem to effect the d-band details too severely for such a simple relationship to hold, though the changes are in the appropriate direction.

(e) The complexities of the 1T-TaS₂ case

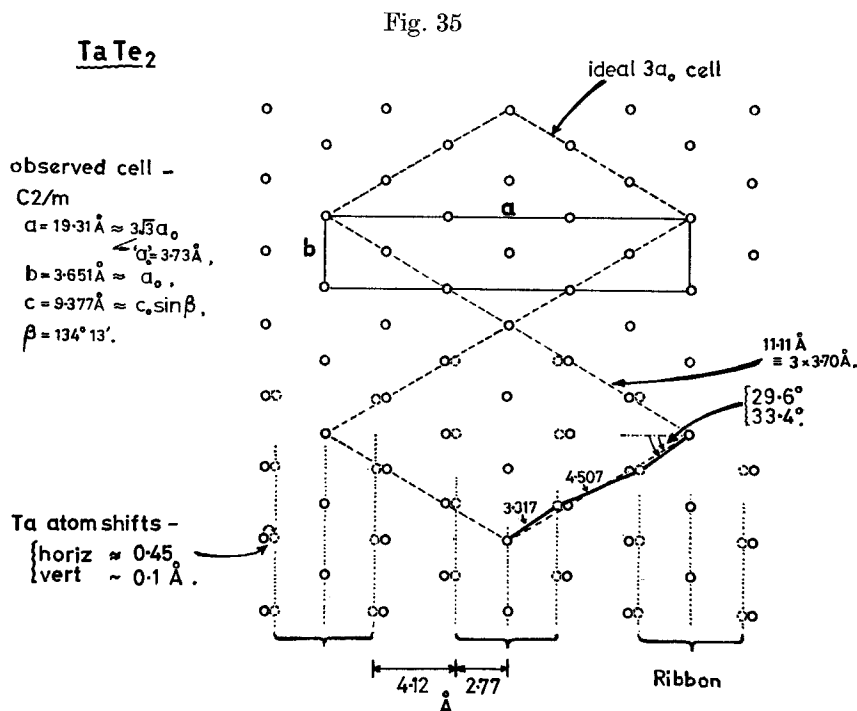
We next offer some comments concerning the rather complex behaviour displayed by the 1T polymorph of TaS₂. As for why 1T-TaS₂ should be unique in these complexities, we perceive no answer. It is only little more incommensurate than is 1T-TaSe₂, and indeed zero mismatch can be achieved by substitutional doping with 2 to 3% Ti, yet the complex state remains (see fig. 21 (iii)). In fig. 21 (v), which is for 6% Ti-doping, we see that although the clear systematics of the 1T-TaS₂ pattern are degenerating, a simple 1T-TaSe₂ type pattern has *not* been achieved. 8% Nb-doping of 1T-TaS₂ yielded fig. 21 (viii), which recalls the 4Hb pattern (although the inner spots are noted to be absent with this flare out condition of the a_0^* spotting). The 4Hb-like spotting [both here and again in selenide figs. (i) (b) and (ii)], is assumed to arise from a drastic reduction in α/β domain size, resulting from the doping. The condition persists to low temperatures. It is worth noting that such doped 1T *sulphide* plates (fig. 21 (iv) and (vii)), invariably show a novel trigonality in the strong spotting, as the morass of fine-structure spotting is drawn towards the 4Hb-like pattern. Presently we are trying to follow the behaviour of the 'superlattice' state through the mixed sulphur/selenide series, which we find extensively to retain the complexities of the pure sulphide, but without the added complexities just mentioned for cation substitution.

As was shown in fig. 18 for 1T-TaS₂, the spots centring the small triangular clusters, in the diffraction pattern from the state obtaining between 350°K and 200°K, do not fall exactly at the vertices of the hexagonal $a_0^*/\sqrt{13}$ net. However, they do form collinear strings (according to our construction) for the spot pairings 1 and 2, 3 and 6, 4 and 8, 9 and 5, 10 and 7, 12 and 11 (in the notation of figs. 17 and 18), which might be taken to radiate from the parent Bragg spotting, after the manner of the first and second-order high-temperature-phase satellite spotting.

Why the rotational adjustment in 1T-TaS₂ should fall short of the full 3-by-1 lock-in (13° 54') in this fashion is not understood. The short-fall is actually greatest right at the 350°K transition ($\sim 3^\circ$ —see fig. 24 (vi)), being reduced to about 2° by room temperature (see fig. 7 (iv) and fig. 18). From the latent heat changes given in table 1, it is seen that the stabilization energy in 1T-TaS₂ at the 350°K transition is only about one-third of that in 1T-TaSe₂ at full lock-in (473°K). Moreover, because of the progressive change in the sulphide below 350°K, this difference does not show up in the subsequent 200°K transition. The resistivity and susceptibility data in figs. 2 and 3 do indicate that less of the Fermi surface is initially removed in the sulphide than the selenide, but that below the 200°K transition the reverse is true. Small differences in band-structure detail throughout the parent zone, prior to folding into the small superlattice zone, will critically determine this transport behaviour.

(f) NbTe₂ and TaTe₂

Apart from in the introduction to § 2, we have not mentioned NbTe₂ and TaTe₂, which, though still structurally based on the CdI₂ type, are fundamentally different from the preceding 1T compounds (see Wilson and Yoffe 1969). The cation shifts range up to almost $\frac{1}{2}$ Å, or 12% of a_0 , and seem much more



The structure of TaTe₂ (based on results of B. E. Brown ; see Wilson and Yoffe 1969, fig. 4), drawn here in terms of distortion from a 3a₀ hexagonal cell. The estimated regular value of a₀ is 3.71 Å (not 3.74 Å, as in W & Y).

related to the situation in WTe₂ (and β-MoTe₂), where d² inter-cation bonding produces a puckered chain distortion, that leaves a virtually semiconducting end product. In the d¹ system we see, however, from the representation of the TaTe₂ structure made in fig. 35, that a simple electron-pair bonding picture will not account for the deformation here. It makes an interesting speculation that the observed ribbonated structure arises initially from a single-*q* CDW, for which λ has fallen from 3.1a₀ in the sulphide and selenide to around 2.6a₀ in the telluride (the value that this view of the structure of fig. 35 would require). The implied adjustment in band structure is readily accounted for, as in NbTe₂ the d(t_{2g}) band starts to overlap with the predominantly chalcogen p-band (Wilson 1974). With the heavier p/d covalent mixing, the states at the Fermi surface then should be sufficiently extended to produce quite strong cation-cation interaction, encouraging large atomic displacements to develop, compared with those for the simpler situation in the sulphide and selenide.

§ 6. CONFIRMATION OF THE CDW INTERPRETATION THE USE OF DOPED AND INTERCALATED CRYSTALS

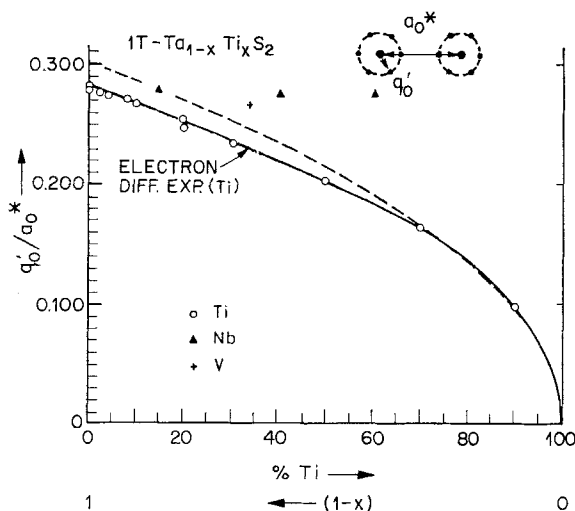
The clearest confirmation of our CDW interpretation of the observed phenomena in the TaS₂ family has come through our doping experiments, where the Fermi surface geometry is altered in a systematic fashion. We start with a section bringing attention to the not insignificant role played by disorder in these experiments, but find it does not affect the crucial result represented

in fig. 36. We close § 6 by showing that the model will explain the anomalies in the electrical, magnetic and optical data, previously listed for these polytypes.

6.1. *A prologue—The effect of doping on the $\sqrt{(13)}a_0$ commensurate transition*

As noted when discussing the diffraction results of fig. 21, the temperature at which the $\sqrt{(13)}a_0$ superlattice is adopted by these systems is quite strongly affected by substitutional doping. We have found from magnetic, electrical and structural experiments that the following levels of cation substitutional doping bring T_d down to room temperature: 1T-(Ta/Ti)S₂, 6% Ti; 1T-(Ta/Ti)Se₂, 10% Ti; 1T-(Ta/Nb)S₂, 5% Nb; 1T-(Ta/V)Se₂, ~5% V. With doping the transition broadens, and becomes ill-defined for $x \geq 15\%$. In no case has T_d been observed to increase above its value in the undoped material. This proves true also for the mixed anion system 1T-Ta(S/Se)₂, when we use the line between T_d for 1T-TaS₂ and 1T-TaSe₂ as reference value. This, together with the very similar effect that introduction either of d⁰Ti sites or of d¹Nb sites has upon T_d , indicates that the prime factor in reducing the lock-in temperature is disorder, and not change in the average electron content, e/a . As one might suspect for a d-band phenomenon, the effect of disorder in the cation site potential proves more active than anion site disorder. It remains

Fig. 36



The q'_0/a_0^* data, contained in fig. 20, is shown against electron content through the series 1T-Ta_{1-x}Ti_xS₂. The selenide data is almost identical. The dotted curve is $q'_0 \propto \sqrt{(1-x)}$, arbitrarily brought into agreement with the experimental data at 75% Ti†. Note $1/\sqrt{13}=0.2773$. q'_0/a_0^* for the 40% Nb doping (fig. 20 (ii)) is 0.274, and similar little-changed values are seen for Se and even V doping.

† At large e/a the experimental data falls below this parabola, as the band structure of fig. 26 (b) would imply, since along ΓM E versus k flattens out approaching Γ .

striking nonetheless that the e/a change brought by group IV substitution should not play a role here of at least comparable importance. In fact, both for 1T-TaS₂ and 1T-TaSe₂, the Fermi surface size is better matched to the $\sqrt{(13)a_0}$ superlattice geometry under 2% to 3% Ti doping than it is for the pure Ta material, yet T_d falls, virtually as under Nb doping. For both, the initial rate of fall is approximately 10°K per per cent substitution. One certainly cannot ascribe this fall in T_d to reduction in volume upon doping (as might possibly mimic the fall in T_d under pressure, see table 1), since T_d is depressed also by substitution of Zr into 1T-TaS₂, and there the molar volume is sharply increased (Benda 1974).

Several of the plates in fig. 21 serve to indicate that the superlattice condition finally established below T_d , in the presence of light doping, is rather severely disturbed. The 4Hb-like patterns seen there reveal that the α/β orientation selection is not maintained over more than a few microns, unlike for the pure materials, where a single domain may extend across the whole crystal. It will be interesting to find how ΔH for the lock-in transition, which is never more than $\frac{1}{3}$ kcal/mole in the pure materials, is reduced by the doping. The lower 200°K transition in 1T-TaS₂, for which ΔH is only 50 cal/mole, is completely removed by $\frac{1}{2}$ % Ti, though it does survive very substantial Se doping.

6.2. *The results from doping to non-superlattice conditions*

Once the $\sqrt{(13)a_0}$ superlattice has been suppressed by Ti doping ($\geq 15\%$), no further superlattices have ever been detected, such as must geometrically be appropriate to other values of e/a through the d¹/d⁰ system. Although we have not investigated the situation structurally to low temperatures, no features occur in the magnetic or electrical data that are suggestive of superlattice formation. In contrast to this sensitivity of long-range lattice commensurate states towards site disorder, there is displayed a remarkable unperturbability towards the creation of the CDW state in the first place (though doubtless the CDW is of much reduced coherence length). This is so despite the fact that the stabilization energy brought by a CDW with $T_0 \approx 600^\circ\text{K}$, is probably only $\sim 5 \times 10^{-2}$ eV per electron or $\frac{1}{2}$ kcal/mole (i.e. $2\Delta \approx 5kT_0$, the CDW gap energy, applied approximately to one-fifth of the d¹ electrons). The value used here for T_0 , we abstract from ρ and χ versus T measurements made at low Ti doping. This doping prevents reversion of the 1T to the 2H phase. We shall make further comments on these electrical and magnetic measurements below, but the details are to be reported separately.

At various points we have implied that the CDW wavelength responds in keeping with changes wrought in e/a by substitutional group IV doping. The diffraction patterns of fig. 20 provide a record, in the ratio q_0'/a_0^* , of just what these changes are. The structure modulation satellites and the diffuse-scattering circles (inner one) are seen steadily to contract back towards the main spotting, as the d-band is progressively emptied. [Relevant to this reduction in the average value of e/a per cation site, it was anticipated that the d-band would be of sufficient width (relative to the degree of matching of the Ti and Ta site potentials) for it to permit the rigid-band approach as a satisfactory first approximation.] Complementing the above very little change of q_0'/a_0^* from that in pure 1T-TaS₂ is signalled in the patterns obtained with

$d^1\text{Nb}$ or V doping. Figure 20 (ii) is such a pattern, here from a sample with 40% Nb substitution (by which stage, we note, the sharp satellite spotting has been lost, and T_d completely suppressed).

Given the reduction in e/a caused by Ti doping, we infer that the results in fig. 20 are indeed monitoring the Fermi surface, as it shrinks back on the ML axes in accord with the calculated band structure (see figs. 26 (b) and 27 (b)). As the tantalum content is reduced, E_F drops to where the bands are increasingly parabolic, causing the Fermi surface to become ellipsoidal, with constant eccentricity. In fig. 36, which records our measurements of q_0'/a_0^* , we show that the plot of q_0'/a_0^* versus doping content indeed tends to a quadratic form as e/a becomes smaller. Results like these (fig. 36) we hold as providing conclusive evidence that the effects seen indeed derive from the Fermi surface. It is particularly convincing when the positive results of IV/V cation mixing are viewed against the absence of any major change in q_0'/a_0^* for V/V mixing. In the latter cases the slight changes detected in q_0'/a_0^* are not inappropriate to the peripheral changes to be expected in band shape, e.g. from spin-orbit coupling. [The band structures of fig. 26 are non-relativistic. Band splitting in the proximity of E_F will occur for the states $\Gamma(3+)$ and $A(3+)$ in 1T (D_{3d}^3), and K(5) and H(2) for 2H (D_{6h}^4).]

Using fig. 36, one notes that the Fermi surface geometry at 20% Ti is suited to a $4a_0$ superlattice; that at 40% Ti to a $\sqrt{(21)}a_0$ '4-by-1' rotated superlattice. Such states, as mentioned above, are not to be detected in any measurements. The diffraction patterns of fig. 20 show that even the first-order structure modulation spotting is highly diffused at all such doping levels. Initially we had further conjectured that there may occur cation migration to produce certain ordered alloy superlattices, this possibility arising whenever the periodicity of the latter should find itself in close conjunction with that deriving simultaneously from the Fermi surface. Unfortunately our model supercells for such accord require x to be in excess of 60%, by which stage the Fermi surface effects are waning rapidly. We obtained no success from long annealing at 500°K (though this, note, is only marginally below T_0 : even so the cation diffusion constant may then be extremely low).

6.3. Further evidence in optical, electrical and magnetic data

A rough estimate of the stabilization energy brought by the 1T CDW was given above at 0.05 eV per d^1 electron. This was derived from a gap equation of approximate BCS form, such as has been found satisfactorily to describe the SDW in Cr (Rice *et al.* 1969, Barker and Ditzemberger 1970). With $T_0 \approx 600^\circ\text{K}$, we expect the average gap, 2Δ , to be $\sim \frac{1}{4}$ eV. The I.R. absorption and reflection spectra (Benda 1974, Barker 1974), unlike the case for chromium, do not show a single rather well-defined peak, but instead display loss throughout the I.R. (and ultimately match up with the low d.c. conductivity). The principal range of anomalous absorption seems to stretch from 0.15 eV to 0.6 eV. The absorption between $\frac{3}{4}$ and $1\frac{1}{2}$ eV we attribute, as earlier, to standard intra-d-band transitions (Wilson and Yoffe 1969, fig. 80). Note that we are for the moment talking about the *incommensurate* state, as attained through doping or elevated temperature. For increasing Ti doping, the anomalous behaviour in the I.R. steadily disappears, so that from about 60% onwards it is possible to fit the data reasonably closely using a Drude plot. However, the relaxation

parameter required is extremely short, being only 10^{-15} sec for $1T\text{-Ta}_{0.4}\text{Ti}_{0.6}\text{S}_2$ (Benda 1974).

For pure $1T\text{-TaS}_2$ when taken below T_d (and still more so below the 200°K transition, Barker (1974)), the I.R. absorption is further complicated by extension of the gapping, due to the superlattice condition. The rapid depression of T_d observed under doping suggests that any simple superlattice gapping is dominated by the underlying CDW correlated gapping. In the ρ versus T plots of fig. 3 we interpret the negative gradient of the plots found in the initial range below T_d as resulting from thermal excitation of substantial numbers of additional free carriers across the smaller superlattice gaps in typical semi-metallic fashion (e.g. WTe_2). The slopes yield a (least) activation energy of about 0.02 eV, or one-tenth that estimated for the CDW itself. [For the mixed coordination polytypes, the $\rho_{\perp c}$ versus T gradient does not show a negative value in this initial range below T_d , (though it is much reduced; see fig. 8), since in these polytypes the greater part of the current passes through their trigonal prismatic sandwiches.]

When similarly examining this region below lock-in, but now using samples lightly doped with Ti, negative ρ versus T gradients continue to be observed. Moreover, there follows no strong reduction in ρ at lower temperatures (for $x \gtrsim 2\%$ in $1T\text{-Ta}_{1-x}\text{Ti}_x\text{Se}_2$). The persistent negative gradient suggests a heavy amount of disorder scattering, and even local trapping. Many of the plates of fig. 21 plainly reveal structural disorder in the superlattice state. ρ versus T plots of this type continue to be obtained for Ti concentrations far beyond those at which lock-in to the $\sqrt{(13)}a_0$ superlattice finishes. Only below about 20°K does the increase in resistivity cease. This type of behaviour is reminiscent of that produced either by extreme disorder, as in $\text{NbN}_{0.9}$ (Fisk and Lawson 1973) and concentrated TiAl and VAl alloys (Mooij 1973), or by spin fluctuation conditions as in PuZn_2 , etc. (Brodsky 1974). As mentioned in § 1, only when the level of Ti doping exceeds 50% does the ρ versus T plot of $1T\text{-(Ta/Ti)S}_2$ finally take on a positive gradient at room temperature and below.

With low doping concentrations $\approx 10\%$ Ti, a positive gradient is, however, ultimately attained *above* about 600°K , and this we take to signify the end of the CDW state, and the onset of more normal free-carrier behaviour. By this stage the resistivities of the $1T$ and $2H$ polytypes have become very comparable (see fig. 3). Actually under the same 600°K conditions, the magnetic susceptibility (fig. 2) of the $2H$ phase is still much higher than for $1T$ ($+100 \times 10^{-6}$ and $+10 \times 10^{-6}/\text{mole}$ respectively). This we take largely to reflect the four-fold difference in their density of states at E_F (fig. 26 (c)).

When a sample, permanently secured by substantial Ti or Nb doping ($\gtrsim 15\%$) in the non-superlattice $1T$ phase, is followed in χ from high to low temperatures, the susceptibility (once $T < T_0$) is found to slide slowly down into negative values. The residual paramagnetism from the 'free' Fermi surface electrons finds itself only slowly insufficient to offset the core diamagnetism, the CDW gapping in the presence of such high disorder being much retarded. The terminal value, however, is close to that found in pure $1T\text{-TaS}_2$, for the range $T_d < T < T_0$.

6.4. Concerning organo-intercalation

Finally we turn to the problem presented in the EDA intercalation plates of fig. 20 (ix) and fig. 22 (i), (§ 2.2 (g)). The size of the rings of diffuse scatter-

ing, while compatible with the stoichiometric geometry of fig. 23 (*b*) and its eight metal atoms per unit cell, is not to be drawn simply from fig. 36. If one were merely to extrapolate the curve of fig. 36 to higher electron contents (and even, thereby, neglect the density of states peak arising from the critical point at Γ), the experimentally implied expansion of the 1T Fermi surface would be completely beyond the 'unaided' electron-donating power of the organic to secure. It is apparent that the detailed shape of the d-band structure must be modified somewhat in the process of intercalation \dagger . Then, unfortunately, we do not get a true measure of the electron-donating power of the intercalate. It is in fact known that the 1T stacking changes to a 3R stacking during EDA intercalation (Meyer 1974). Other sandwich-stacking changes have been reported for pyridine intercalation in 2H-TaS₂ (Parry *et al.* 1974), and likewise for alkali metal intercalation (Omloo and Jellinek 1970). It is through such band-structure changes accompanying intercalation that we can accept a $\sqrt{(13)}a_0$ superlattice state being formed in cyclopropylamine intercalated 2H-TaS₂ (Beal and Liang 1973, fig. 10 (*b*)), when already the superlattice for 2H-TaS₂ is $3a_0$ (see § 7).

Conversely, the latter authors find (*Ibid.*, fig. 3) that when cyclopropylamine is intercalated into 1T-TaS₂, the optical spectrum at 77°K is not like that of pure 1T-TaS₂. Instead, it is of a form which we are now in a position to note comes from having passed outside the $\sqrt{(13)}a_0$ superlattice régime, it being, as they show, rather like that from 1T-Ta_{0.50}Nb_{0.50}S₂. The latter material actually yields a spectrum that upon intercalation changes little over the range 0.4 to 4 eV. Unlike 1T-TaS₂, it shows the presence of free-carrier absorption in the near infra-red.

1T-TaS₂ intercalated by EDA does not become superconducting ($> 0.3^\circ\text{K}$, Meyer 1974), here being similar to pure 1T-TaS₂, or indeed 1T-TaSe₂, which are not superconducting, certainly to well below 1°K. Superconductivity has been detected below 1°K in the 1T-(Ta/Ti)S₂ system, beyond such Ti concentrations as permit the $\sqrt{(13)}a_0$ superlattice to appear at low temperatures (J. Gerber, unpublished).

§ 7. THE CASE OF THE TRIGONAL PRISMATIC POLYTYPES

7.1. Background concerning the low temperature state

It has been known for some time in the case of TaSe₂ that some form of phase change occurs at close to 120°K, in all of its polymorphs possessing trigonal prismatic coordination, 2H, 3R, and 4Ha/c. The plots of magnetic susceptibility versus T were, for example (e.g. Bjerkelund and Kjekshus 1967), found to show a break very reminiscent of antiferromagnetism (although the absolute value of χ was less than for palladium, see fig. 2). Naturally this prompted an N.M.R. investigation, since the complete family of materials was already known to be superconducting. By this investigation (made on 2H-NbSe₂) antiferromagnetism was immediately discounted (Ehrenfreund *et al.*, 1971). However, it was discovered that atomic site field inequivalencies appear in the low temperature phase. The N.M.R. quadrupole satellite peaks of Nb become split quite strongly, into what would seem to be an equally

\dagger The 1 eV band splitting at Γ in 2H-TaS₂ (1+/4-; fig. 26 (*a*)) gives some measure of inter-sandwich interactions.

weighted doublet. This splitting was judged greater, moreover, than could be accounted for by the very small shifts in atomic position indicated in a concurrent crystallographic investigation (again for 2H-NbSe₂; Marezio *et al.* 1972). Although the details in the latter structural refinement were always suspect, since the changes were so slight, it was made apparent that the atomic shifts lay in the range below 0.05 Å, as for 'soft phonon mode' materials like Nb₃Sn (Shirane and Axe 1971 a, b) or SrTiO₃. The conclusions drawn were that the structure remains hexagonal (though following a slight downward break in c/a), and that the N.M.R. results would have to be accounted for by inequivalencies $\sim 5\%$ in the site d-band charges.

In table 1 we incorporated earlier the integrated heat of transition for 2H-TaSe₂. This is only 1 cal/mole; yet it is likely to be the largest value in the family (T_d highest). It reveals how slight the transitions are, compared with say the lock-in transitions of the 1T polymorphs, for which ΔH is two orders of magnitude higher. It also accords with the sensitivity of the transition details to preparation conditions and stoichiometry. This sensitivity appears intriguingly coupled to sensitivity in the superconducting temperatures

Table 5.

	2H-TaSe ₂	2H-TaS ₂	2H-NbSe ₂
Peak in susceptibility	120° (a), (b)	80° (e), (b)	broad (f)†
Break in ρ versus T	110° (a), (b)	75° (e), (b)	(35°) (a)
R_H	120° (a)	65° (e)	40° (a), (f)
[H c]	(start	90°	25°
	+ , 0, -	55°	15°
S	(end	35°	60° (g)
	- , 0, +		25°
peak			
T_o structural	120° (b), (c)		35° (c)
T_c	0.2°	0.8°	7.3°K
$\partial T_c / \partial P$	(< 3×10^{-5}) (d)	+ 5×10^{-5} (d)	+ 6×10^{-5} (i), (j) °K/bar

(2H-NbS₂ becomes superconducting at 6.1°K, and no structural change is reported via N.M.R. down to this temperature (k). A structural change below 4°K has possibly been detected in the electron microscope (l).

References

- (a) Lee *et al.* (1970).
 (b) This work and earlier papers.
 (c) Moncton and Axe (1975).
 (d) Schwall, Thesis, Stanford (May 1973).
 (e) Thompson, Gamble and Koehler (1972).
 (f) Marezio *et al.* (1972).
 (g) Huntley and Frindt (1974).
 (h) Geballe (1972).
 (i) Yamaya and Sambongi (1972).
 (j) Jones *et al.* (1972). (Note their null result on NbS₂ is with the 3R polymorph in fact.)
 (k) Ehrenfreund, Gossard *et al.* (1972).
 (l) Fernandez-Moran, Monterey Conf. on layered comps., 1972, unpublished.

(Brackets in table denote experiments not definitive; gaps denote no results yet.)

† The peak in χ seen by Lee *et al.* (1970) appears to be due to oxygen contamination.

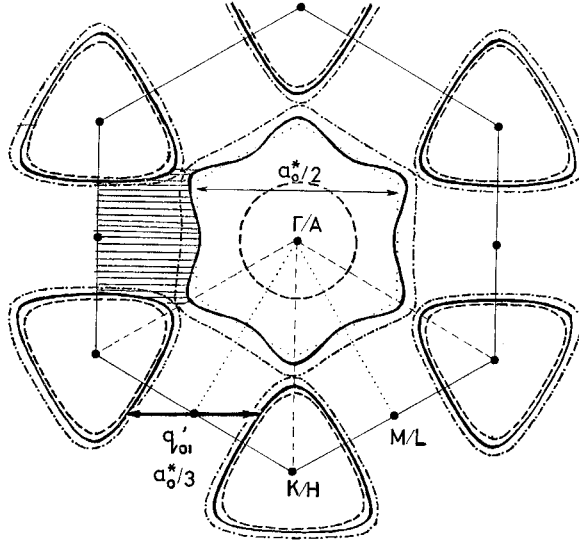
(as for the martensitic transition in V_3Si , and Nb_3Sn). Huntley and Frindt, in a forthcoming paper, display the especially high sensitivity of the transition in $NbSe_2$, through a comparative plot of Hall coefficient versus T for a selection of specimens. Although the transition is slight, the Hall coefficient in fact undergoes in its vicinity a change in sign, as first reported by Lee *et al.* (1970). The Seebeck coefficient shows almost as marked a change (Geballe 1972). For $2H-NbSe_2$ the ability to transform is possibly destroyed by cycling to pressures in excess of 1 to 2 kBar; the superconducting transition temperature (T_c) is thereby increased (Yamaya and Sambongi 1972). T_c increases rapidly for TaS_2 and particularly $NbSe_2$ up to pressures of 25 kBar, but this is not so for $2H-TaSe_2$, where T_0 is probably too far removed from T_c . Correspondingly, no change is found in T_c for NbS_2 , for which, if a structural transition exists at all, it lies below T_c . These facts are summed up in table 5.

7.2. *The low temperature state related to the band-structure results*

As was presented in § 2.2 (*d*), we now know that the structure of the low temperature phase is a $3a_0$ superlattice, defined by very slight modulations in atomic position. In addition to the case of $2H-TaSe_2$, this periodicity is now also confirmed for $2H-NbSe_2$ (Moncton and Axe 1974), and we presume it to be general to the family. In fig. 27 (*a*) we have presented the Fermi surface as derived from Mattheiss' band structure of fig. 26 (*a*). From this diagram it seems quite likely that the same form of critical spanning is involved here as was the case for the 1T CDW; viz. at the centre of the Brillouin zone walls, by the triple set, \mathbf{q}_{0i} , having basal projections parallel to ΓM . The very recent band structure by Fong and Cohen (1974), though showing some differences of detail, and unfortunately not being calculated for the crucial symmetry lines MK and LH, would seem, with a Fermi level falling at 0.3 eV on their (arbitrarily positioned) energy scale, to lead to virtually the same Fermi surface as above; in particular, a Fermi surface that intersects the zone walls just about half-way from the ML to the KH axes. We show in fig. 37 the (Mattheiss') Fermi surface as it intersects the planes AHL and ΓKM . Away from the former plane, the surface becomes two-sheeted, this resulting from the presence of two molecules per unit cell. Possibly it is this fact which prevents a CDW state in the 2H polytypes from providing the same degree of stabilization of the ground state that it does in the 1T polytypes. It should be further noted on this point that with a hexagonal $3a_0$ superlattice, for which the maxima in the CDW are centred on atom sites, the minima also automatically find themselves similarly centred. This can be seen in fig. 38 (*a*) in which we have shown the directions of the cation displacements to be expected for a $\Phi' = 90^\circ$ CDW (see § 5.1). Still to be reconciled with the N.M.R. results is the fact that here there are not just two but three site types per cell, present in the ratio 1 : 2 : 6†. Given the presence of the superlattice, it is of course clear why the very low temperature magneto-thermal oscillation data (Graebner 1973) does not fit the simple band structure. The details of the band folding into the reduced Brillouin zone of

† Note if the CDW origin is shifted to lie symmetrically between three cations, the atom site ratio will reduce to 6 : 3, should one consider only the local charge in the CDW (fig. 31 (*a*)), and neglect the atomic displacements (fig. 38 (*b*)).

Fig. 37



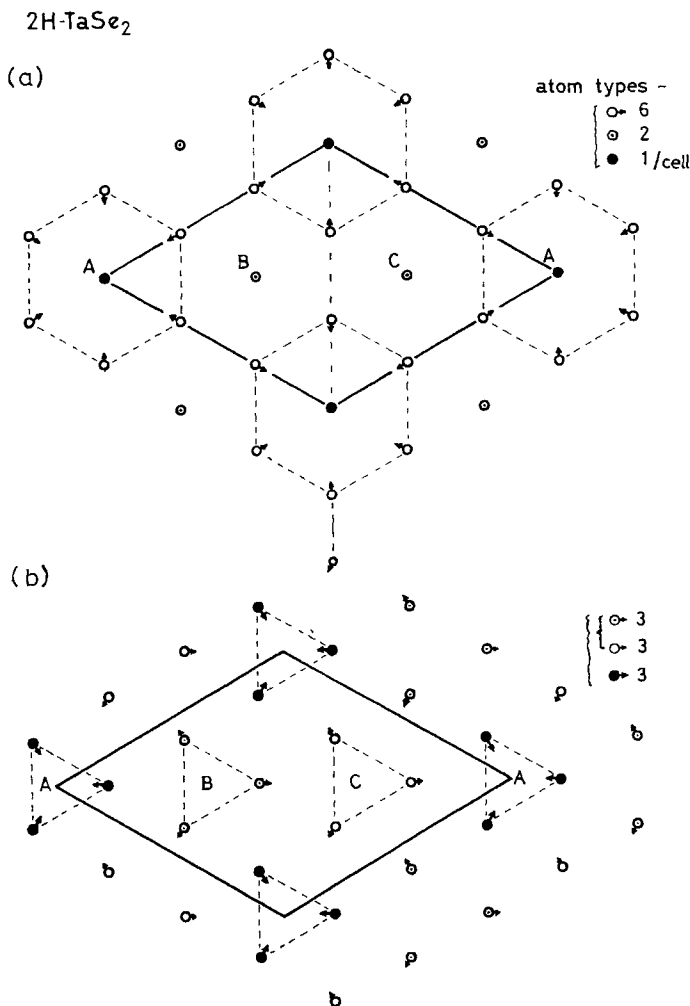
The two-sheeted Fermi surface of 2H-TaS₂ in horizontal section (see fig. 27), showing the common AHL section (\sim), and the two Γ KM sections (----- lower band; - · - · - upper band). One of the critical spanning vectors q_{oi} (horizontal projection) that probably produces the $3a_0$ superlattice is indicated, along with the vector probably determining the $2a_0$ superlattice (§ 7.4).

the $3a_0$ superlattice are likely to remain a mystery for some time, and, with this, so are the remarkable changes in Hall and Seebeck coefficients. It is not likely, either, that the band-structure calculations will be made sensitive enough to perceive whether differences in the density of states at the Fermi level play a role in determining T_0 , and in the amplitude of the CDW below this temperature.

Calorimetrically determined electronic specific heats (γ_{es}), of course, refer to the superlattice condition (with the exception of 2H-NbS₂, for which only unconfirmed data exist). According to the calculated density of states, $N(E_F)$ prior to the transition is quite high ($\sim 3/eV$ -‘cation’ spin, as for V₃Si), and is critically placed at a very sharp peak in the density of states (fig. 26 (c)). The experimental value of γ_{es} for 2H-NbSe₂, at 16 mJ/mole °K², shows $N(E_F)$ to remain high below T_d . This value of γ_{es} is found to decrease with organo-intercalation, the reverse of what is found for 2H-TaS₂. The details clearly are highly individual. However, what does seem general is that an increase in γ_{es} produces an increase in T_c . For 2H-TaS₂, such an increase in γ_{es} follows upon either organo-intercalation or substitution of selenium for sulphur. As we will see in the next subsection, both these actions are in fact found to incur a suppression of the superlattice state.

A representative selection of data relating to the above matters is given in table 6. Much data contained in the Stanford Ph.D. theses of J. F. Revelli, R. E. Schwall, J. A. Benda and S. F. Meyer remains unpublished.

Fig. 38



Basal plane displacements in $3a_0$ superlattice (compare fig. 33). The choice $\Phi' = 90^\circ$ is still made; in (a) origin is retained at an atom site to preserve hexagonal symmetry for distorted phase; in (b) origin is displaced to the off-site position.

7.3. The magnetic, electrical and optical properties The suppression of T_0

As one suppresses the 'amplitude' of the low temperature state in $2H-TaS_2$, via organo-intercalation (with its changes in band structure and conduction electron content), or alternatively via selenium substitution (with its concomitant lattice strain), the peak in χ falls and broadens (Di Salvo 1972 and unpublished, Murphy *et al.* 1974), and the resistivity anomaly is likewise removed. The latter anomaly in ρ at T_0 (see Thompson, Gamble and Koehler 1972) takes the classic form for a second-order transition (or in fact very much as for the SDW onset in chromium, see Barker and Ditzinger 1970; fig. 12).

Table 6.

	2H-TaS ₂	2H-TaS ₂	2H-NbSe ₂	2H-NbS ₂	4Hc-Ta(S _{0.8} Se _{0.2}) ₂	2H-TaS ₂ · PVr _{1/2}	4Hb-TaS ₂	1T-TaS ₂	1T-TaSe ₂	TaTe ₂
<i>T</i> ₀ (°K)	120	80	35	(< 4)	~105	Fully suppressed	20 (trig. prism)	—	—	—
<i>θ</i> _D (°K)	136 (k)	174 (l)	154 (l)	200	145 (l)	94 (l)	172 (j)	135 (e)	—	—
<i>β</i> (mJ/mole °K ⁴)	0.72 (k)	0.37 (l)	0.53 (l)	?0.3 (o)	0.63 (l)	2.32 (l)	0.38 (j)	0.71 (e)	0.9 (o)	—
<i>T</i> _c (°K)	0.15	0.8	7.3	6.1	3.85 (k)	3.4 (l)	< 1.1 (j)	< 0.07	< 0.05	—
<i>γ</i> (mJ/mole °K ²)	5.1 (k)	8.5 (l)	16.5 (l)	?10.7 (o)	11.2 (l)	9.1 (l)	2.9 (j)	{1.4 (a) 4.2*	{0.3 (e) 2.5*	3 (o)
<i>N</i> _{BS(0)} (eV ⁻¹ molecule ⁻¹)	1.53 (k)	1.19 (l)	1.73 (l)	—	1.3 (l)	1.0 (l)	~0.5 (j)	—	—	1.3 (o)
<i>χ</i> (<i>T</i> _d) [†] (e.m.u./mole) × 10 ⁻⁶	+ 155 (b)	+ 180 (b)	+ 200 (e)	—	[2H·]_{+150} (b)	+ 95 (c)	+ 60 (> <i>T</i> _d) (d)	- 7 (> <i>T</i> _d) ^(e)	- 20 (> <i>T</i> _d) (e)	- 45 (b)
<i>R</i> _H (<i>T</i> _d) [‡] (C ⁻¹ cm ⁻¹) × 10 ⁻⁴	+ 2 (h) §	+ 2 (n)	+ 4 (h), (f), (g)	—	—	—	—	- 0.6 (m)	—	+ 32 (o)
(< <i>T</i> _d)	- 2	- 4.5 (n)	- 12 (max)(g)	—	—	—	—	- 1.0 (m)	—	—

† *χ* here uncorrected for diamagnetism.
 § *R*_H ≤ 3 corresponds (on one band model) to an electron density > cation density, (1.55 × 10²² for TaS₂; 1.7 × 10²² cm⁻³ for TaSe₂).
 ¶ For 1T-Ta_{0.3}Ti_{0.7}S₂ *γ* has risen to 4.0 (a) mJ/mole °K².
 || With diamagnetic contribution from organic removed.
 * For all the 'anomalous' 1T materials, plots of *C_v/T* versus *T*² show unexplained non-linearity for *T* ≤ 4°K, leading to this value.

[Please note this table is meant to provide a representative and not an exhaustive documentation of existing data.]

References

(a) Benda, Thesis (1973).
 (b) Di Salvo—earlier results updated.
 (c) Di Salvo (1972).
 (d) Di Salvo, Bagley *et al.* (1973).
 (e) Di Salvo *et al.* (1974).
 (f) Geballe (1972).
 (g) Huntley and Frindt (1974).
 (h) Lee *et al.* (1970).
 (i) Marezio *et al.* (1972).
 (j) Meyer (1974)—Thesis.
 (k) Revelli (1973)—Thesis.
 (l) Schwall (1973)—Thesis.
 (m) Thompson, Gamble and Revelli (1971).
 (n) Thompson, Gamble and Koehler (1972).
 (o) van Maaren and Harland (1969).

Approaching T_0 from above, there is evidence of growing critical scattering, corresponding to the diffuse scattering seen in electron diffraction (fig. 7 (vi)). Occurring immediately below T_0 is a small hump in ρ , extending over perhaps 20°K, that probably derives in large part from the changing number of carriers as the gapping develops. The materials offer interesting possibilities for critical exponent work. The temperature range of the fluctuations seems more limited here than in chromium or dysprosium (theory for which has recently been presented; Kasuya and Kondo 1974), and much more so than for typical alloy disordering (see Thomas *et al.* (1973), concerning 'Fe₃Al'). For 2H-TaS₂ and TaSe₂, the hump in ρ associated with T_0 comes just where the temperature exponent is passing from T^2 to T^1 (approx.) behaviour, and it is rather difficult to choose a base line. Consequent upon pyridine intercalation into 2H-TaS₂, with suppression of T_0 , ρ retains the gradient of its high temperature curve, and does not drop to the low values shown by all the pure 2H materials (Thompson, Pisharody and Koehler 1972); though ultimately the intercalated material does still become superconducting, and with a higher T_c than for 2H-TaS₂. The same is true for the mixed system Ta(S/Se)₂ (Revelli, thesis; Revelli and Phillips 1974).

The above pattern of behaviour with regard to the suppression of T_0 is also to be seen in the I.R. spectra, (Benda *et al.* 1974). For Ta(S_{0.8}Se_{0.2})₂ and its pyridine intercalate, a normal free-carrier behaviour occurs, but with pure 2H-TaSe₂ quite marked absorption is found (at 4°K) in the range from 0.1 to 0.5 eV. This is, however, nothing like the general disruption of the Drude tail that was observed in the 1T polymorphs (see fig. 4). The absorption peak in 2H-TaSe₂ actually occurs at around $\frac{1}{4}$ eV, which is about five times higher than would be expected (for $T_0 = 120^\circ\text{K}$) from the BCS-like gap equation, $2\Delta = 5kT_0$, that earlier proved successful for the chromium SDW. However, it must be noted that the agreement for chromium related to the *incommensurate* state only. When very small amounts of Mn, Ru or Fe are doped into Cr securing the commensurate state, the peak in absorption is in fact shifted from 0.15 eV up to 0.4 eV (Barker and Ditzenberger 1970). In 2H-TaSe₂, at 4°K we are similarly confronted with a lattice commensurate state, even though there is not found the very large discontinuity in ρ at T_d , which appears for Cr : 3% Fe, (*Ibid.*, fig. 15 (a); see also Kotani 1974).

7.4. Other questions concerning the stability of the $3a_0$ CDW

We have endeavoured for 2H-TaSe₂ to discern some degree of incommensurateness inherent in the diffuse critical scattering seen above the 120°K transition, and conclude it not to be more than 2 or 3%. As we have seen above, in clear contrast to the 1T polymorphs, it is not apparent from our data that a static incommensurate CDW pre-exists the superlattice state. T_d and T_0 , then, appear to be the same, although the onset transition at 120°K does seem second order†. It is possibly only this chance proximity of the $3a_0$ commensurateness that allows the CDW state to develop at all in the

† Recent results separating T_0 and T_d have now been obtained for 2H-TaSe₂ by Moncton and by Barmatz.

trigonal prismatic polymorphs, since there is forced to be a conflict here between the sheets of the Fermi surface, not present for the 1T polymorph. It remains to be discovered just if and how the varying extent of suppressed incommensurateness (pre-determined in each parent Fermi surface) helps govern the changes in $T_{o/d}$ and also the amplitude of the CDW when we pass through the 2H family from TaSe₂ to NbS₂. Already, at the end of § 5.2 (*d*), we noted the possible rôle played by the molecular weight in determining the transition temperatures. From the scanty data available on the 3R and 4Ha/c polytypes (Bjerkelund and Kjekshus 1967, Revelli and Phillips 1974), it seems T_o is rather insensitive to the band-structure modifications that these structural changes must bring. Indeed we find it somewhat surprising that $3a_o$ critical scattering becomes visible at room temperature in samples modified by either excess metal in the van der Waals gap sites (Ta_{1.08}Se₂), or by cation substitution (Ta_{0.92}W_{0.08}Se₂). We have not in these cases, either, as yet made careful enough measurements to detect any small change in the diffuse electron scattering away from the $3a_o$ positions. (Substitution of 20% W is, unfortunately, found completely to suppress the susceptibility anomaly.) Electrons added in the above manner would, from an inspection of the band structure, seem likely to be incorporated principally into states around the Γ A axis, thereby not too greatly changing the MK intercept of the Fermi surface.

When samples again of formula M_{1+x}X₂ are produced, but now probably containing chalcogen vacancies rather than metal excess, as from heating or the deintercalation of sulphur-extracting organics, we are confronted by a quite different result. This is the appearance of a $2a_o$ superlattice (see figs. 19 (v) and (vi)). The onset temperature for this condition lies well above room temperature. If this were also to represent a CDW-driven superlattice, $2a_o$ is in fact most compatible with critical spanning across the centre of the zone, parallel to Γ M, but in the end planes of the zone. The Fermi surface (see fig. 37) would actually be more favourable to the $2a_o$ condition arising via such ALH plane interactions, if the d-band splitting in the Γ MK plane were to be increased. An increase in the splitting of the 'd_{z²}'-band would follow upon an increase in inter-sandwich interaction, such as will arise if the van der Waals gap spacing is reduced. This may well be the case following deintercalation and chalcogen loss. Likewise, it is feasible that the $2a_o$ superlattice is the phase reached in NbSe₂ by the application of 33 kB pressure at 300°K (Frindt *et al.* 1972), since a pressure of 30 kB would produce a 5% contraction in c_o (Jones *et al.* 1972) that will occur disproportionately in the vdW gap. It is not likely that the phase reached is the $3a_o$ superlattice condition, forced up to room temperature. For the 2H phase it is known that pressure increases the superconducting temperature, which probably implies $T_d(3a_o)$ falls under pressure (as the preliminary Hall coefficient data of Yamaya and Sambongi (1972) would suggest).

Under pressure (and particularly through the 30 kB transition) the anisotropy in resistivity of NbSe₂ is observed to decrease from a room conditions value of 30 to a figure below 10 (Frindt *et al.* 1972). A comparable drop in conduction anisotropy was also observed on cooling 2H-NbSe₂, beginning rather sharply at about 75°K (Edwards and Frindt 1971). This again has been attributed, and falsely so we believe, to the $3a_o$ transition rising. It seems likely that the reduction in c -axis conductivity above 75°K most probably

comes with activation of the inter-sandwich 'bumping' mode (B_{2g}^2). For NbSe₂ the rigid sandwich 'rubbing' mode (E_{2g}^2) occurs at 30 cm⁻¹ (Wang and Chen 1974), and, using the ratio of 1.6 between these two modes displayed by MoS₂, we arrive at a value of 50 cm⁻¹ (or 75°K) for the B_{2g}^2 mode, so crucial to *c*-axis scattering. Note that these mode frequencies are somewhat higher in NbSe₂ than in MoSe₂. This is presumably a reflection of the metallic bonding in the d¹ material, as is also the reduced chalcogen-chalcogen 'vdW' length of the group V materials.

§ 8. SUMMARY

We feel that the results and discussion given in this paper provide new direction to work on the metallic layered compounds—the properties of which were increasingly being regarded as 'anomalous'. It now seems that these unusual properties follow, virtually without exception, from the occurrence of charge density waves.

By focusing on the changes (structural, magnetic, optical, thermal, etc.) which occur in these materials at a variety of first and second-order transitions, perception was gained of the underlying electronic conditions. In the 1T polymorphs the transitions that occur somewhat above 300°K represent the move into a commensurate aspect for a pre-existing incommensurate CDW. It is found with the aid of slightly Ti-doped samples that the onset temperature for this incommensurate state is up at approximately 550°K. For the trigonal prismatic polytypes, all the transitions are much slighter and now occur at low temperature. The lower amplitude of the CDW in the latter polytypes is attributed to their more complex band structure.

Through extensive doping experiments on the 1T materials, we have related the electronic instability represented by the CDW, to a divergence arising in $\chi(q)$ from a particular spanning of the Fermi surface. We have also accounted for the observed orientational details of the instability wave-vector in a physically meaningful manner. Substitutional doping yields interesting disorder effects with regard to lock-in of the commensurate phase. All cation doping, even when isoelectronic, ultimately suppresses lock-in. The 4Hb polytype throughout presents a remarkable combination of the 1T and 2H properties, appropriate to its *c*-axis alternation in sandwich coordination type. The neutron diffraction work (Moncton and Axe) will throw considerable light on the details of the various crystallographic distortions and superlattices, as well as on phasons and the growth in amplitude of the CDW below T_0 and on the critical phenomena above.

Charge-density wave formation is general to the d¹/d⁰ layer metal family, in large part, it seems, because of the form and simplicity of the Fermi surfaces. Because of the low (d-)electron content, the Fermi level lies in the very bottom of the d-band complex. This, moreover, is not overlaid by an s-band, as in the transition metal elements themselves, nor by the anion p-band, as in many other metallic T.M. compounds. All these factors help to contribute to a simple Fermi surface, to which then the layered structure of the materials further adds its high degree of two-dimensionality. Such a Fermi surface greatly favours the possibility of a critical divergence occurring in $\chi(q)$. This is

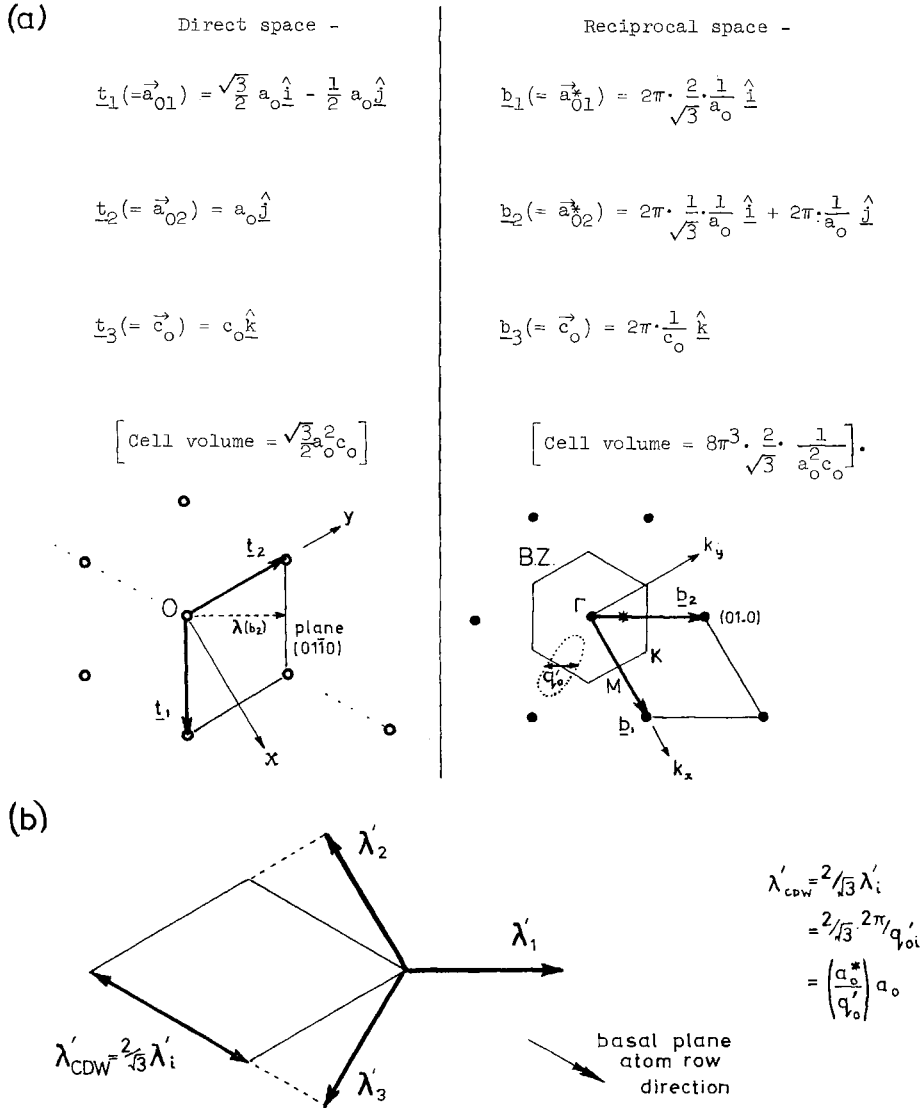
additionally promoted by the high electron-phonon and electron-electron interactions present in these materials; materials that are not too greatly removed from the Mott transition. Accordingly, interesting magnetic effects may be produced by light doping with more magnetic ions like iron or uranium. It should be particularly interesting to find a system that will pass from a CDW to an SDW state beyond a certain doping level. What will doubtless also be probed further is the relationship between the CDW state and superconductivity, and between the lattice instabilities and T_c . We are extending the above studies on the metallic layered compounds to incorporate a still wider range of mixed systems, particularly with regard to magnetism and to disorder. We also hope to investigate more closely the effects of the CDW instability on the physical properties of metallic systems, and to determine if they are a rare or relatively common occurrence.

ACKNOWLEDGMENTS

We would like to express our thanks to R. D. Lowde (A.E.R.E., Harwell), D. E. Moncton (M.I.T.), J. D. Axe (Brookhaven), and S. A. Werner (Ford Motor Co.), and also to our colleagues P. W. Anderson, A. S. Barker, A. C. Gossard, L. F. Mattheiss and T. M. Rice at Bell Laboratories for helpful comments received at various stages in the development of this work. We are also grateful to those who have helped from time to time with the electron microscopy; to A. G. Cullis, M. L. Green, and P. Petroff at Bell Laboratories, and especially to L. A. Freeman of the Cavendish who helped in the initial stages of this work. We are also particularly indebted to J. V. Waszczak, for his energetic and expert technical assistance, as likewise we are to the continued collaboration with T. H. Geballe and his students at Stanford.

APPENDIX

For space groups with hexagonal Bravais lattice (inc. D_{6h}^4 and D_{3d}^3)



(a) Relationship between direct and reciprocal space for space groups with hexagonal Bravais lattice, (inc. D_{6h}^4 and D_{3d}^3). (b) Orientation and size of the repeat unit for a CDW formed from three in-phase waves directed 120° apart (basal plane projection).

REFERENCES

ALLPRESS, J. G., 1972, *5th N.B.S. Symp. Mat. Res.*, Publication 364, p. 727.
 AMELINCKX, S., 1964, *Solid St. Phys.* [EST], Suppl. 6, § 10.
 BACHMAN, R., KIRSCH, H. C., and GEBALLE, T. H., 1971, *Solid St. Commun.*, 9, 57.
 BAGLEY, B. G., DI SALVO, F. J., BAIR, H. E., and VOGEL, E. M., 1975 (to be published).
 BARIŠIĆ, S., 1972 a, *Phys. Rev. B*, 5, 932, 941 ; 1972 b, *Annls Phys.*, 7, 23.

- BARIŠIĆ, S., BJELIŠ, A., and ŠAUB, K., 1973, *Solid St. Commun.*, **13**, 1119.
- BARIŠIĆ, S., and ŠAUB, K., 1973, *J. Phys. C*, **6**, L367.
- BARKER, A. S., and DITZENBERGER, J. A., 1970, *Phys. Rev. B*, **1**, 4378.
- BARKER, A. S., 1974 (unpublished results).
- BATTERMAN, B. W., MARACCI, G., MERLINI, A., and PACE, S., 1973, *Phys. Rev. Lett.*, **31**, 227.
- BEAL, A. R., and LIANG, W. Y., 1973, *Phil. Mag.*, **27**, 1397.
- BENDA, J. A., 1974, *Phys. Rev. B*, **10**, 1409; see also Stanford Ph.D. Thesis, 1973.
- BILLINGHAM, J., BELL, P. S., and LEWIS, M. H., 1972, *Acta crystallogr. A*, **28**, 602.
- BJERKELUND, E., and KJÆKSHUS, A., 1967, *Acta chem. scand.*, **21**, 513.
- BRODSKY, M., 1974, *Phys. Rev. B*, **9**, 1381.
- BROMLEY, R. A., MURRAY, R. B., and YOFFE, A. D., 1972, *J. Phys. C*, **5**, 759.
- BROUWER, R., and JELLINEK, F., 1974, *Mater. Res. Bull.*, **9**, 827.
- BROWN, B. E., 1966, *Acta crystallogr.*, **20**, 264.
- BURSILL, L. A., 1972, *5th N.B.S. Symp. Publication*, **364**, 727.
- BUTLER, M. A., and GUGGENHEIM, H. J., 1974, *Phys. Rev. B*, **9** (in the press).
- CARTER, C. B., and WILLIAMS, P. M., 1972, *Phil. Mag.*, **26**, 393.
- CASTLES, J. R., COWLEY, J. M., and SPARGO, A. E. C., 1971, *Acta crystallogr. A*, **27**, 376.
- CHAN, S.-K., and HEINE, V., 1973, *J. Phys. F*, **3**, 795.
- CHU, C. W., HUANG, S., HAMBOURGER, P. D., and THOMPSON, A. H., 1971, *Physics Lett. A*, **36**, 93. (Certain mistakes exist here.)
- CHU, C. W., and TESTARDI, L. R., 1974, *Phys. Rev. Lett.*, **32**, 766.
- COMES, R., LAMBERT, M., LAUNOIS, H., and ZELLER, H. R., 1973 a, *Phys. Rev. B*, **8**, 571; 1973 b, *Phys. Stat. Sol. B*, **58**, 587.
- CONROY, L. E., and PISAHARODY, K. P., 1972, *5th N.B.S. Symp. Mater. Res.*, Publication **364**, 663.
- COOKE, J. F., DAVIS, H. L., and MOSTOLLER, M., 1974, *Phys. Rev. B*, **9**, 2485.
- COWLEY, J. P., and WILKINS, S., 1970, *Batelle Conf. on Critical Phenomena*, Gstaad, p. 265.
- DI SALVO, F. J., 1972, *L.T. XIII (Denver), Conf. Proc.*, Vol. 3 (Plenum Press), pp. 417-27.
- DI SALVO, F. J., BAGLEY, B. J., VOORHOEVE, J. M., and WASZCZAK, J. V., 1973, *J. Phys. Chem. Solids*, **34**, 1357.
- DI SALVO, F. J., MAINES, R. G., WASZCZAK, J. V., and SCHWALL, R. E., 1974, *Solid St. Commun.*, **14**, 497.
- DONIACH, S., 1974, *Electronic Structure and Related Properties of Actinides*, edited by A. J. Freeman and J. B. Darby (New York: Academic Press).
- EDWARDS, J., and FRINDT, R. F., 1971, *J. Phys. Chem. Solids*, **32**, 2217.
- EDWARDS, L. R., and FRITZ, I. J., 1973, *A.I.P. Conf. Proc.*, **18**, 401 (Ann. Mag. Conf., Boston).
- EHRENFREUND, E., GOSSARD, A. C., and GAMBLE, R. F., 1972, *Phys. Rev. B*, **5**, 1708.
- EHRENFREUND, E., GOSSARD, A. C., GAMBLE, F. R., and GEBALLE, T. H., 1971, *J. appl. Phys.*, **42**, 1491.
- EHRENFREUND, E., RYBACYEWSKI, E. F., GARITO, A. F., and HEEGER, A. J., 1972, *Phys. Rev. Lett.*, **28**, 873.
- ENDO, Y., SHIRANE, G., ISHIKAWA, Y., and TAJIMA, K., 1973, *Solid St. Commun.*, **13**, 1179.
- FEHLNER, W. R., and LOLY, P. D., 1974, *Solid St. Commun.*, **14**, 653.
- FLETCHER, G. C., and OSBORNE, C. F., 1974, *J. Phys. F*, **3**, 75.
- FISK, Z., and LAWSON, A. C., 1973, *Solid St. Commun.*, **13**, 277.
- FONG, C. Y., and COHEN, M. L., 1974, *Phys. Rev. Lett.*, **32**, 720.
- FRINDT, R. F., MURRAY, R. B., PITT, G. D., and YOFFE, A. D., 1972, *J. Phys. C*, **5**, L154.
- GAMBLE, F. R., OSIECKI, J. H., and DI SALVO, F. J., 1971, *J. chem. Phys.*, **55**, 3525.
- GAUTIER, F., KRILL, G., PANISSOD, P., and ROBERT, C., 1974, *J. Phys. C*, **7**, L170.
- GEBALLE, T. H., 1972, *A.I.P. Conf. Proc.*, No. 4, Supercond. in d- and f-Metals, p. 237.

- GEERTSMA, W., and HAAS, C., April 1973, *IVth Intl. Conf. on T. M. Compounds*, Geneva, p. 134.
- GRAEBNER, J. E., 1973, *Bull. Am. phys. Soc.*, **18**, 386.
- GUINIER, A., 1963, *X-Ray Diff. in Crystals, Imperfect Crystals and Amorphous Bodies*, Eng. Ed. (San Francisco: W. H. Freeman) (§ 7.2.1).
- HASHIMOTO, S., and OGAWA, S., 1970, *J. phys. Soc. Japan*, **29**, 710.
- HERRING, C., 1966, *Magnetism*, Vol. 4, edited by Rado and Suhl (Academic Press).
- HUISMAN, R., 1969, Ph.D. Thesis, Groningen, Neth.: see also *J. less-common Metals*, **17**, 111 (Huisman, R. and Jelinek, F.).
- HUNTLEY, D. J., and FRINDT, R. F., 1974 (to be published).
- JONES, R. E., SHANKS, H. R., FINNEMORE, D. K., MOROSIN, B., 1972, *Phys. Rev. B*, **6**, 835.
- KASUYA, T., and KONDO, A., 1974, *Solid St. Commun.*, **14**, 249.
- KOTANI, A. (née SHIBATANI), 1974, *J. phys. Soc. Japan*, **36**, 103.
- LEE, H. N. S., GARCIA, M., MCKENZIE, H., and WOLD, A., 1970, *J. Solid St. Chem.*, **1**, 190.
- LIU, S. H., ENGLAND, W. B., and MYRON, H. W., 1973, *A.I.P. Conf. Proc.*, **18**, 1054 (19th Ann. Mag. Conf., Boston).
- MAREZIO, M., DERNIER, P. D., MENTH, A., and HULL, G. W., 1972, *J. Solid St. Chem.*, **4**, 425.
- MATTHEISS, L. F., 1973 a, *Phys. Rev. B*, **8**, 3719; 1973 b, *Phys. Rev. Lett.*, **30**, 384.
- MATTHEISS, L. F., 1974, *Phys. Rev. B* (to be published).
- MATTIS, D. C., and LANGER, W. D., 1970, *Phys. Rev. Lett.*, **25**, 376.
- MEYER, S., 1974, Ph.D. Thesis, Stanford University.
- MOOIJ, J. H., 1973, *Phys. Stat. Sol. A*, **17**, 521.
- MONCTON, D. E., 1973, *Solid St. Commun.*, **13**, 1779.
- MONCTON, D. E., and AXE, J. D., 1974 (unpublished work).
- MORINGA, M., 1974 (to be published).
- MOSS, S. C., 1969, *Phys. Rev. Lett.*, **22**, 1108.
- MOSS, S. C., KEATING, D. T., and AXE, J. D., 1973, *Proc. Conf. on Phase Transitions*, edited by L. E. Cross (Penn. State Univ., Mater. Res. Bull./Pergamon), pp. 179-88.
- MURPHY, D. W., DI SALVO, F. J., HULL, G. W., WASZCZAK, J. V., MEYER, S. F., STEWART, G. R., EARLY, S., ACRIVOS, J. V., and GEBALLE, T. H., 1974, *J. chem. Phys.* (to be published).
- MURRAY, R. B., BROMLEY, R. A., and YOFFE, A. D., 1972, *J. Phys. C*, **5**, 746.
- MURRAY, R. B., and YOFFE, A. D., 1972, *J. Phys. C*, **5**, 3038.
- MYRON, H. W., and FREEMAN, A. J., 1973, *Physics Lett. A*, **44**, 167; 1974, *Phys. Rev.*, **B**, **9**, 481.
- OMLOO, W. P. F. A. M., and JELLINEK, F., 1970, *J. less-common Metals*, **20**, 121.
- OVERHAUSER, A. W., 1968, *Phys. Rev.*, **167**, 691; 1971, *Ibid. B*, **3**, 3173.
- PARRY, G. S., SCRUBY, C. B., and WILLIAMS, P. M., 1974, *Phil. Mag.*, **29**, 601.
- RATH, J., and CALLAWAY, J., 1973, *Phys. Rev. B*, **8**, 5398.
- RENKER, B., PINTSCHOVIVUS, L., GLÄSER, W., RIETSCHEL, H., COMES, R., LIEBERT, L., and DREXEL, W., 1974, *Phys. Rev. Lett.*, **32**, 836.
- RENKER, B., RIETSCHEL, H., PINTSCHOVIVUS, L., GLÄSER, W., BRÜESEL, P., KUSE, D., and RICE, M. J., 1973, *Phys. Rev. Lett.*, **30**, 1144.
- REVELLI, J. F., Jr., and PHILLIPS, W. A., 1974, *J. Solid St. Chem.*, **9**, 176.
- RICE, M. J., and STRÄSSLER, S., 1973, *Solid St. Commun.*, **13**, 1931.
- RICE, T. M., BARKER, A. S., HALPERIN, B. J., and MCWHAN, D. B., 1969, *J. appl. Phys.*, **40**, 1337.
- RICE, T. M., and HALPERIN, B. J., 1970, *Phys. Rev. B*, **1**, 509.
- RIETSCHEL, H., 1973, *Solid St. Commun.*, **13**, 1859.
- ROTH, L. M., ZEIGER, H. J., and KAFLAN, T. A., 1966, *Phys. Rev.*, **149**, 519.
- SATO, H., and TOTI, R. S., 1968, *Bull. Soc. fr. Minér. Cristallogr.*, **91**, 557.
- SAUVAGE, M., and PARTHÉ, E., 1972, *Acta crystallogr. A*, **28**, 607.
- SHACKLETTE, L. W., and WILLIAMS, W. S., 1973, *Phys. Rev. B*, **7**, 5041.
- SHAPIRO, S. M., AXE, J. D., SHIRANE, G., and RACCAH, P. M., 1974, *Solid St. Commun.*, **15**, 377.

- SHARP, R. I., 1969, *J. Phys. C*, **2**, 421, 432.
- SHIRANE, G., and AXE, J. D., 1971 a, *Phys. Rev.*, B, **4**, 2957; 1971 b, *Phys. Rev. Lett.*, **27**, 1803.
- SMITH, T. F., DE LONG, L. E., MOODENBAUGH, A. R., GEBALLE, T. H., SCHWALL, R. E., 1972, *J. Phys. C*, **5**, L230.
- SMITH, T. F., and FISHER, E. S., 1973, *J. low Temp. Phys.*, **12**, 631.
- TACHIKI, M., and TERAMOTO, K., 1966, *J. Phys. Chem. Solids*, **27**, 335.
- THOMAS, G. A., GIRAY, A. B., and PARKS, R. D., 1973, *Phys. Rev. Lett.*, **31**, 241.
- THOMPSON, A. H., GAMBLE, F. R., and KOEHLER, R. F., 1972, *Phys. Rev. B*, **5**, 2811.
- THOMPSON, A. H., GAMBLE, F. R., and REVELLI, J. F., 1971, *Solid St. Commun.*, **9**, 981.
- THOMPSON, A. H., PISHARODY, K. R., and KOEHLER, R. F., 1972, *Phys. Rev. Lett.*, **29**, 163.
- TRAUM, M. M., SMITH, N. V., and DI SALVO, F. J., 1974, *Phys. Rev. Lett.*, **32**, 1241.
- VAN LANDUYT, J., REMAUT, G., and AMELINCKX, S., 1970, *Phys. Stat. Sol.*, **41**, 271.
- VAN MAAREN, M. H., and HARLAND, H. B., 1969, *Phys. Lett. A*, **29**, 571, and unpublished.
- VOLKENSTEIN, N. V., DYAKINA, V. P., and STARTSEV, V. E., 1973, *Phys. Stat. Sol. B*, **57**, 9.
- WANG, C. S., and CHEN, J. M., 1974, *Solid St. Commun.*, **14**, 1145.
- WERNER, S. A., 1975 (to be published).
- WILLIAMS, P. M., PARRY, G. S., and SCRUBY, C. B., 1974, *Phil. Mag.*, **29**, 695.
- WILSON, J. A., 1972, *Adv. Phys.*, **21**, 143; 1973, *Proc. Conf. on Phase Transitions*, edited by L. E. Cross (Penn. State Univ., Mater. Res. Bull./Pergamon), pp. 101-16; 1975, *Rev. mod. Phys.* (to be published).
- WILSON, J. A., and YOFFE, A. D., 1969, *Adv. Phys.*, **18**, 193.
- WILSON, J. A., DI SALVO, F. J., and MAHAJAN, S., 1974, *Phys. Rev. Lett.*, **32**, 882 (also 1973, *Bull. Am. phys. Soc.*, **18**, 386).
- YAMAGUCHI, S., and HIRABAYASHI, M., 1972, *J. phys. Soc. Japan*, **33**, 708.
- YAMAYA, K., and SAMBONGI, T., 1972, *Solid St. Commun.*, **11**, 903.
- YOFFE, A. D., 1973, *Festkörperprobleme*, **XIII**, 1.